

Multi-plane super-resolution microscopy

THÈSE N° 7570 (2017)

PRÉSENTÉE LE 24 FÉVRIER 2017

À LA FACULTÉ DES SCIENCES ET TECHNIQUES DE L'INGÉNIEUR
LABORATOIRE D'OPTIQUE BIOMÉDICALE
PROGRAMME DOCTORAL EN PHOTONIQUE

ÉCOLE POLYTECHNIQUE FÉDÉRALE DE LAUSANNE

POUR L'OBTENTION DU GRADE DE DOCTEUR ÈS SCIENCES

PAR

Azat SHARIPOV

acceptée sur proposition du jury:

Prof. Y. Bellouard, président du jury
Prof. T. Lasser, Dr M. Leutenegger, directeurs de thèse
Dr L. Bonacina, rapporteur
Prof. D.-P. Herten, rapporteur
Prof. G. Fantner, rapporteur



ÉCOLE POLYTECHNIQUE
FÉDÉRALE DE LAUSANNE

Suisse
2017

Abstract

Understanding cell functions is the major goal of molecular biology, which intends to elucidate the interactions between biomolecules at a subcellular level. One of the widely used techniques in molecular biology is fluorescence microscopy, which offers high specificity and sensitivity at the submicrometer spatial scale but is limited by diffraction to about 200nm lateral resolution, which is insufficient for the observation of many molecular processes.

During the last two decades several super-resolution techniques overcoming the diffraction limit have been developed. However, imaging samples in three dimensions (3D) at high speed remains a challenging and not yet resolved task. This thesis focuses on enhancing super-resolution imaging towards fast, live-cell and 3D imaging.

Super-resolution optical fluctuation imaging (SOFI) is a technique based on the stochastic fluctuations of photoswitchable fluorescent markers. It possesses several unique features such as background reduction, capability of increased pixel grid generation, i.e. spatial oversampling, as well as tolerance and robustness to a wide range of photoswitching conditions. In this thesis SOFI was extended to perform 3D analysis. As a result, the resolution in all three spatial dimensions can be improved and the depth sampling increased.

We present a novel design of a 3D fluorescence microscope capable of acquiring images of eight depth planes simultaneously. This design incorporates an image-splitting prism, a single optical element allowing to achieve in-depth image separation. The optical performance of the 3D microscope was described and experimentally verified. The simultaneous depth plane acquisition allows to fully exploit the 3D capabilities of SOFI while generating additional virtual depth planes.

An algorithm for the extraction of switching kinetics of fluorescent markers is presented. Using appropriate imaging conditions, we demonstrate the applications of 3D SOFI on several examples of fixed and living cells. We also present the potential of the 3D microscope for phase retrieval in transparent samples.

Key words: Optical Microscopy, Biomedical Imaging, Super-Resolution Imaging, Fluorescence, Single Molecule, Stochastic Optical Fluctuation Imaging, SOFI, Live cell imaging, 3D imaging

Résumé

La compréhension des fonctions cellulaires est le principal objectif de la biologie moléculaire. Elle vise à élucider les interactions entre les biomolécules à un niveau subcellulaire. L'une des techniques largement utilisée en biologie moléculaire est la microscopie à fluorescence. Elle offre une spécificité et une sensibilité élevées à l'échelle submicrométrique. Cependant, la microscopie submicrométrique est limitée par la diffraction à environ 300 nm de résolution latérale qui est insuffisante pour les observations de nombreux processus moléculaires.

Au cours des deux dernières décennies, plusieurs techniques de super-résolution s'affranchissant de cette limitation ont été développées. Cependant, l'imagerie des échantillons en trois dimensions (3D) à grande vitesse restent une tâche difficile et encore non résolue. Cette thèse se concentre sur le développement de l'imagerie à super résolution et en particulier sur l'imagerie rapide de cellules vivantes en 3D.

L'imagerie par fluctuations optiques à super résolution (SOFI) est une technique basée sur les fluctuations stochastiques des marqueurs fluorescents photocommutables. Cette technique possède plusieurs caractéristiques uniques telles que la réduction de l'arrière-plan, la capacité de densification de la grille de pixels, c'est-à-dire le suréchantillonnage, ainsi que la tolérance et la robustesse à une large gamme de marqueurs aux propriétés diverses. Dans cette thèse, SOFI a été enrichie pour effectuer une analyse en 3D. De cette façon, la résolution dans les trois dimensions spatiales est améliorée et l'échantillonnage en profondeur est augmenté.

Nous présentons une nouvelle conception d'un microscope à fluorescence 3D capable d'acquérir simultanément des images de huit plans en profondeur. Cette conception intègre un prisme de fractionnement de l'image, un seul élément optique permettant d'obtenir une séparation en profondeur. Les performances optiques du microscope 3D ont été décrites et vérifiées expérimentalement. L'acquisition simultanée des plans en profondeur permet d'exploiter pleinement les capacités de SOFI tout en générant des plans supplémentaires virtuels en profondeur.

Un algorithme pour l'extraction de la cinétique de commutation des marqueurs fluorescents est présenté. En utilisant les conditions d'imagerie appropriées, nous démontrons les applications de SOFI en 3D sur plusieurs exemples de cellules fixes et vivantes. Nous présentons également le potentiel du microscope 3D pour le calcul de la phase dans des échantillons transparents.

Mots clés : Microscopie optique, Imagerie biomédicale, Imagerie à super résolution, Fluorescence, SOFI, Imagerie cellulaire, Imagerie 3D

Contents

Abstract (English/Français)	i
1 Introduction	1
2 General concepts and methods	5
2.1 Diffraction limited wide field fluorescence microscopy	5
2.2 Fluorescence and photoswitching	9
2.2.1 Fluorescence fundamentals	9
2.2.2 Photoswitching	11
2.2.3 Fluorescent proteins	12
2.3 Single molecule localization super-resolution microscopy	12
2.4 Super-resolution Optical Fluctuation Imaging	14
2.4.1 Introduction	14
2.4.2 Cumulants	15
2.4.3 Cumulant imaging	17
2.4.4 Linearized SOFI	20
2.4.5 Cross-cumulants	22
2.4.6 3D cross-cumulants	24
3 Multi-plane setup and its configurations	27
3.1 Epi-fluorescence microscope and its extensions	27
3.2 ABCD matrix description of the optical setup	30
3.3 Ray tracing	33
3.4 Experimental characterization:	39
3.4.1 Lateral image displacement in beamsplitter	39
3.4.2 Interplane distances	41
3.4.3 PSF characterization	42
3.4.4 Brightness response	43
4 SOFI imaging	45
4.1 Sample preparation	45
4.1.1 Immunofluorescence	45
4.1.2 Transfection and expression of fluorescent proteins	46
4.1.3 Direct labeling with cell-permeant probes	47

Contents

4.1.4	Sample preparation protocols	47
4.2	Optimizing imaging conditions	49
4.3	Fixed cell 3D fluorescence imaging	53
4.4	Live cell and bacteria 2D fluorescence imaging	54
4.5	Journal article preview/manuscript	58
4.5.1	Introduction	58
4.5.2	Experimental setup	59
4.5.3	Image reconstruction	60
4.5.4	Live cell imaging	62
4.5.5	Discussion	64
4.5.6	Methods	64
5	Conclusions and outlook	67
	Image gallery	71
A	Image splitting prism characterization and setup alignment	75
A.1	ABCD calculation conventions	75
A.2	Jones Matrix description of the beam splitter	75
A.2.1	Jones Matrix total internal reflection	76
A.2.2	Summary	77
A.3	3D epi-fluorescence microscope alignment	77
	Acknowledgments	83
	Bibliography	85
	Curriculum vitae	92

1 Introduction

The cell is a basic building unit of living organisms. Anton van Leeuwenhoek built one of the first microscopes and observed a single cell back in the 17th century. This event can be considered as a starting point of cell biology and microscopy. Since then, optical microscopy is one of the essential techniques to observe the intracellular structures and processes in biology and evolved as an ever growing field in optics.

Known cells range in size from one to hundreds of micrometers. Many of the intracellular structures and processes are driven by biomolecules as small as one to several tens of nanometers. This imposes a limit on the application of a classical optical microscope, which can resolve around 200 nm in lateral and 500 nm in axial dimensions due to a fundamental physical limitation, the diffraction limit.

During the last two decades, several new optical imaging techniques were introduced to overcome the diffraction limit [1, 2, 3]. These techniques can be divided into two main categories depending on the exploited quantum mechanical property of fluorophores. The deterministic approach exploits the non-linear response of fluorophores to excitation. This category includes the first super-resolution technique - stimulated emission depletion (STED) [4, 5, 6, 7], and saturated structured illumination microscopy (SSIM) [8]. The stochastic approach exploits the random photoswitching of fluorophores as exploited for instance by single molecule localization methods, such as photoactivated localization microscopy (PALM) [9] and stochastic optical reconstruction microscopy (STORM) [10, 11], and correlation-based methods, such as super-resolution optical fluctuation imaging (SOFI) [12, 13].

In STED, an excitation beam induces spontaneous emission of fluorophores. An additional doughnut-shaped depletion beam makes fluorophores exhibit stimulated emission inside its irradiation region, constraining the spontaneous emission of fluorophores to a small volume in the center of the depleting doughnut beam, much smaller than the classical excitation and detection point spread function (PSF), figure 1.1. Therefore, by scanning the sample with such an excitation-depletion pattern, one can significantly improve the spatial resolution. In theory, this approach offers unlimited resolution. In practice, fluorophore bleaching, aberrations of

Chapter 1. Introduction

the optical system and light scattering in biological specimen limit the resolution to $\sim 20\text{nm}$ in lateral and $\sim 50\text{nm}$ in axial dimensions. A 4π implementation of STED was also demonstrated, yielding a resolution improvement in axial dimension [14, 15].

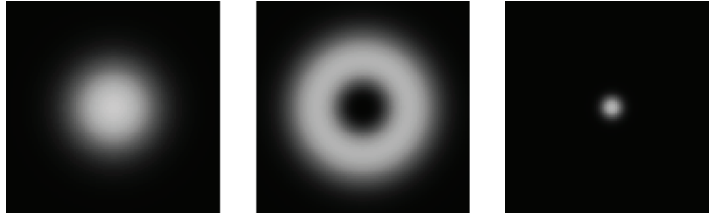


Figure 1.1: STED technique: excitation spot (left), doughnut-shaped depletion laser spot (center), remaining area from where spontaneous fluorescence can be detected (right)[16].

Structured illumination microscopy (SIM) improves image resolution by applying a periodical illumination pattern, typically a sinusoidal grid. The acquired single image is then a product of the illumination pattern and the sample structure (figure 1.2). Several images obtained with shifted and/or rotated illumination patterns are then acquired in order to calculate the final super-resolved image. The resolution improvement can be observed when looking at the Fourier transform of the acquired images, where an offset introduced by grid pattern allows to observe higher spatial frequencies [17].

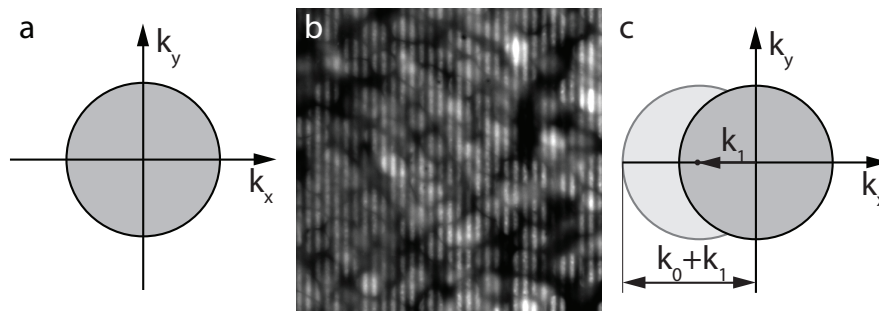


Figure 1.2: SIM technique: (a) Spatial frequencies k_0 observed by a normal microscope. (b) sample illuminated with a sinusoidal pattern of spatial frequency k_1 . (c) Offset frequency image allows to observe higher spatial frequencies [18].

Since the illumination and the detection are both limited by diffraction, the resolution can be doubled utmost in the linear regime. Saturated excitation of the fluorophores allows to further improve the resolution by exploiting the nonlinear response to excitation [18]. This way, a resolution of at best 50 nm was achieved [19, 20].

Single plane illumination microscopy (SPIM) [21, 22] provides another possibility for 3D imaging. In this technique, an additional objective lens is used to create a thin sheet of light

placed orthogonally to the imaging objective (figure 1.3). This allows to image a single plane at a time and avoid bleaching of the out of focus structures. By scanning the sample along the axial dimension, the 3D image can be recorded.

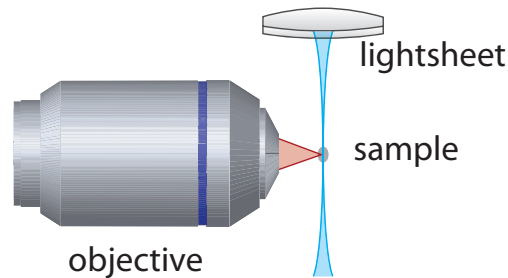


Figure 1.3: SPIM technique: light sheet is used to illuminate a single plane at a time.

The use of Bessel beam for the excitation instead of the conventional Gaussian beam allowed to craft ultrathin light sheets, enabling further increase in resolution and bleaching reduction [23]. SPIM was also demonstrated with a single-objective approach, where a micromirror cavity is used to create a light sheet from epi-illumination [24].

In stochastic approaches, such as PALM and STORM, any fluorescent sample can be determined by the spatial coordinates of individual fluorophores, provided that the fluorophores can be accurately localized individually. If the fluorescence emission is controlled such that only one fluorophore within a PSF emits at a time, the positions of the fluorophores can be determined with a much higher accuracy than the resolution limit for the system, and the sample structure can be reconstructed with an improved resolution. This concept is key for PALM and STORM [25, 26, 27], where temporal separation is achieved by using photoactivatable [28, 29] or photoswitchable fluorophores [30, 31]. Therefore, when a fluorescent sample is excited, only a random, tiny fraction of the molecules are bright at each moment of time whereas the majority of labels stay dark. Repeated imaging of stochastically blinking fluorophores allows to localize them separately in many images and to build a super-resolved map of their positions, as shown in figure 1.4. The resolution of the reconstructed image is determined by the localization precision and the fluorophore density. Lateral resolutions of about 20 nm have been reported with this approach.

The performances of different available algorithms have been compared in a review paper by D. Sage [32]. In particular, an algorithm allowing to work with high-density labeling for fitting of overlapping PSFs was introduced [33]. The use of photoswitchable membrane probes also allowed to demonstrate STORM in live cells [34]. Recently, more extensions of STORM for 3D imaging were presented. It can be done by using an engineered PSFs, such as astigmatic [35] or double-helix [36].

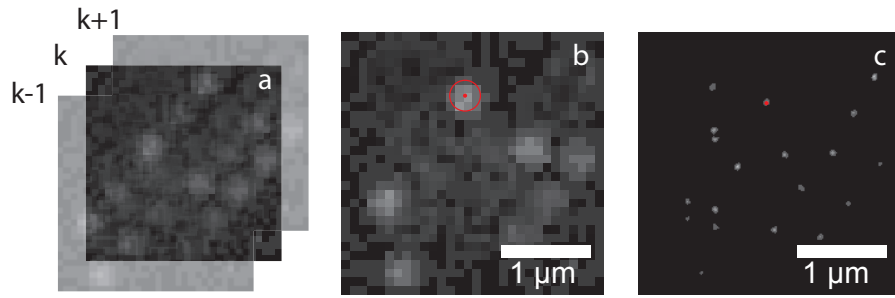


Figure 1.4: STORM technique: (a) A sequence of images of blinking emitters is acquired. (b) The center of each PSF is localized per frame. (c) The determined centers are assembled into a single composite image [37].

In 2009 Dertinger et al. introduced a new technique based on stochastic blinking called Super-resolution Optical Fluctuation Imaging (SOFI) [13]. In contrast to localization methods, SOFI analyses the statistics of spatio-temporal fluctuations to improve the image resolution by the use of higher order cumulants, quantities related to higher order correlations [38].

SOFI relies on high-order statistical analysis of temporal fluctuations, which can be caused by fluorophore blinking and recorded in a sequence of images. The resolution improves with the order of the cumulant analysis in discrete steps, which allows to obtain images at growing resolutions. Since the background is not correlated, cumulant orders of 2 and higher yield a significant background reduction and, hence, largely enhanced contrast. Recently, Geissbuehler et al. [37] showed that SOFI exhibits a robust behavior in a wider variety of samples and photo-switching kinetics in comparison to STORM/PALM.

The original SOFI algorithm is based on computing high order autocumulants. It was shown that spatio-temporal cross-cumulants between different pixels yield finer sampling grids not limited by the effective pixel size [12]. This means that neither the system magnification nor the pixel size is a limiting factor for the final image grid density, which increases linearly with increasing cumulant order. Unlike interpolated pixels, these new intermediate pixels contain true information on the object.

This thesis focuses on further improvement of the SOFI technique, aiming at fast, live-cell compatible, and three-dimensional (3D) super-resolved imaging. Chapter 2 introduces the SOFI algorithm and underlying principles of molecular photoswitching. In particular, the 3D cumulant analysis is explained. For 3D imaging a custom microscope was built. The development and characterization of this multi-plane epi-fluorescence microscope is explained in chapter 3. Chapter 4 introduces the sample labeling and the optimization of imaging conditions, followed by the SOFI imaging results and discussion. Chapter 5 summarizes the achieved results and gives an outlook for the further exploitation of the multi-plane microscope capabilities.

2 General concepts and methods

This chapter introduces the classical wide-field microscope (2.1), the fluorescence process (2.2), single molecule localization microscopy (2.3), and super-resolution optical fluctuation imaging (2.4). All these elements are essential for this thesis and are intended as a general view of super-resolution optical fluctuation imaging (SOFI), the key topic of this thesis.

2.1 Diffraction limited wide field fluorescence microscopy

The word 'microscope' can be traced back into ancient Greek, where 'micro' means small and 'skopein' means to look or to see. This wording describes perfectly classical optical microscopy which uses visible light to create a magnified image of a microscopic object hidden to be viewed by an unaided human eye.

Today's classical wide-field microscope design is shown in figure 2.1. The scheme shows the design of an Infinity-Color-Corrected System (ICS), where an image of an object is created by a combination of an objective and a tube lens. This microscope system can be divided into the illumination path, shown as a classical Koehler illumination [39], and the observation path imaging the object at the observer's retina by a combination of an objective, a tube lens, and an ocular. The left image shows the image ray path, and the right shows the pupil ray path. As shown, the advantage of this design is the illumination homogeneity: each object point receives light from all source points, and each source point contributes to illumination of each object point equally. Due to its versatility and major advantages over the compound microscope (where an image is created directly by the objective), the ICS principle is used by all major microscope providers since the late 80'.

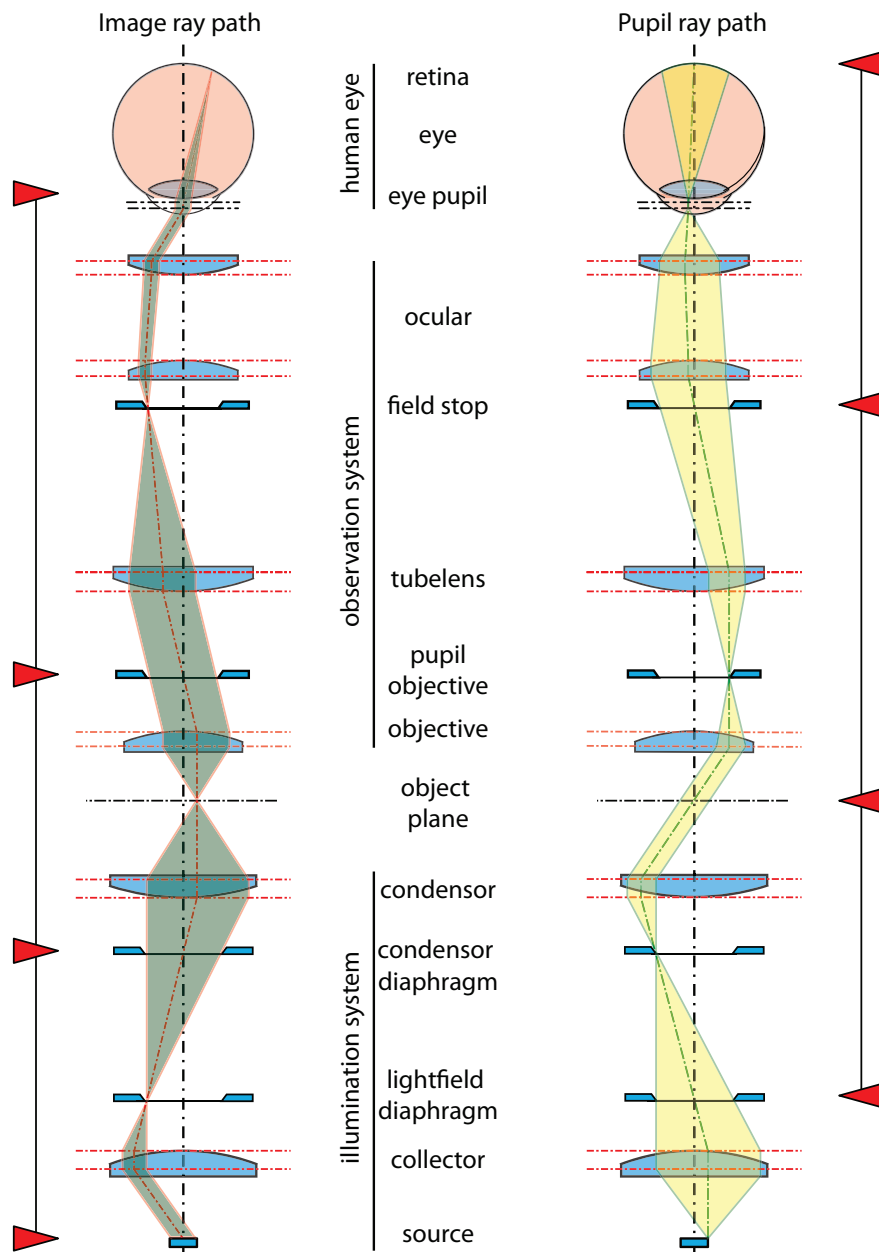


Figure 2.1: Classical wide-field ICS optical microscope beam paths for imaging and illumination. Red arrows shows the conjugated planes. Left: the image ray path shows the field stop and its images, the windows. Right: the pupil ray path shows the aperture stop and its images, the pupils.

The performance of a microscope is mainly characterized by its spatial resolution, which is a fundamental intrinsic property of the instrument, and by the image contrast, which also depends on the sample properties. The image of a thick cell formed by a classical wide-field microscope shows a low intrinsic contrast. This intrinsic contrast basically reports the integrated light scattering properties of the sample. This means that the index variations of

2.1. Diffraction limited wide field fluorescence microscopy

cellular structures are generating this intrinsic contrast. The contrast can be enhanced by dark field, polarization or phase contrast microscopy [40]. However, methods relying on the intrinsic contrast of the sample lack specificity.

Fluorescence provides an extrinsic contrast enhancement which is obtained by attaching fluorophores to the sample/cell structures of interest. Labels can be attached with a high molecular specificity using antibodies or genetic engineering (detailed description of fluorescence is given in section 2.2, and fluorescent labeling in section 4.1).

Contrast enhancement based on fluorescence labeling was a key element for discovering bacteria and has been used for many applications and discoveries in medicine [41]. Today, staining/coloring is an essential element in histology and pathology to enhance the contrast for a basic recognition of tissue structures. Similar concepts have also been used in cell biology. For example, in botanic samples the intrinsic autofluorescence has been widely used. A breakthrough in cell and molecular biology was the discovery of the GFP (Green Fluorescent Protein) [42]. This molecule was the starting point of genetic labeling of biomolecules, where the protein could be used to target and to select cell structures of interest.

In fluorescence microscopy, a sample is exposed to an illumination with a wavelength matching the fluorophore absorption spectrum. The sample then emits fluorescent light at a longer wavelength. The most commonly used type of microscope is an epi-fluorescence microscope, where the excitation and emission both pass through the objective, but in opposite directions. The difference in excitation and emission wavelength, called Stokes shift, is used to separate the excitation from emission light with the help of an excitation filter, a dichroic mirror and an emission filter. The common design of an epi-fluorescence microscope is shown in figure 2.2.

Mercury arc or xenon arc lamps are typically used as an excitation source. Their broad spectrum covers the visible (VIS) and near-UV range. An excitation filter is used to select an appropriate excitation band. Lasers and light emitting diodes (LED) are also used as they provide high power at a selected wavelength.

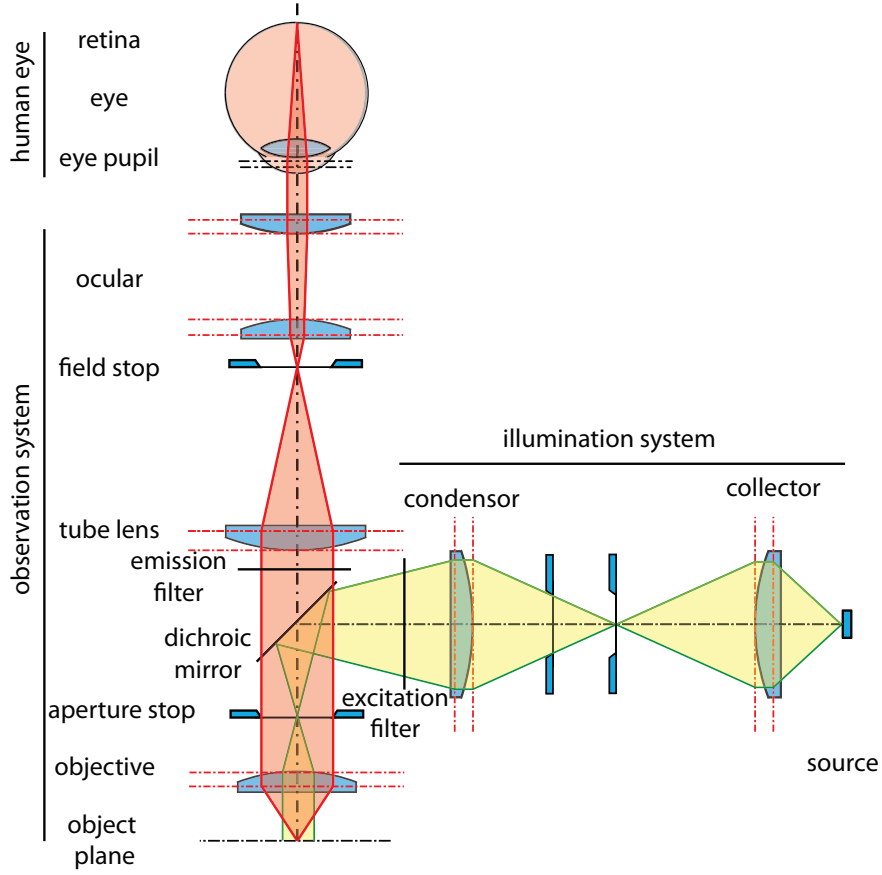


Figure 2.2: Wide-field ICS epi-fluorescence microscope.

The emission from the sample is then captured either by a human eye or a camera. Due to the wave nature of light, the spatial resolution in classical optical microscopy is fundamentally limited by diffraction. The light from a point source cannot be imaged into a point, but is spread into the so-called Point Spread Function (PSF), i.e. the intensity image covers a finite area. In fluorescence microscopy different fluorophores emit light incoherently. An intensity image of an arbitrary fluorescently labeled object can therefore be described as a convolution of the true object with the intensity PSF $U(\vec{r}')$ fully determined by the microscope properties:

$$I_i(\vec{r}') = I_o(\vec{r}) \otimes U(\vec{r}'), \quad (2.1)$$

where I_i and I_o are image and object intensities depending on the image and object spatial coordinates \vec{r}' and \vec{r} accordingly, and $\vec{r}' = M\vec{r}$, where M is the magnification. The resolution limit of a microscope is typically defined as the minimal distance between two point sources that still allows their distinction. This definition was formulated by Ernst Abbe [43] almost 150 years ago and expressed as

$$d \approx \lambda/2NA, \quad (2.2)$$

where λ is the wavelength of the light and NA represents the numerical aperture of the imaging system. This formula approximates Rayleigh's criterion, formulated as follows: two point sources of equal intensity are considered resolved if the maximum of one diffraction (Airy) pattern matches the first minimum of the other one (image 2.3). Using the fluorophores emitting in a visible part of the spectrum, one can achieve a PSF extent of approximately 200 nm full width at half-maximum (FWHM) in lateral and 500 nm in axial dimensions at best.

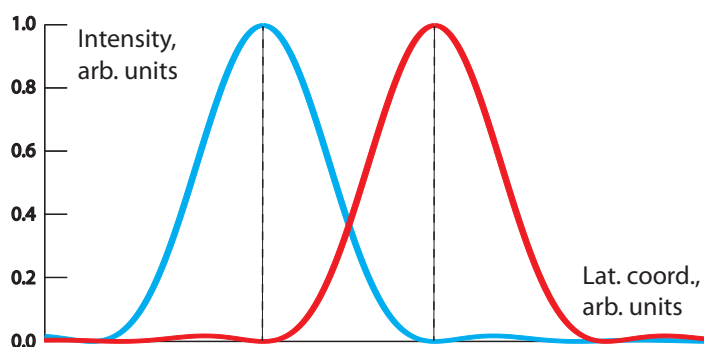


Figure 2.3: Rayleigh criterion. Red and blue curves represent the diffraction patterns of two point sources. The maximum of one diffraction pattern matches the first minimum of the other. The distance between the two maxima represents the resolution limit.

Overcoming the diffraction limit opened a new field in microscopy, called super-resolution microscopy. Although many cell structures have been studied using classical fluorescence microscopy, certain features stayed hidden due to the diffraction limit and require new concepts for becoming resolved. This thesis describes novel ways overcoming the diffraction limit by exploiting the photophysical properties of fluorophores.

2.2 Fluorescence and photoswitching

In this section we briefly describe the fundamental concepts of fluorescence and photoswitching which are crucial for all super-resolution techniques.

2.2.1 Fluorescence fundamentals

In a quantum mechanical description, a molecule is characterized by different energy bands. These energy bands correspond to electronic, vibrational and rotational states. The configuration of the energy levels and energy differences depends on the structure of the molecule. Upon absorption and emission of a photon, the molecule adopts different energy states. The molecule can then emit a photon via a process referred to as fluorescence. The energy difference between the energy levels is then directly proportional to the frequency of the corresponding photon.

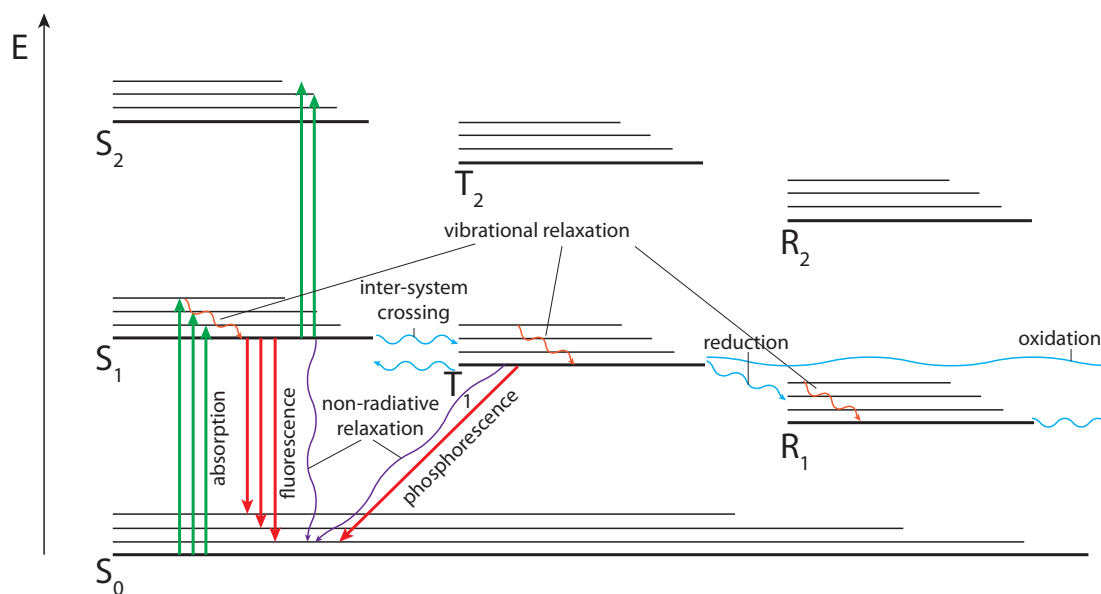


Figure 2.4: Jablonski diagram describing the electronic level structure. The electronic states are arranged vertically according to the energy and grouped horizontally according to spin multiplicity. The legends S, T, and R denote singlet, triplet, and radical states accordingly. Thick lines indicate the vibrational ground states, and narrow lines indicate the vibrational levels. Straight arrows indicate radiative, and wavy arrows non-radiative transitions between the states.

The Jablonski diagram is a convenient way to describe the electronic level structure in a molecule. The electronic states are arranged vertically according to the energy and horizontally according to spin multiplicity and molecular conformation. In this example, the ground state is referred to as S_0 , excited singlet states as S_1 , S_2 , etc, the excited triplet states as T_n , and radical states as R . Each of these states possesses vibrational and rotational sub-levels.

The absorption of a photon excites the molecule from the ground state S_0 to an excited state, e.g. S_1 . Since the absorption is light driven, there is no fundamental lower limit for the rate. After this transition, the system ends in one of the vibrational states of S_1 . Very rapidly, the molecule relaxes through a process called vibrational relaxation which occurs at a time around $10^{-12} - 10^{-10}$ s. Fluorescence emission occurs upon electron transition from the lower vibrational sub-level of the excited state to the various sub-levels of the ground state S_0 at a time of $10^{-8} - 10^{-9}$ s. Therefore, the emission spectrum represents the level structure of the ground state, whereas the absorption spectrum is dependent on the level structure of the excited state. Since certain energy is dissipated via vibrational relaxation, the emission spectrum is red-shifted compared to the excitation spectrum (Stokes shift).

The excited molecule can undergo other transitions, such as internal conversion at a rate $10^9 - 10^{11} \text{ s}^{-1}$ or a non-radiative transition from excited state S_1 to the triplet state T_1 at a rate $10^6 - 10^{10} \text{ s}^{-1}$, called inter-system crossing. Inter-system crossing is less probable as it violates the spin selection rule, but remains possible due to spin-orbit coupling. Its probability

becomes higher when the vibrational sub-levels of S_1 and T_1 partially overlap. Inter-system coupling is typical for systems containing heavy atoms (e.g. Br, I) due to strong spin-orbit coupling.

From the triplet state T_1 a molecule can relax to the ground state S_0 via radiative transition called phosphorescence. Since this transition violates spin selection rule, it occurs with a low probability and a low rate $10^2 - 10^5 \text{ s}^{-1}$. Another possibility is a reverse inter-system crossing. In general, the triplet state T_1 is long-lived - typically about 1000 times longer than the excited state S_1 . Therefore, molecules in the triplet state are more likely to interact with the environment. This, in turn, is a major reason for molecular photobleaching - irreversible photochemical alteration of a dye causing the loss of fluorescence ability.

Since molecular oxygen has a triplet ground state, it acts as a primary quencher of the fluorophore's triplet state. As oxygen enhances also the photobleaching, for long-term measurements it is advantageous to remove oxygen from the solution. In the experimental part of this thesis an enzymatic oxygen scavenging system, comprising glucose, glucose oxidase and catalase [44] was commonly used.

2.2.2 Photoswitching

In contrast to photobleaching, where the molecule is oxidated to a non-fluorescent state in an irreversible manner, reversible photoswitching or blinking is a process where molecules cycle between the fluorescent and non-fluorescent states [45]. Due to temporary residence in the triplet state, fluorophores commonly show rapid blinking. In a normal aqueous solution the typical lifetime of the triplet state is in the order of microseconds. By removing molecular oxygen from the fluorophores environment, the lifetime of its triplet state can be prolonged to milliseconds [46].

The triplet state can be quenched by reducing agents that transfer the molecule from the triplet to a meta-stable radical anion state [46]. Since these states are generally non-fluorescent and the nature of transitions is stochastic, this results in a stochastic reversible photoswitching of the molecules. The longer lifetimes of these states in aqueous solutions (seconds to minutes) favor this type of blinking for use in super-resolution microscopy, as the modern CCD or CMOS detectors can readily record at these timescales. Additionally, many of the organic fluorophores possess an additional absorption band in the near-UV range, which can be used to recover the molecule into the bright state [47]. Therefore, the switching rates of the molecules can be tuned by varying the intensities of the excitation and reactivation lasers and selecting the buffer conditions [48].

Process	rate, s ⁻¹
absorption	0 – 10 ¹²
vibrational relaxation	10 ¹⁰ – 10 ¹²
fluorescence	10 ⁸ – 10 ⁹
internal conversion	10 ⁹ – 10 ¹¹
inter-system crossing	10 ⁶ – 10 ¹⁰
phosphorescence	10 ² – 10 ⁵
reduction	10 ² – 10 ⁴

2.2.3 Fluorescent proteins

Fluorescent proteins (FPs) are small proteins which possess intrinsic fluorescent properties and can be attached to another protein of interest by genetic encoding. The compatibility of FPs with living cells or organisms in contrast to organic fluorophores favors their use in functional studies. Though the first FP to be discovered, GFP, does not possess evident blinking properties, other photoswitchable FPs have been constructed, enabling their use in super-resolution microscopy [49].

The photoswitching mechanism of simple FPs such as Dronpa can be explained by cis-trans isomerization of the chromophore, as shown by structural studies [50]. The conformational changes of the beta barrel, surrounding the chromophore, can also influence the photoswitching kinetics [51].

Dreiklang FP utilizes a different photoswitching mechanism: hydration-dehydration reaction of the chromophoric five-membered ring [52]. This enables a unique property of Dreiklang: fluorescence excitation decoupled from photoswitching. The reversible on- and off-switching can then be performed with light of 365nm and 405nm wavelength and fluorescence excitation at 515nm wavelength. Due to this ability to tune the blinking conditions, we extracted Dreiklang switching kinetics (section 4.2) and used it extensively for imaging experiments during this thesis.

2.3 Single molecule localization super-resolution microscopy

A fluorescent sample can be described by the spatial coordinates of separate fluorophores, if each of the fluorophores can be precisely localized individually. If fluorophores photoswitch at a low on-rate, such that only a single fluorophore within a PSF emits at a time, then the position of each of them can be determined with a precision higher than the resolution limit of the optical system. The stochastic and independent photoswitching can provide these conditions, which are the key requirements for the methods called STochastic Optical Reconstruction Microscopy (STORM) [10] and PhotoActivation Localization Microscopy (PALM) [9]. Originally, STORM was based on activator-reporter Cy3 and Cy5 dye pair, where Cy5 was reversibly photoswitching upon illumination by light of 2 wavelengths. PALM, on the other hand, was

2.3. Single molecule localization super-resolution microscopy

based on photoactivatable fluorescent proteins which remained in the on-state only once, and were then photobleached. Several other methods based on different switching processes were employed, such as points accumulation for imaging in nanoscale topography (PAINT) [53], where the stochastic binding and subsequent activation of freely diffusing fluorescent probes in solution is used for localization. In Direct STORM (dSTORM) and ground-state depletion followed by individual molecule return (GSDIM) [54] ordinary fluorophores are reversibly switched to a meta-stable dark state by the use of special buffer conditions.

Using different photoswitching techniques, the localization methods employ a similar microscope setup and processing algorithm. A wide-field epi-fluorescence microscope is typically used with a total internal reflection fluorescence (TIRF) modality, which allows to reduce the background illumination. The series of frames (usually several thousands) is acquired by a digital camera. For each frame the positions of emitters are localized via fitting with a sufficiently realistic PSF model (e.g. Gaussian). These positions are then assembled into a single image with a finer pixel grid to represent the final resolution.

However, this refined reconstruction does not directly translate into the spatial resolution of the image, because it is sample-dependent and is affected by several factors. The localization precision is dependent on the number of photons detected, meaning that brighter dyes can deliver better resolution. The labeling density is influencing the integrity of a reconstructed image, requiring higher labeling densities compared to a normal wide-field microscopy. However, the blinking rate of molecules should maintain the non-overlapping PSF condition [10].

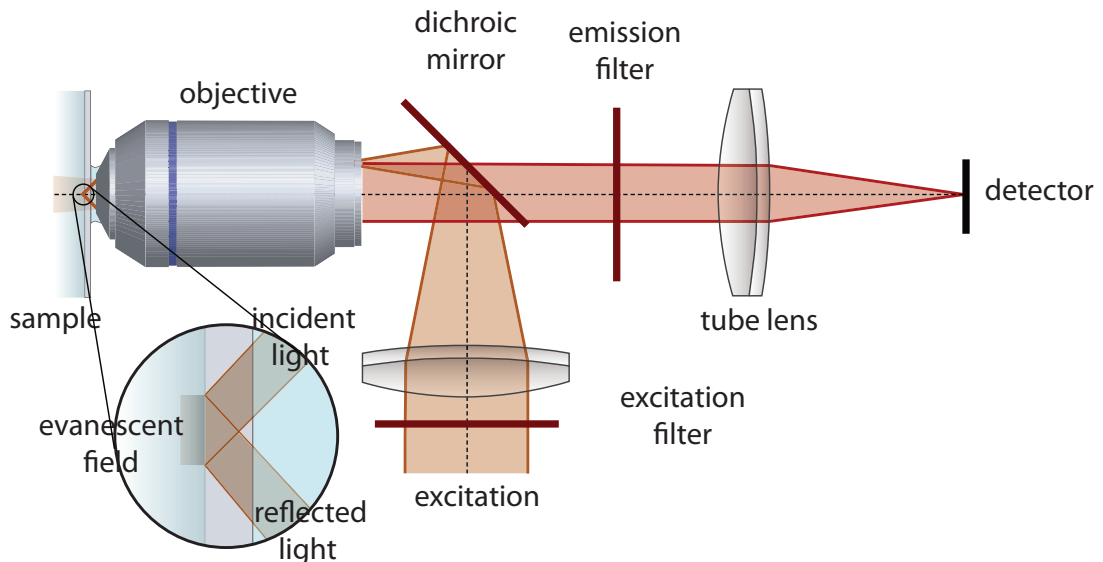


Figure 2.5: Total internal reflection fluorescence microscope. The excitation beam is focused close to the border of the objective back aperture. The light then comes out on the sample side at an angle, allowing total internal reflection. The back-reflected excitation light is then filtered by a dichroic mirror and an emission filter.

One way to improve localization precision is the use of Total Internal Reflection Fluorescence (TIRF) microscope[55]. In this microscope the excitation beam is focused on the border of the back aperture of the high NA objective lens, so that the beam undergoes total internal reflection at the coverslip-sample interface (image 2.5). The created evanescent field then only illuminates a 100-300nm thin volume close to the coverslip surface, omitting the background fluorescence from out-of-focus fluorophores, but limiting the acquisition depth. An epi-fluorescence TIRF microscope provides a further advantage in collecting the emitted fluorescence more efficiently than without TIRF.

Although being capable of delivering high sub-diffraction resolutions in ideal conditions, localization methods impose strict requirements for sample preparation and fluorophore blinking. The ratio between the dark and bright states' lifetimes should remain above 1000:1 to avoid false localizations.

2.4 Super-resolution Optical Fluctuation Imaging

2.4.1 Introduction

SOFI is a super-resolution technique based on higher-order statistical analysis of temporal fluctuations [13]. In contrast to single molecule localization methods, SOFI does not require non-overlapping PSFs, a property especially useful in live cell imaging [37]. SOFI exploits image sequences of stochastically fluctuating emitters, provided that three following conditions are fulfilled:

- The fluorescent markers should have at least two visibly distinct states, for example, a fluorescent and a non-fluorescent.
- The fluorophores should switch stochastically and independently from each other.
- The system PSF should cover several camera pixels.

If molecules switch stochastically and independently, the signal from a single molecule correlates most with itself. The n -th order autocorrelation of this signal raises the PSF to the n -th power, thereby narrowing the lateral extent of the image PSF by \sqrt{n} . SOFI benefits of this fact using cumulants, quantities related to the correlation functions, explained in section 2.4.2. Because the signals from the different molecules are independent and therefore not correlated, the n -th power of each PSF can be taken separately, avoiding cross-products and delivering a \sqrt{n} resolution improvement.

The original SOFI algorithm relied on the calculation of auto-cumulants for each pixel, limiting therefore the final resolution to the raw images' pixel size [13]. This limitation can be overcome with cross-cumulants by taking combinations of several pixels into account [12], which delivers an n -fold increased pixel density, where n is the cross-cumulant order. Moreover, a subsequent

linearization step [56] can deliver a nearly n -fold resolution improvement for the n -th order cross-cumulant. In this thesis, we implemented and extended these improvements to the three spatial dimensions [57] and time.

2.4.2 Cumulants

Cumulants, or semi-invariants, are quantities similar to moments, which, however, cannot be determined directly through the probability density function. They are usually determined through the logarithm of the characteristic function ϕ_X , or through the moments μ . In order to determine the moments, we first define the characteristic function $\phi_X(u)$ of the random variable X with a probability density function $f(x)$, where E is an expectation of X :

$$\phi_X(u) = E\{e^{iuX}\} = \int_{-\infty}^{+\infty} e^{iux} f(x) dx \quad (2.3)$$

The characteristic function can be represented as MacLaurin series:

$$\phi_X(u) = \sum_{n=0}^{+\infty} E\{X^n\} \frac{(iu)^n}{n!} = \sum_{n=0}^{+\infty} \mu_n \frac{(iu)^n}{n!} \quad (2.4)$$

Moments are defined as

$$\mu_n(X) = E\{X^n\} = \int_{-\infty}^{+\infty} x^n f(x) dx, \quad (2.5)$$

and can be derived as the coefficients in the equation 2.4:

$$\mu_n(X) = (-i)^n \left. \frac{\partial^n \phi_X(u)}{\partial u^n} \right|_{u=0} \quad (2.6)$$

Cumulants κ are determined as the coefficients of the MacLaurin series of the logarithm of the characteristic function, also known as cumulant generating function $\varphi(u)$, which shows the tight link between the cumulants and moments:

$$\varphi(u) = \ln(\phi_X(u)) = iu\kappa_1 + \frac{(iu)^2}{2!}\kappa_2 + \dots + \frac{(iu)^n}{n!}\kappa_n = \sum_{n=1}^{+\infty} \frac{(iu)^n}{n!}\kappa_n \quad (2.7)$$

The first term of this series is set equal to zero, unlike for moments. The cumulant of n -th order is then determined similarly to equation 2.5:

$$\kappa_n = (-i)^n \left. \frac{\partial^n \varphi}{\partial u^n} \right|_{u=0} \quad (2.8)$$

Several important properties of cumulants can be derived using the cumulant generating function:

Chapter 2. General concepts and methods

- Additivity for the independent random variables X and Y :

$$\varphi(u) = \ln(\mathbb{E}\{e^{iu(X+Y)}\}) = \ln(\mathbb{E}\{e^{iuX}\}) + \ln(\mathbb{E}\{e^{iuY}\}), \quad (2.9)$$

which is a consequence of multiplicativity of the characteristic function for independent random variables.

- Semi-invariance: if a and b are constants and X a set of random variables, then:

$$\varphi(u) = \ln(\mathbb{E}\{e^{iu(a+bX)}\}) = iua + \ln(\mathbb{E}\{e^{iubX}\}) = iua + \sum_{n=0}^{+\infty} b^n \kappa_n(X) \frac{(iu)^n}{n!} \quad (2.10)$$

Cumulants are then expressed as: $\kappa_1(a+bX) = a + b\kappa_1(X)$ for the first order, and $\kappa_n(a+bX) = b^n \kappa_n(X)$ for the orders $n \geq 2$.

- The cumulant generating function of a subset of independent random variables $\{X_1, \dots, X_n\}$ is written as:

$$\varphi(u) = \ln(\mathbb{E}\{e^{iu_1 X_1 + \dots + iu_n X_n}\}) = \ln(\mathbb{E}\{e^{iu_1 X_1}\}) + \dots + \ln(\mathbb{E}\{e^{iu_n X_n}\}) \quad (2.11)$$

The partial derivatives by X_n yield zero, therefore $\kappa(X_1, \dots, X_n) = 0$ for any $n > 1$.

Alternatively, cumulants can be defined through moments. By representing the characteristic function as Maclaurin series, equation 2.7 transforms into:

$$\ln \left\{ 1 + \sum_{n=1}^{+\infty} \frac{(iu)^n}{n!} \mu_n \right\} = \sum_{n=1}^{+\infty} \frac{(iu)^n}{n!} \kappa_n \quad (2.12)$$

After representing the logarithm as Maclaurin series, we obtain:

$$\sum_{m=1}^{+\infty} (-1)^{m+1} \frac{(\sum_{n=1}^{+\infty} \frac{(iu)^n}{n!} \mu_n)^m}{m} = \sum_{n=1}^{+\infty} \frac{(iu)^n}{n!} \kappa_n \quad (2.13)$$

Equating the coefficients of equal powers iu , we obtain an expression of the cumulants through the moments:

$$\begin{cases} \kappa_1 = \mu_1 \\ \kappa_2 = \mu_2 - \mu_1^2 \\ \kappa_3 = \mu_3 - 3\mu_2\mu_1 + 2\mu_1^3 \\ \kappa_4 = \mu_4 - 4\mu_3\mu_1 - 3\mu_2^2 + 12\mu_2\mu_1^2 - 6\mu_1^4 \\ \dots \end{cases} \quad (2.14)$$

Usually the expression through the central moments μ' (moments centered at the mean value)

is used. It is achieved by dropping all terms where μ_1 appears as a factor:

$$\begin{cases} \kappa_2 = \mu'_2 \\ \kappa_3 = \mu'_3 \\ \kappa_4 = \mu'_4 - 3\mu'^2_2 \\ \kappa_5 = \mu'_5 - 10\mu'_2\mu'_3 \\ \dots \end{cases} \quad (2.15)$$

For example, the first and second order cumulants correspond to the mean value and variance accordingly to moments. However, the equivalence of cumulants and central moments is only valid up to 3rd order. For the 4th and higher orders, cumulants are therefore advantageous compared to moments.

2.4.3 Cumulant imaging

We consider a sample consisting of N independently fluctuating fluorophores whose positions \vec{r}_k do not change during the acquisition time (figure 2.6, a). Assuming brightnesses A_k and temporal fluctuations $s_k(t)$ of the blinking fluorophores, the sample emission can be represented as:

$$S(\vec{r}, t) = \sum_{k=1}^N A_k \delta(\vec{r} - \vec{r}_k) s_k(t) \quad (2.16)$$

Given the isotropic imaging system PSF $U(\vec{r})$, a detected image is a convolution of the object and PSF with an addition of a temporally constant background $b(\vec{r})$ (figure 2.6, b).

$$F(\vec{r}, t) = \sum_{k=1}^N A_k U(\vec{r} - \vec{r}_k) s_k(t) + b(\vec{r}) \quad (2.17)$$

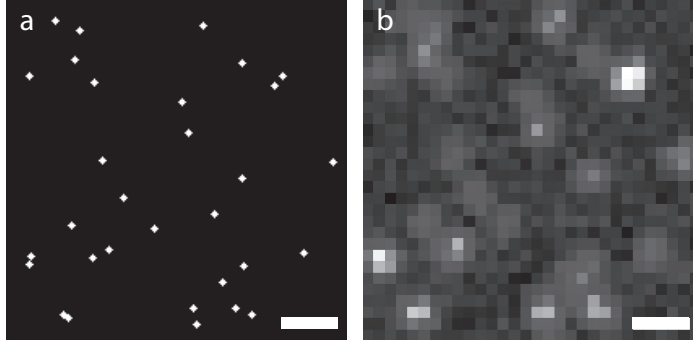


Figure 2.6: (a) Fluorophore distribution. (b) Detected wide field image. Scale bars: 500nm.

We assume that the molecules blink independently and stationary (no bleaching), therefore fluctuations can be described as zero-mean image sequence (figure 2.7):

$$\delta F(\vec{r}, t) = F(\vec{r}, t) - \langle F(\vec{r}, t) \rangle_t \quad (2.18)$$

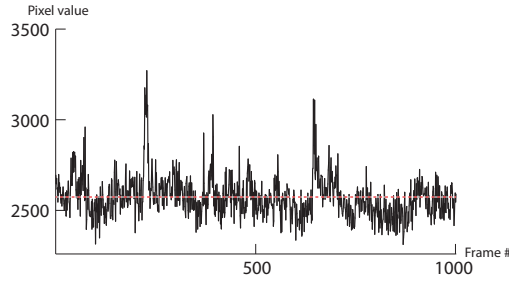


Figure 2.7: Time trace detected by a single camera pixel.

The autocorrelation of the fluctuations, or the second order SOFI image is then described as:

$$\begin{aligned} G_2(\vec{r}, t) &= \langle \delta F(\vec{r}, t) \delta F(\vec{r}, t + \tau) \rangle_t \\ &= \sum_{j,k=1}^N A_j A_k U(\vec{r} - \vec{r}_j) U(\vec{r} - \vec{r}_k) \langle \delta s_j(t + \tau) \delta s_k(t) \rangle_t \\ &= \sum_{k=1}^N A_k^2 U^2(\vec{r} - \vec{r}_k) \langle \delta s_j(t + \tau) \delta s_k(t) \rangle_t \end{aligned} \quad (2.19)$$

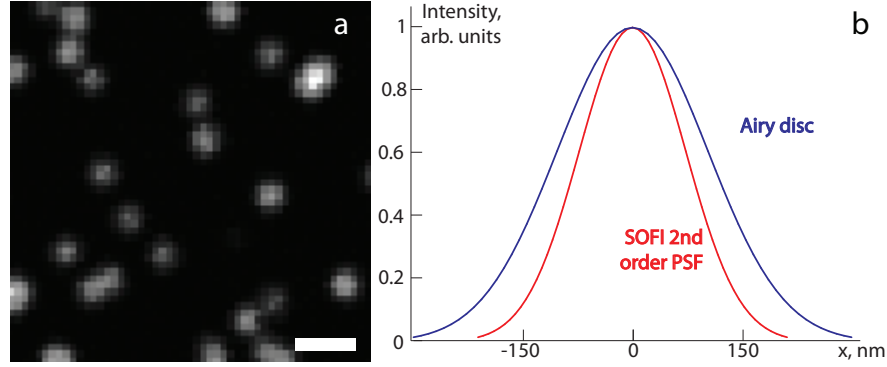


Figure 2.8: (a): Second order SOFI image, scale bar: 500nm (b): Shrinking of PSF by squaring.

Here all cross-terms with $k \neq j$ vanish due to the independency of emitter fluctuations, as well as the temporally constant background $b(\vec{r})$, according to the previously derived cumulant properties. The resulting image is then composed of the sum of squared PSFs $U^2(\vec{r} - \vec{r}_k)$ weighted by squared brightness and the correlation factor $\langle \delta s_k(t + \tau) \delta s_k(t) \rangle_t$. Assume a 3D Gaussian PSF of the system:

$$U(\vec{r}) = \exp\left(-\frac{x^2 + y^2}{2\omega_0^2} - \frac{z^2}{2\omega_{z0}^2}\right) \quad (2.20)$$

A PSF of the second order SOFI image is then narrowed by a factor of $\sqrt{2}$ in all 3 spatial dimensions:

$$\tilde{U}(\vec{r}) = U^n(\vec{r}) = \exp\left(-\frac{x^2 + y^2}{2\tilde{\omega}_0^2} - \frac{z^2}{2\tilde{\omega}_{z0}^2}\right) \quad (2.21)$$

where $\tilde{\omega}_{z0} = \omega_{z0}/\sqrt{2}$ and $\tilde{\omega}_0 = \omega_0/\sqrt{2}$. This demonstrates the principle of achieving super-resolution by SOFI, as shown in figure 2.8.

For obtaining higher resolution, a higher order correlation function could be calculated. However, as mentioned before, it is additive only up to third order, since higher orders contain cross-terms, limiting the resolution improvement. For higher orders, we rely on cumulants due to their additivity:

$$\begin{aligned} C_n(\vec{r}, \tau_1, \dots, \tau_{n-1}) &= \kappa(\delta F(\vec{r}, t), \delta F(\vec{r}, t + \tau_1), \dots, \delta F(\vec{r}, t + \tau_{n-1})) \\ &= \sum_{k=1}^N A_k^n U^n(\vec{r} - \vec{r}_k) \kappa(\delta s_k(t), \delta s_k(t + \tau), \dots, \delta s_k(t + \tau_{n-1})) \\ &= \sum_{k=1}^N A_k^n U^n(\vec{r} - \vec{r}_k) c_{n,k}(\tau_1, \dots, \tau_{n-1}) \end{aligned} \quad (2.22)$$

The n -th order cumulant image is then represented by the sum of n -th power PSFs $U^n(\vec{r} - \vec{r}_k)$ weighted by n -th power brightness and the correlation factor $c_{n,k}(\tau_1, \dots, \tau_{n-1})$. n -th power of PSF therefore provides \sqrt{n} resolution improvement [13, 38, 58]. Assuming that the brightness

and blinking statistics don't vary in a small regions of a adjacent pixels, we can also approximate this expression as:

$$C_n(\vec{r}, \tau_1, \dots, \tau_{n-1}) = A(\vec{r})^n c_n(\tau_1, \dots, \tau_{n-1}) \sum_{k=1}^N U^n(\vec{r} - \vec{r}_k) \quad (2.23)$$

Since shot noise, which is typically a major source of noise in fluorescence images, is uncorrelated in time, for higher order cumulant calculation ($n > 1$), it is advantageous to use non-zero time lags. The use of zero time lag would be equivalent to multiplying the fluctuating signals with themselves, and would introduce a shot noise bias in the cumulant values. Any other time lag cancels this bias. However, time lags should be no longer than the molecules' on-time to ensure proper signal correlation.

2.4.4 Linearized SOFI

Theoretically, the SOFI resolution improvement is unlimited as higher order cumulants can be calculated. However, in practice these images suffer from a non-linear brightness response, as the brightness and temporal fluctuations are raised to the power n . Therefore, higher order cumulant images often appear as a set of few bright dots, while the majority of the structure of interest disappears in the background. Another limitation is due to the decrease of the signal-to-noise ratio (SNR) with higher order calculation. Therefore, it is advantageous to achieve maximum resolution improvement while calculating low order cumulants.

By definition, an OTF $\tilde{U}(\vec{k})$ is a Fourier transform of the system PSF $U(\vec{r})$. The OTF represents the transfer function of the object's spatial frequencies \vec{k} . As derived in equation 2.22, n -th order SOFI PSF is defined by a system PSF $U(\vec{r})$ raised to the n -th power. The corresponding OTF $O(\vec{k})$ in the Fourier space is then defined as:

$$O(\vec{k}) = \mathcal{F}(U(\vec{r})^n) = \tilde{U}(\vec{k}) \overbrace{*\dots*}^{\text{n-1 times}} \tilde{U}(\vec{k}) \quad (2.24)$$

According to Titchmarsh convolution theorem [59], the support of the OTF $O(\vec{k})$ is n times larger than the one of the optical system $\tilde{U}(\vec{k})$. It could therefore be possible to achieve n -times resolution improvement for the n -th order SOFI, in contrast to \sqrt{n} provided by the PSF. Dertinger et al. [12] demonstrated this approach by using a Fourier reweighting scheme, which is equivalent to a Wiener filter deconvolution and a smoothing with $U(\vec{r})^n$. Here we used an improved approach proposed by Geissbuehler et al. [56], where these two steps are done separately and dedicated deconvolution algorithms can be applied.

During the data processing we generally used a Lucy-Richardson deconvolution, an iterative algorithm without regularization assuming Poisson distributed noise that is well-suited for images dominated by shot noise. Assuming a source composed of point emitters located at

2.4. Super-resolution Optical Fluctuation Imaging

positions \vec{r} , the detected image is represented as:

$$d(\vec{r}') = \sum_{\vec{r}} U(\vec{r}, \vec{r}') b(\vec{r}) \quad (2.25)$$

Where $d(\vec{r}')$ is the detected brightness at an observed location \vec{r}' , $U(\vec{r}, \vec{r}')$ is the system PSF, and $b(\vec{r})$ is a brightness in location \vec{r} in the latent image. An equation for $b(\vec{r})$ can then be written and solved iteratively:

$$b(\vec{r})^{t+1} = b(\vec{r})^t \sum_{\vec{r}'} \frac{d(\vec{r}')}{c(\vec{r}')} U(\vec{r}, \vec{r}'), \quad (2.26)$$

where $c(\vec{r}') = \sum_{\vec{r}} U(\vec{r}, \vec{r}') b(\vec{r})^t$. It was shown that if the latent image converges, it converges to the maximum likelihood of $b(\vec{r})$ [60, 61]. Assuming a perfect deconvolution and applying it to the n -th order cumulant image 2.23, we obtain:

$$\tilde{C}_n(\vec{r}, \tau_1, \dots, \tau_{n-1}) = A(\vec{r})^n c_n(\tau_1, \dots, \tau_{n-1}) \sum_{k=1}^N \delta(\vec{r} - \vec{r}_k) \quad (2.27)$$

The n -th root can then be taken from the deconvolved image, linearizing the brightness response without lowering the resolution. The result is then convolved with a physically meaningful n -times narrower PSF, as provided by the cumulant OTF's n -times increased support of the optical system OTF. Figure 2.9 shows the difference between the raw and linearized SOFI images.

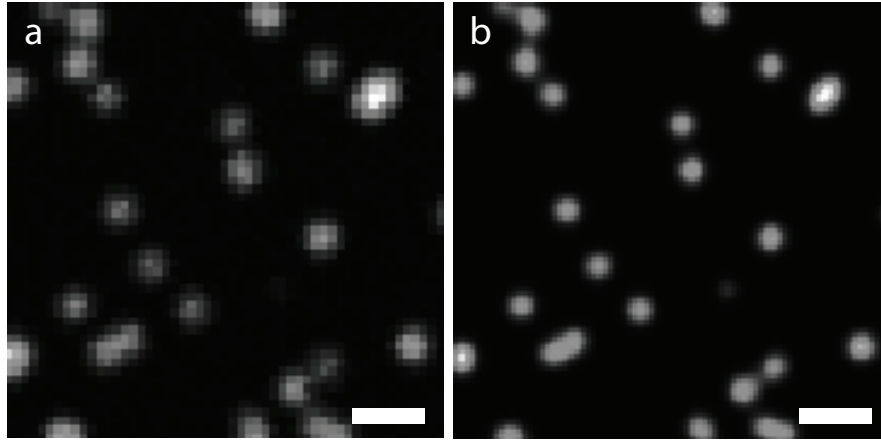


Figure 2.9: (a): Second order raw SOFI image. (b): Linearized SOFI image. Scale bars: 500nm.

Despite performing well under certain conditions, the Lucy-Richardson deconvolution has drawbacks. In particular, it assumes positive shot-noise-limited data in the original image.

However, this is not valid for higher order cumulants in the areas of fast spatial changing molecular parameters. In order to process cumulant images, we implemented the Bregman iterative method for deconvolution, which does not impose a non-negativity constraint and converges quickly as described in the manuscript in section 4.5.

2.4.5 Cross-cumulants

Up to now, we have only considered auto-cumulants of individual pixel signals with different time lags. Another possibility is the calculation of cumulants between different pixel combinations (cross-cumulants).

Similarly to equation 2.22 a formula for the n -th order cross-cumulant is given as:

$$C_n(\vec{r}_1, \dots, \vec{r}_n, \tau_1, \dots, \tau_{n-1}) = \sum_{k=1}^N A_k^2 U(\vec{r}_k - \vec{r}_1) \dots U(\vec{r}_k - \vec{r}_n) c_{n,k}(\tau_1, \dots, \tau_{n-1}) \quad (2.28)$$

Assuming a Gaussian PSF of the optical system (equation 2.20), we transform:

$$(\vec{r}_1 - \vec{r}_1)^n + \dots + (\vec{r}_n - \vec{r}_1)^n = n \left(\vec{r} - \frac{\sum_i^n \vec{r}_i}{n} \right) + \prod_{j<l}^n \frac{\vec{r}_j - \vec{r}_l}{\sqrt{n}} \quad (2.29)$$

The cross-cumulant can then be re-written as:

$$C_n(\vec{r}_1, \dots, \vec{r}_n, \tau_1, \dots, \tau_{n-1}) = \prod_{j<l}^n U\left(\frac{\vec{r}_j - \vec{r}_l}{\sqrt{n}}\right) \sum_{k=1}^N A_k^n U^n\left(\vec{r}_k - \frac{\sum_i^n \vec{r}_i}{n}\right) c_{n,k}(\tau_1, \dots, \tau_{n-1}) \quad (2.30)$$

An expression $\prod_{j<l}^n U\left(\frac{\vec{r}_j - \vec{r}_l}{\sqrt{n}}\right)$ depends on the system PSF and distances between involved pixels, and acts as a weighting factor for the n -th order cross-cumulant due to the decay of cross-correlation [12]. The calculated cumulant value is located in the geometric center $\frac{1}{n} \sum_{i=1}^N \vec{r}_i$ of the pixels involved and can be perceived as an additional 'virtual' pixel. By taking the different combinations of pixels, the final sampling grid can be n -fold improved, as shown in the figure 2.10 for the second order SOFI. This is beneficial as the super-resolved SOFI image remains well sampled.

2.4. Super-resolution Optical Fluctuation Imaging

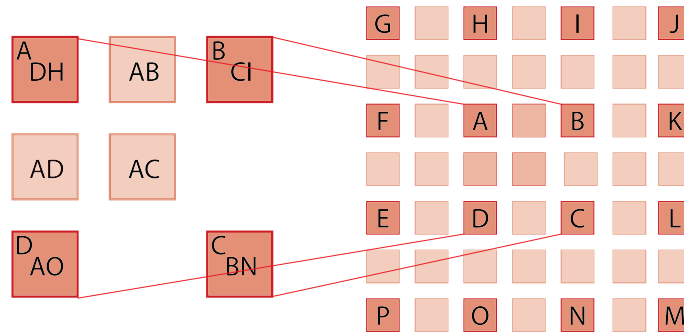


Figure 2.10: 2D second order cumulant calculation diagram. Taking the combinations of adjacent pixels, a finer sampling grid is generated.

Provided that the camera sensor does not introduce correlated noise among neighboring pixels, cross-cumulants possess the required noise bias and background reduction properties even for zero time lag. Use of cross-cumulants to generate pixel values at the physical pixels positions allows to avoid auto-cumulants completely, as shown in figure 2.10. For higher order cumulants, we considered a 4×4 pixel neighborhood and selected pixel combinations with minimal inter-distance to minimize the decay of spatial cross-correlation. Due to the zero time lag, temporal oversampling is no longer necessary. The camera exposure time and the characteristic marker's on-time can thus be matched, allowing to decrease the total acquisition time and/or to improve the SNR.

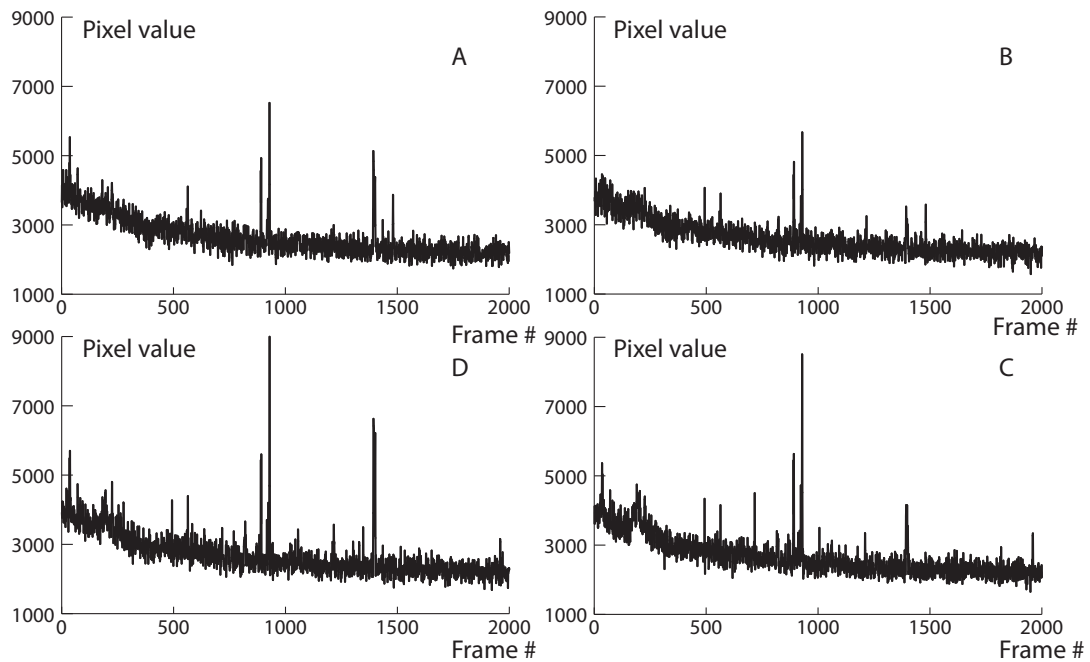


Figure 2.11: Time traces detected by 4 adjacent camera pixels A,B,C,D, according to the figure 2.10

Chapter 2. General concepts and methods

The cross-cumulant weighting factors can be calculated according to the known system PSF. Alternatively, it can be iteratively optimized by matching the PSF model (a Gaussian PSF was used in this thesis) until all the pixels have similar weights. This can be done by maximizing the smoothness of the image. The effect of this step is shown in the figure 2.12. The extracted PSF can then be used in the SOFI balancing procedure described in section 2.4.4.

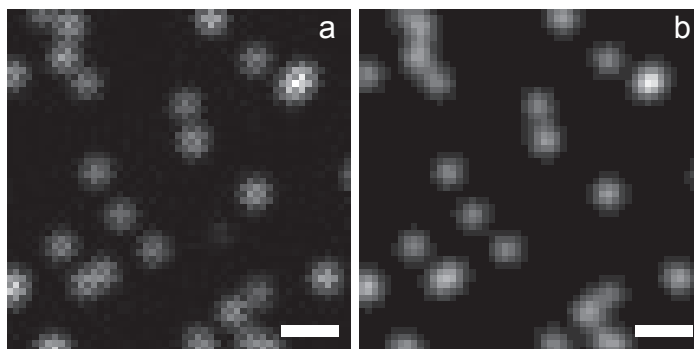


Figure 2.12: (a): Raw cross-cumulant image. (b): Flattened cross-cumulant image. Scale bars: 500nm.

2.4.6 3D cross-cumulants

As it was shown before, SOFI possesses the intrinsic property of resolution improvement along all spatial dimensions. The cumulant approach can be applied for background subtraction and optical sectioning as well, which suits well for 3D imaging. Dertinger et al. [62] demonstrated 3D imaging by mechanical scanning of the sample and acquisition of an image sequence per image plane.

However, several issues might arise in this type of imaging. The epi-illumination microscope illuminates the entire depth of the sample. Despite acquiring a single object plane at a time, the fluorescent markers are exposed and bleached throughout the sample. As well, cross-cumulants can be calculated only within each image sequence per single plane, the depth sampling cannot be improved by 'virtual' planes and the signals from other sample depths are lost.

Here we propose to use multiplexed imaging schemes (chapter 3), where several depth planes are acquired simultaneously. This allows to calculate cross-cumulants using pixel combinations from different planes, as shown in figure 2.13. Thereby, additional 'virtual' planes can be generated similarly to 'virtual' pixels to increase the depth sampling and lower the number of acquired images.

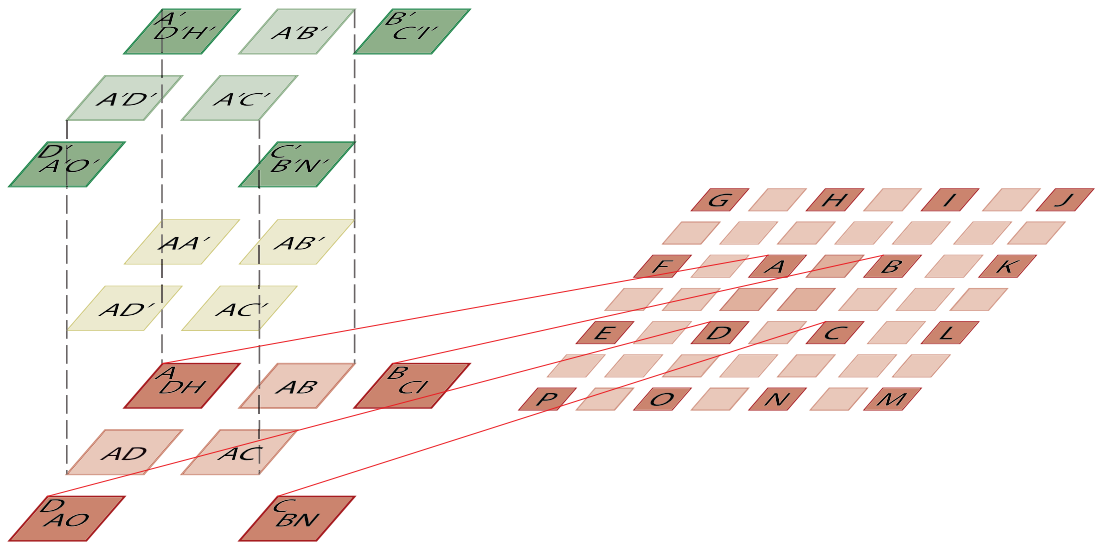


Figure 2.13: Second order 3D cumulant calculation diagram. Taking the pixel combinations from different planes allows to generate additional 'virtual' planes.

3 Multi-plane setup and its configurations

This chapter introduces the design of the multi-plane epi-fluorescence microscope, a key element of 3D SOFI, in section 3.1. Sections 3.2 and 3.2 provide an ABCD matrix description and ray tracing model for assessing the optical performance of the microscope. The results of experimental characterization and comparison to the proposed model are shown in section 3.4.

3.1 Epi-fluorescence microscope and its extensions

A typical design of an epi-fluorescence microscope is outlined in figure 3.1. This design is commonly used in life sciences and can be used to perform measurements for 2D SOFI. 3D SOFI is possible by sequential plane acquisition [62], but with limitations as discussed in section 2.4.6.

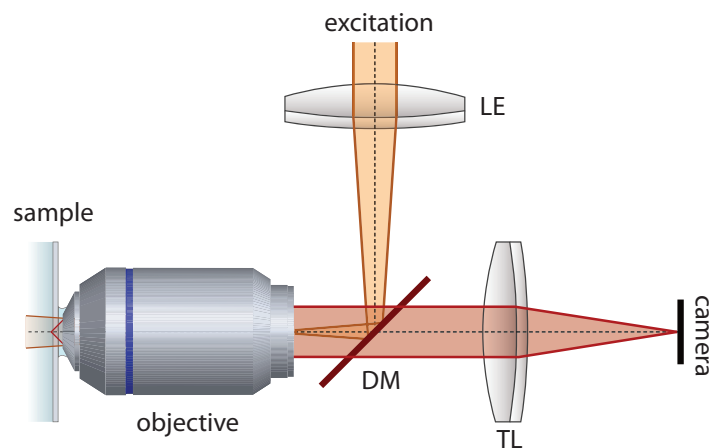


Figure 3.1: Detection part of the 2D epi-fluorescence microscope.

In order to take advantage of 3D cumulant analysis and increased depth sampling, we introduced a multi-plane epi-fluorescence microscope [57] shown in figure 3.2. The detection path

Chapter 3. Multi-plane setup and its configurations

of an epi-fluorescence microscope (figure 3.1) was complemented by an additional telescope, three diagonally arranged 50:50 beam splitters, four mirrors and two CMOS cameras. An axial shift of two mirrors by distances d and $2d$ accompanied by displacing one camera by a distance $4d$ allows to project eight equally spaced depth planes on the camera sensors. The distance between the probed planes in the object space is given by d/M_a , where M_a is the microscope's axial magnification. A field aperture in the intermediate focal plane allows to limit the detection area to avoid overlaps of the images from the projected planes.

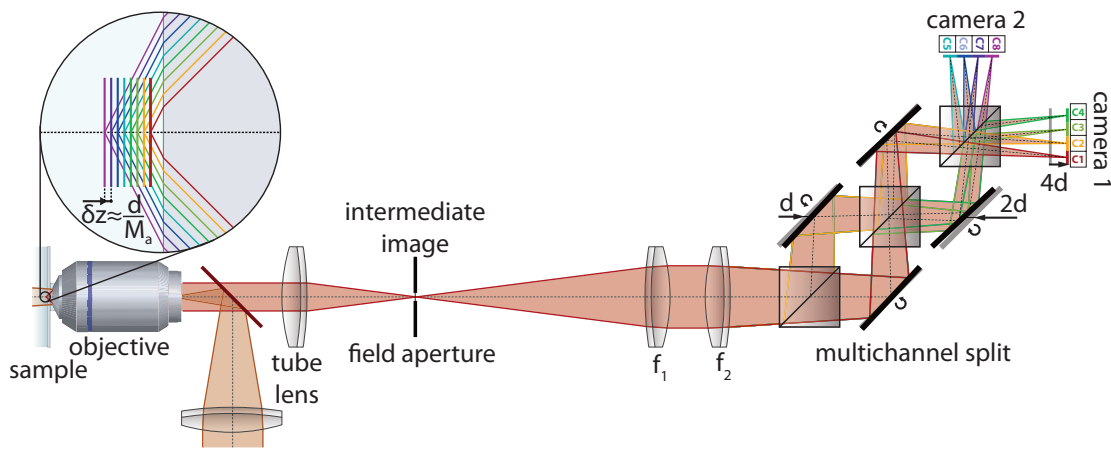


Figure 3.2: Detection part of the multi-plane epi-fluorescence microscope [57]. The image splitting is done by three beamsplitters and the images projected on two cameras. Shifting the mirrors by d and $2d$ and camera position by $4d$ as indicated in the image allows to achieve object depth separation of d/M_a , where M_a is the microscope's axial magnification. Adapted from Nature Communications 5, 5830 (2014), figure 2.

Although being flexible in tuning the interplane distances, this system showed several disadvantages. It requires frequently a careful and time-consuming alignment because the mechanical mounts of mirrors are prone to drifts. The number of interfaces light encounters upon propagation reduces the image brightness. Therefore, we proposed another design of a multi-plane microscope, where the image planes are set up by a single optical element.

Figure 4.13 shows the design of the new 3D epi-fluorescence microscope. A high numerical aperture objective is selected to maximize the photon collection efficiency and reduce PSF size. The immersion liquid matches the refraction index of the sample to avoid spherical aberrations. The tube lens TL creates an intermediate image, where a rectangular field aperture is used to limit the field of view and avoid image overlapping. An additional telescope comprising lenses T_1 and T_2 is used to project the images on the camera sensors.

3.1. Epi-fluorescence microscope and its extensions

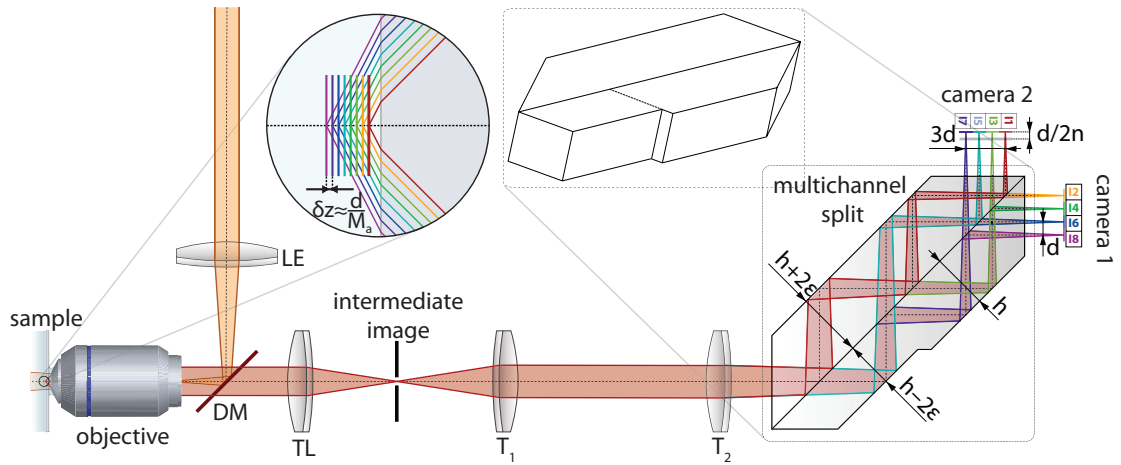


Figure 3.3: Detection part of the multi-plane epi-fluorescence microscope employing image-splitting prism. The depth separation is achieved by the different thickness of the compound prisms.

The images are separated in depth using a 2×4 image splitting prism, assembled of two plane parallel and a rhomboid prism with the sides cut at 45 degrees. A coating is used at the central cemented interface for non-polarized approximately 50:50 image splitting. The larger plane parallel, smaller plane parallel and rhomboid prisms have according thicknesses of $h + 2\varepsilon$, h , and $h - 2\varepsilon$, where $\varepsilon = \sqrt{2}d$, resulting in a lateral distance d between the neighboring images on a camera sensor. The optical path difference (OPD) accordingly corresponds to d/n , where n is the refractive index of the prism material.

In the figure 4.13 we propose an axial shift of $d/2n$ between the two cameras, resulting in an interleaved channel configuration with an OPD of $d/2n$. The camera distance can also be adjusted to $4d/n$ for a sequential channel configuration with an OPD of d/n .

3.2 ABCD matrix description of the optical setup

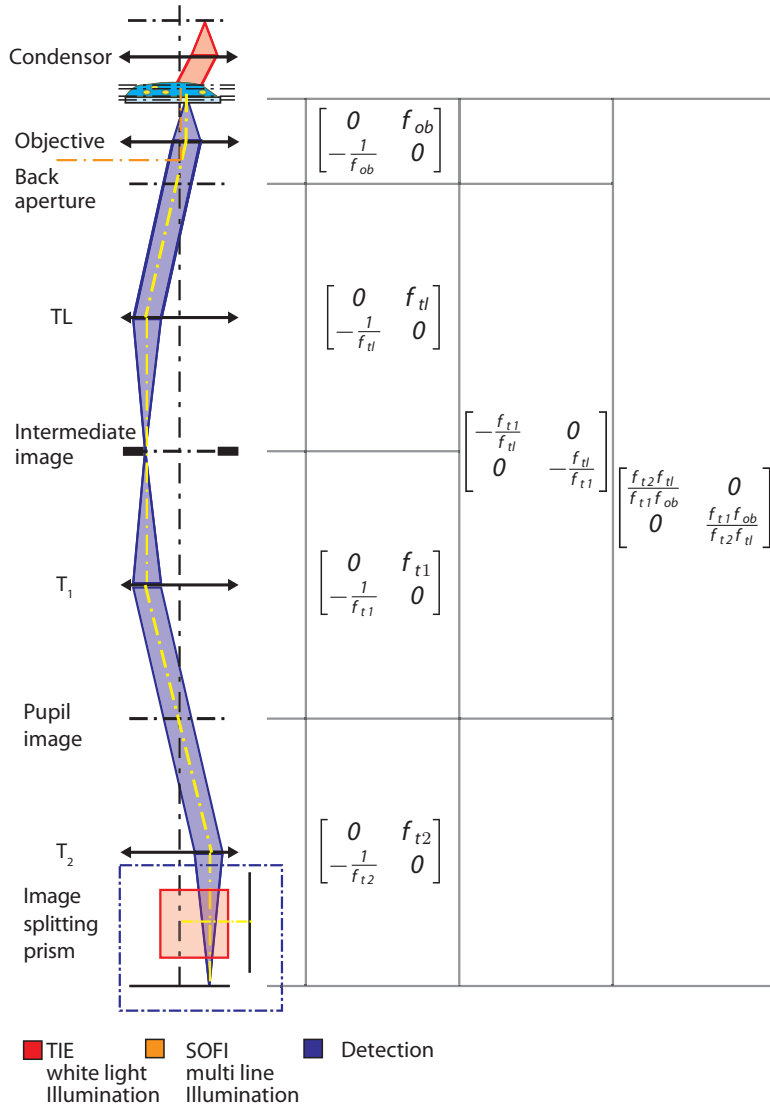


Figure 3.4: Matrix description of the multi-plane epi-fluorescence microscope

In this section we describe the system with ABCD matrix calculations. ABCD, or ray transfer matrix analysis is a convenient tool for the description of optical systems under paraxial approximation (all rays are at small angle and small distance to the optical axis). The conventions and matrices of optical elements and ray propagation are defined in the annex. The detection path of the multi-plane microscope can be represented as a combination of four 2-f configurations, as shown in figure 3.4. The transfer matrix of each configuration is found by multiplication of two propagation matrices and a refraction matrix of a thin lens. Consecutive

3.2. ABCD matrix description of the optical setup

multiplication of the four 2-f matrices yields the full description of the system \mathbb{M}_{sys} .

$$\mathbb{M}_{sys} = \begin{bmatrix} \frac{f_{i2}f_{i1}}{f_{i1}f_{ob}} & 0 \\ 0 & \frac{f_{i1}f_{ob}}{f_{i2}f_{i1}} \end{bmatrix} = \begin{bmatrix} M_{tel}M_{mic} & 0 \\ 0 & \frac{1}{M_{tel}M_{mic}} \end{bmatrix} \quad (3.1)$$

where the ratio $\frac{f_{i2}}{f_{ob}}$ gives the magnification of the microscope body M_{mic} and $\frac{f_{i1}}{f_{i1}}$ the magnification of the added telescope M_{tel} . The system is arranged as four 2-f configurations in order to provide both object and image side telecentricity. This property is confirmed by the antidiagonal elements of the system matrix, which are equal to zero. Telecentricity ensures equal magnification for all object and image planes and simplifies image co-registration in the post-processing steps as compared to the previous setup [57].

Supposing the axial displacement δ in the object plane and according displacement Δ in the opposite direction in the image plane, two additional matrices describing this translation need to be added for the full system description \mathbb{M}_{tot} :

$$\mathbb{M}_{tot} = \begin{bmatrix} 1 & -\Delta \\ 0 & 1 \end{bmatrix} \cdot \mathbb{M}_{sys} \cdot \begin{bmatrix} 1 & \delta \\ 0 & 1 \end{bmatrix} = \begin{bmatrix} M_{tel}M_{mic} & \delta M_{tel}M_{mic} - \frac{\Delta}{M_{tel}M_{mic}} \\ 0 & \frac{1}{M_{tel}M_{mic}} \end{bmatrix} \quad (3.2)$$

Fulfilling the imaging condition ($B = 0$), the displacement in the image space is determined as:

$$\Delta = M_{tel}^2 M_{mic}^2 \delta \quad (3.3)$$

When imaging different sample features or using different fluorophores with emission spectra ranging from the blue to red wavelength, different spacings between the acquired depth planes might be required to ensure the correlation between the planes, since the PSF size changes. It can be adjusted by changing the lateral magnification. Since the distance is dependent on the axial magnification, which is the square of the lateral magnification, this distance can be adjusted by changing the lenses.

In order to conserve the overall length of the system and simplify the adjustment, we propose to vary the "telescope" magnification M_{tel} by changing the focal lengths of lenses TL and T_1 and conserving the sum of their focal distance at the same time:

$$M_{tel} = \frac{f_{i1}}{f_{t1}} \quad f_{t1} + f_{i1} = const \quad (3.4)$$

It is therefore possible to adjust the spacing in a wide range, however significantly bigger or smaller distances could require too large change in magnification, which could compromise the 3D SOFI approach due to over- or under-sampling in the lateral dimension.

Chapter 3. Multi-plane setup and its configurations

As discussed in the section 3.1, an OPD between the neighboring images is determined by the prism geometry and camera arrangement and corresponds to $d/2n$ for the interleaved channel configuration (figure 4.13). The displacement Δ then also includes a coefficient α , ranging from 1 to 8, depending on the number of the plane imaged:

$$\delta = \frac{\Delta}{M_{tel}^2 M_{mic}^2} = \frac{\alpha d f_{t1}^2 f_{ob}^2}{2n f_{t2}^2 f_{tl}^2} \quad (3.5)$$

In our setup we typically used an Olympus UPLSAPO 60XW objective with a 3mm focal length, and a 200mm lens T_2 . The prism was fabricated from fused silica with a refractive index of $n \approx 1.45$ and OPD $d=3.3\text{mm}$ corresponding to a quarter of the Hamamatsu ORCA Flash-4.0 CMOS sensor. Figure 3.5 shows the dependence of the axial spacing between the planes on the focal length of lens TL (provided that the focal length of the lens T_1 is adjusted according to equation 3.4).

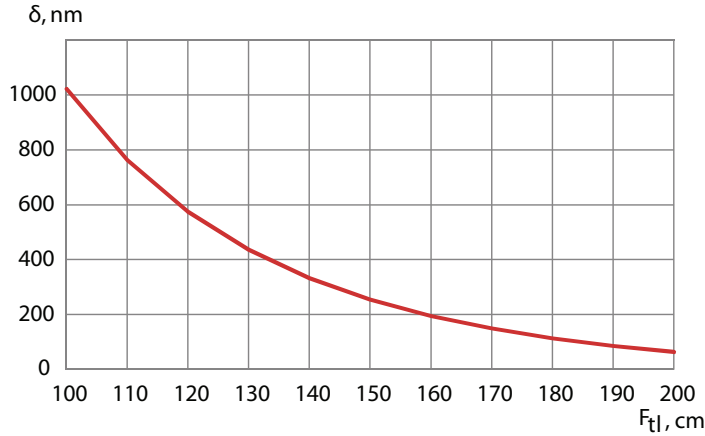


Figure 3.5: Dependence of axial spacings between the planes on the focal length of the tube lens

The PSF sampling can be described by its comparison to the scaled pixel size p - the physical pixel size of the camera sensor P ($6.5 \mu\text{m}$ for the Hamamatsu ORCA Flash-4.0 camera) divided by the system magnification:

$$p = \frac{P}{M_{sys}} = \frac{P f_{t1} f_{ob}}{f_{t2} f_{tl}} \quad (3.6)$$

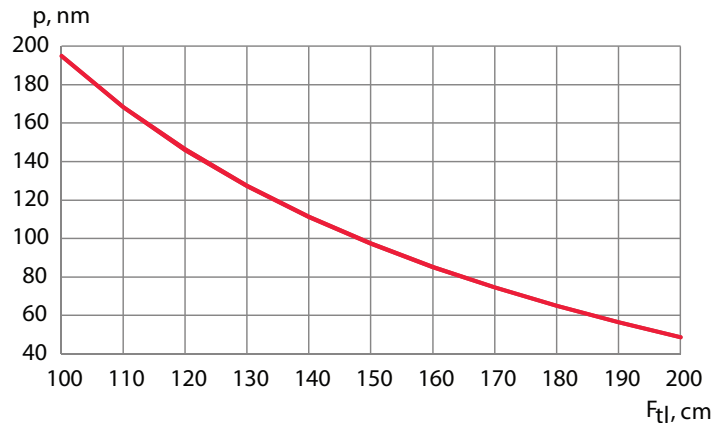


Figure 3.6: Dependence of the scaled pixel size p on the focal length of the tube lens

The proposed range of the tube lens focal lengths provides a fourfold change in the scaled pixel size p , and accordingly ~ 16 -fold change of the plane spacing.

A typical configuration includes the 140mm tube lens, and a combination of 160mm and 200mm lenses for T_1 and T_2 , yielding the spacing δ of 334nm in air, or 444nm in an aqueous environment due to the refractive index of 1.33 of water.

A larger separation could be used for non-fluorescent imaging of samples combined with phase reconstruction techniques, e.g. by the transport of intensity equation. This modality would require the according change of emission filters and trans-illumination, e.g. a Koehler illumination.

3.3 Ray tracing

In order to design the multi-plane imaging system incorporating image-splitting prism, minimize its aberrations and assess the performance for SOFI, we performed a ray tracing analysis using the optical simulation software Zemax. We have been using the sequential multi-configuration mode in order to describe the splittings at the 50:50 interface (figure 4.13). The objective was modeled as a paraxial lens, and we used achromatic doublets from Linos as the tube lens and the telescope lenses. The outline of the ray tracing through the splitting part is shown in figure 3.8. The prism was designed to provide the distance between the images according to a $13.3 \times 13.3\text{mm}^2$ sensor with a $6.5 \mu\text{m}$ pixel size. The distance between the images of 3.3 mm allows therefore the detection of images separated by $\delta Z = d/n \approx 2.1$ mm in axial direction.

Chapter 3. Multi-plane setup and its configurations

Surf:Type	Comment	Radius	Thickness	Glass	Semi-Diameter		
OBJ	Standard	Sample	Infinity	-1.167E-003	V	0.033	
1	Standard		Infinity	3.000		0.034	
2	Paraxial	Objective		3.000		3.631	
STO	Standard	Aperture stop	Infinity	138.000		3.600	U
4*	Standard	TL Linos	87.222	6.000	N-BK7	15.750	U
5*	Standard	140mm	-61.748	2.000	N-SF5	15.750	U
6*	Standard	322239322	-177.830	138.000		15.750	U
7	Standard	Field stop	Infinity	156.037		1.544	
8*	Standard	T1 Linos	203.162	2.600	N-SF5	15.750	U
9*	Standard	160mm	70.543	6.000	N-BK7	15.750	U
10*	Standard	322270322	-99.646	158.649		15.750	U
11	Standard		Infinity	199.000		4.118	
12*	Standard	T2 Linos	120.570	4.000	N-BK7	11.200	U
13*	Standard	200mm	-91.728	2.000	N-SF5	11.200	U
14*	Standard	322328000	-277.810	60.000		11.200	U
15*	Standard	Image splitter	Infinity	11.313	C79-80	11.313	U
16#	Standard	50:50	Infinity	0.000	MIRROR	16.000	U
17	Coordinat..			-22.627	-	0.000	
18	Coordinat..			0.000	-	0.000	
19#	Standard		Infinity	0.000	MIRROR	16.000	U
20	Coordinat..			22.627	P	0.000	
21	Coordinat..			0.000	-	0.000	
22#	Standard	50:50	Infinity	0.000	MIRROR	12.000	U
23	Coordinat..			-22.627	-	0.000	
24	Coordinat..			0.000	-	0.000	
25#	Standard		Infinity	0.000	MIRROR	11.313	U
26	Coordinat..			22.627	P	0.000	
27	Coordinat..			0.000	-	0.000	
28#	Standard	50:50	Infinity	0.000	C79-80	6.600	U
29	Coordinat..			4.668	-	0.000	
30*	Standard		Infinity	65.637	V	4.668	U
IMA	Standard		Infinity	-		1.911	

Figure 3.7: Lens editor description of the optical system. The objective, lenses TL, T₁, T₂, and image splitter are highlighted by red. For each surface, the radius, thickness, glass type and semi-diameter are indicated.

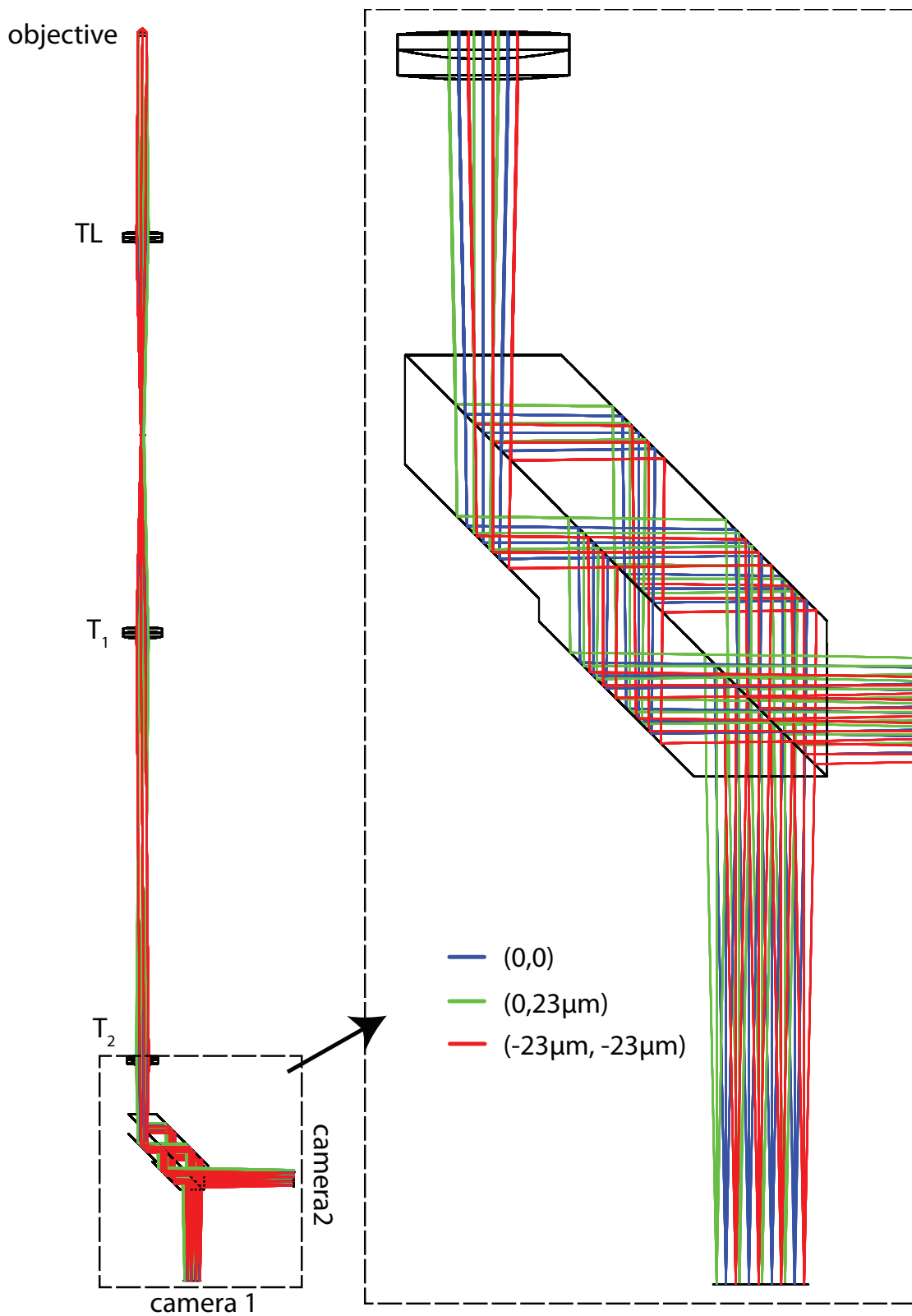


Figure 3.8: Ray tracing diagram. Colors of the rays correspond to the indicated field points.

Chapter 3. Multi-plane setup and its configurations

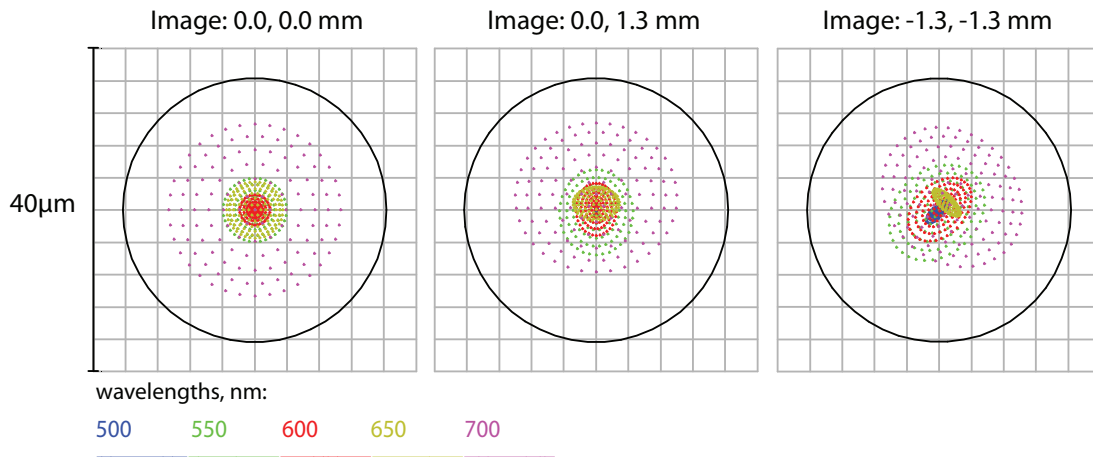


Figure 3.9: Spot diagrams for 3 field points. Colors correspond to the 500 - 700nm wavelengths. The Airy radius is indicated by a black line and equal to 18.4 μm .

In order to estimate the PSF size, the corresponding spot diagrams for all eight images were calculated (figure 3.9). The size of the geometrically traced spots is well below the Airy radius, therefore the system is diffraction limited for the wavelength range from 500 to 700 nm. The marginal field point positions for all images differ only within several percents of the PSF, providing therefore pixel-to-pixel correspondence between the different depth planes.

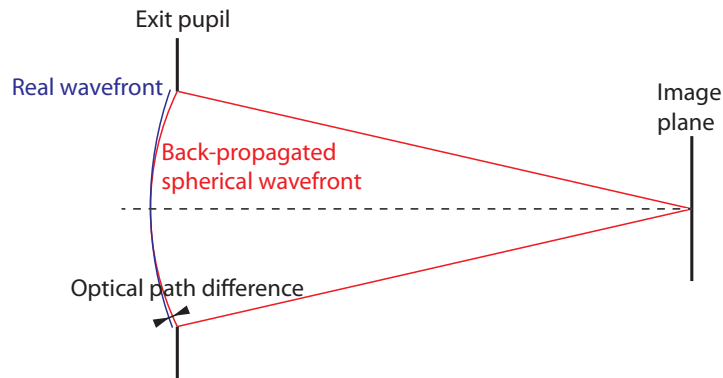


Figure 3.10: Optical path difference, observed at the system exit pupil.

An aberration is a deviation from the best possible performance given by a perfect point-to-point imaging in geometrical optics. A convenient way to describe the aberrations is the OPD diagram, which shows the optical path difference between the ideal case (back-propagated spherical wavefront) and the true wavefront as traced through the system (figure 3.11).

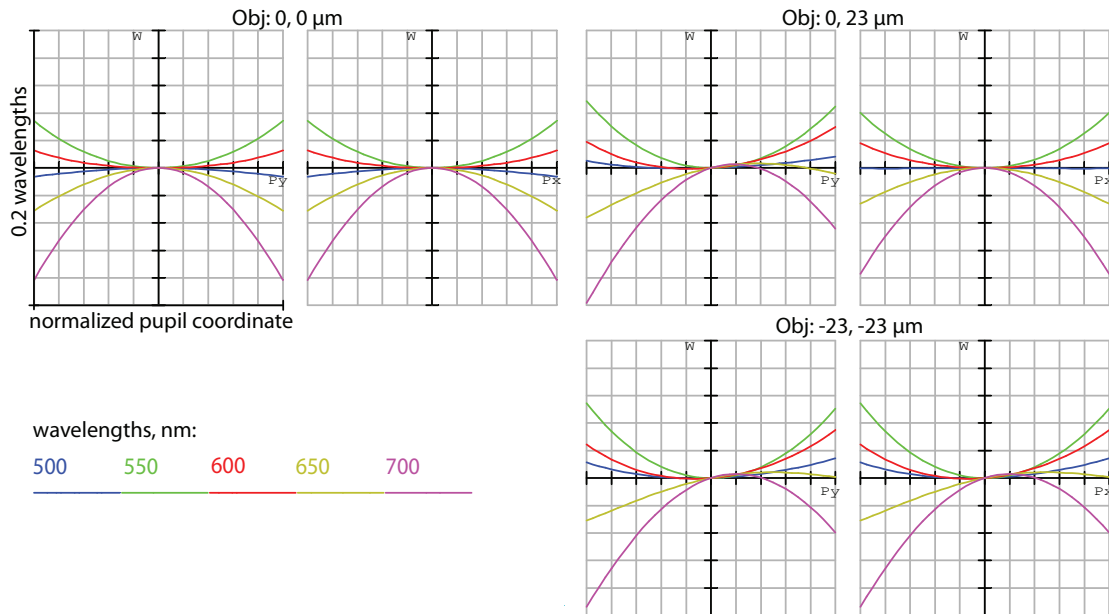


Figure 3.11: OPD diagrams for 3 field points. Colors correspond to 500 - 700nm wavelengths as indicated. The maximum scale of OPD corresponds to 0.2 wavelengths. The maximum scale of P_x and P_y corresponds to the normalized pupil coordinate in the corresponding dimension.

Another way to describe the aberrations of a rotationally symmetric system was provided by Philipp Ludwig von Seidel in 1857. Given the system with a pupil radius a , pupil coordinates r, θ , and image height h' , the primary aberration function is written as follows:

$$W(r, \theta, h') = {}_0a_{40}r^4 + {}_1a_{31}h'r^3 \cos \theta + {}_2a_{22}h'^2r^2 \cos^2 \theta + {}_2a_{20}h'^2r^2 + {}_3a_{11}h'^3r \cos \theta \quad (3.7)$$

where a are the aberration coefficients, corresponding to the 5 Seidel aberrations: ${}_0a_{40}$ - spherical aberration, ${}_1a_{31}$ - coma, ${}_2a_{22}$ - astigmatism, ${}_2a_{20}$ - field curvature, and ${}_3a_{11}$ - distortion. The subscripts of the aberration coefficients a correspond to the powers of h' , r , and $\cos \theta$. The sum of these powers is equal to four, so these aberrations are also referred to as 4-th order wavefront aberrations [63].

The spherical aberration, coma and astigmatism describe the deviation of the wavefront from the reference sphere and therefore have direct impact on the PSF size. The field curvature and distortion correspond to the change of radius and direction of the wavefront - which affects the image position.

By definition, Seidel aberrations are calculated for monochromatic light. Polychromatic aberrations can be described by axial and lateral chromatic aberrations. Axial, or longitudinal chromatic aberration, describes the inability of an imaging system to focus different colors in the same focal plane. When imaging a point source situated on the optical axis, images for different colors are displaced along the axis. Lateral, or transverse chromatic aberration, disperses the focus closer or further from the optical axis. In an imaging system, this results in

Chapter 3. Multi-plane setup and its configurations

a color-dependent magnification.

A Seidel diagram for the multi-plane setup is shown in the figure 3.12. We considered a wavelength range from 500 to 700 nm, and used a reference wavelength of 600 nm for the calculation of the Seidel coefficients. The axial color aberration dominates, and is the only aberration exceeding 50 nm. However, in practice the wavelength range is limited to a particular marker emission spectrum, and the effect of this aberration is decreased.

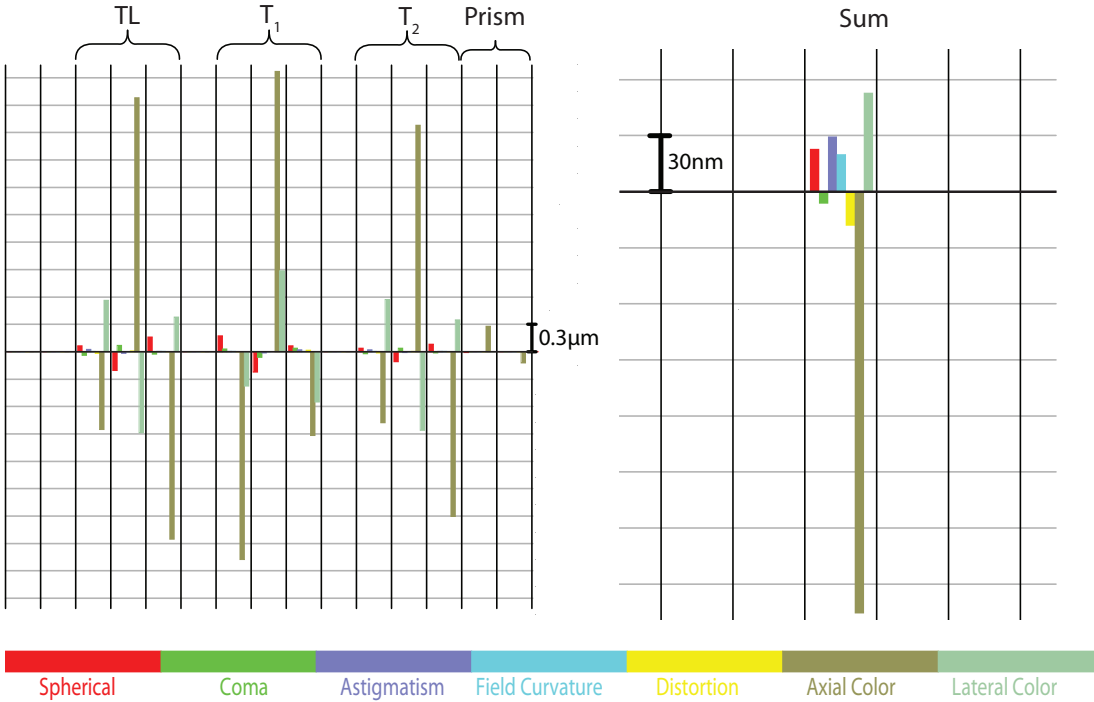


Figure 3.12: Seidel diagram. The grid lines are spaced by 300nm and 50nm for the system and zoomed sum accordingly.

3.4 Experimental characterization:

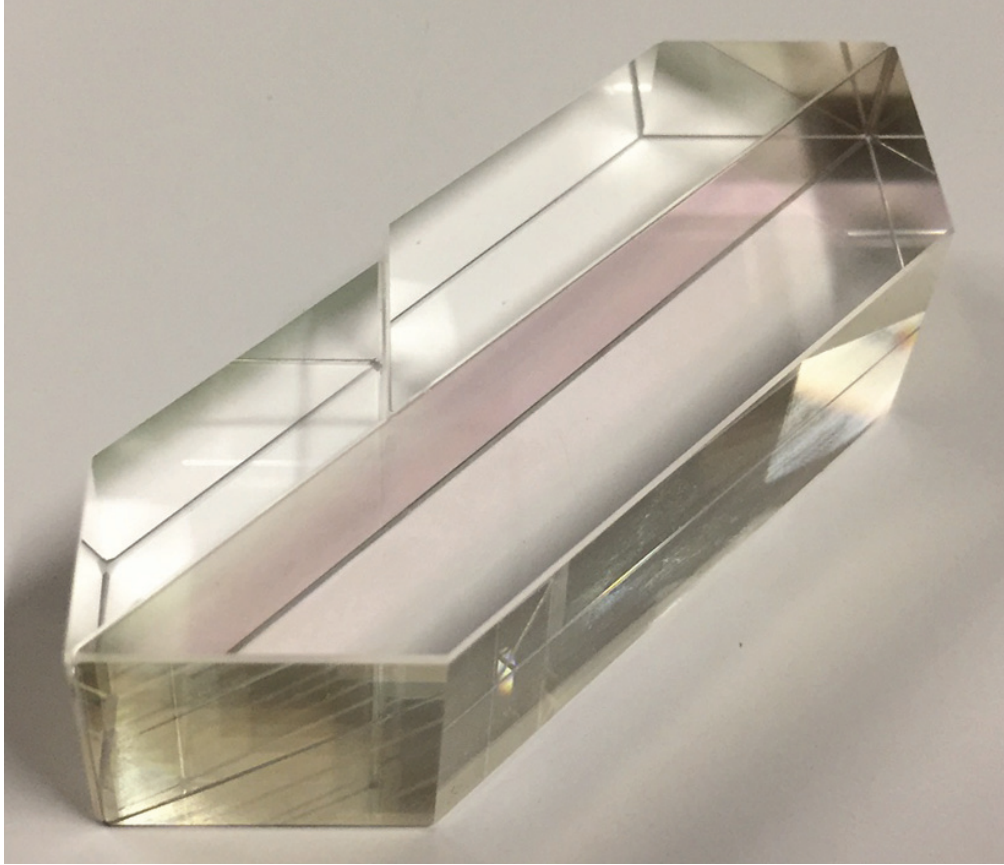


Figure 3.13: Photo of the manufactured prism.

The image-splitting prism was custom-manufactured at SCHOTT Suisse Sa Yverdon facility. The overview photo of the image-splitting prism used is shown in figure 3.13. The prism was then integrated in the setup described in figure 4.13. For the characterization we used fluorescent beads (PS-Speck, Thermo Fisher Scientific) with 175nm diameter were deposited on a coverslip surface, covered with mounting medium and used as a calibration sample. We did a stepped scan in axial direction, taking images of 8 planes after every 200nm step.

3.4.1 Lateral image displacement in beamsplitter

In order to characterize the lateral image displacement in the image splitter, we co-registered the beads' images in neighboring axial planes/channels. The co-registration was done by spatial cross-correlation between the corresponding beads in neighboring channels. We calculated the affine transformations, which were further used for the data co-registration. The diagram for the plane co-registration is shown in figure 3.14.

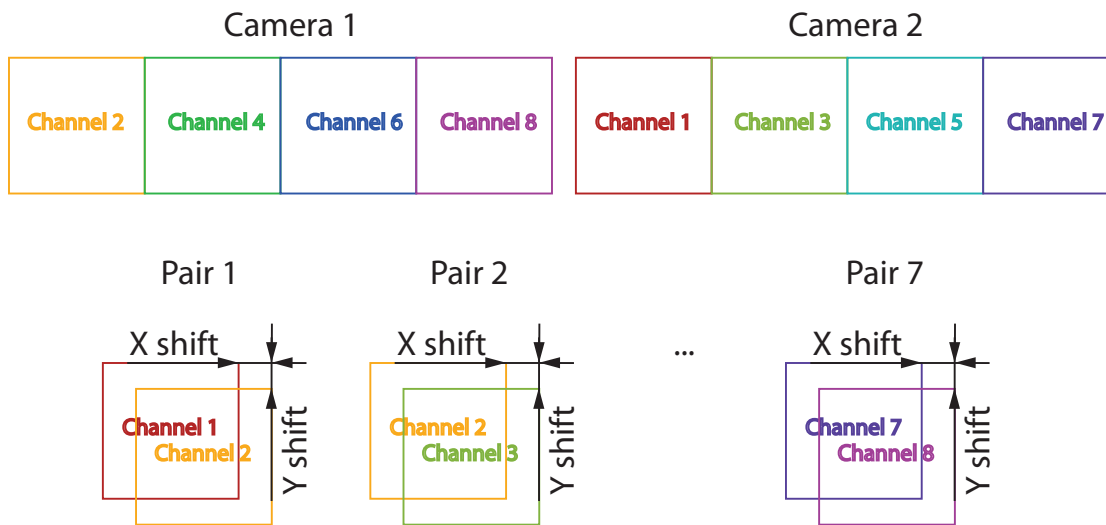


Figure 3.14: Channel registration diagram. For each pair of acquired neighboring planes, a transformation matrix and according lateral shifts are calculated.

An example co-registered image of the bead sample is shown on figure 3.15.

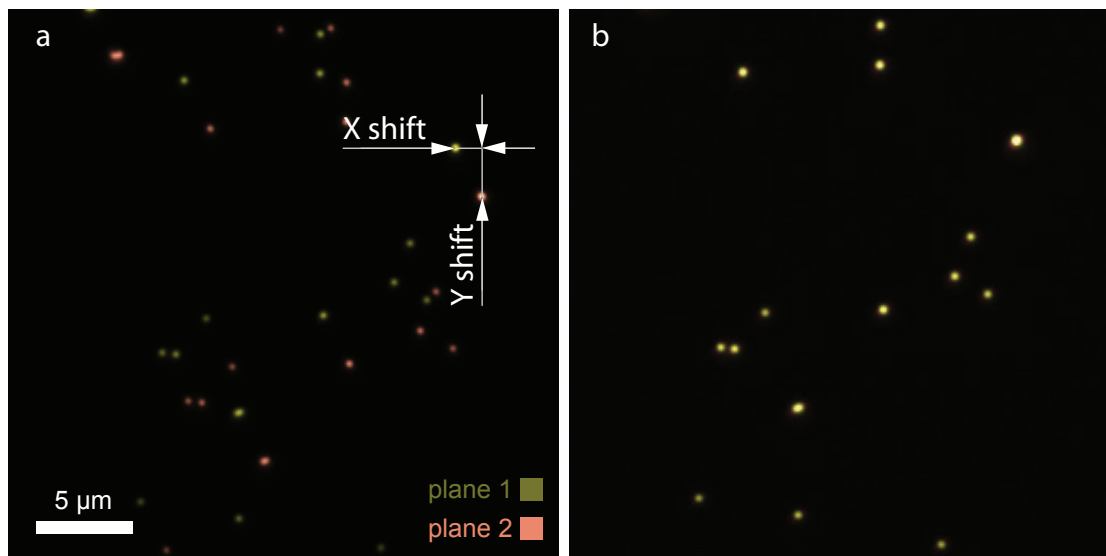


Figure 3.15: Two co-registered images of beads, acquired by the adjacent channels, color-coded in depth. (a) Overlaid images before the registration. Arrows indicate the lateral shift between the images of the same bead. (b) Overlaid images after the co-registration.

As the figure shows, the co-registered beads overlap almost perfectly. The lateral displacements, indicated on the figure 3.15 were extracted from the transformation matrices and summarized in the following table, where the shifts are specified as the distances in the image and object planes accordingly:

3.4. Experimental characterization:

Plane pair	X shift, μm		Y shift, μm	
	image space	object space	image space	object space
1,2	70.5	1.2	-302.9	-5.2
2,3	-65.8	-1.1	321.4	5.5
3,4	69.5	1.2	-298	-5.1
4,5	-134.3	-2.3	134.9	2.3
5,6	69.9	1.2	-293.6	-5.0
6,7	-66.3	-1.1	308.7	5.3
7,8	69.7	1.2	-288.5	-4.9

Table 3.1: Lateral shifts, obtained from co-registration of the depth planes. Shifts indicated in image and object space, given the magnification $M_{lat} = 58.3\times$.

3.4.2 Interplane distances

The distances between the successive planes define the depth of the final reconstructed image. It is also crucial for 3D SOFI approach, since the signal cross-correlation between the planes must be ensured. We determined these distances from the scan of the sample with fluorescent beads. The average brightness response was calculated for each plane and plotted versus the axial position of the stage. Each plot was fitted by Gaussian in order to localize the maximum, corresponding to the plane focus position during the scan (figure 3.16). The difference between the Gaussian maxima corresponds to the distance between the planes, as indicated in the table.

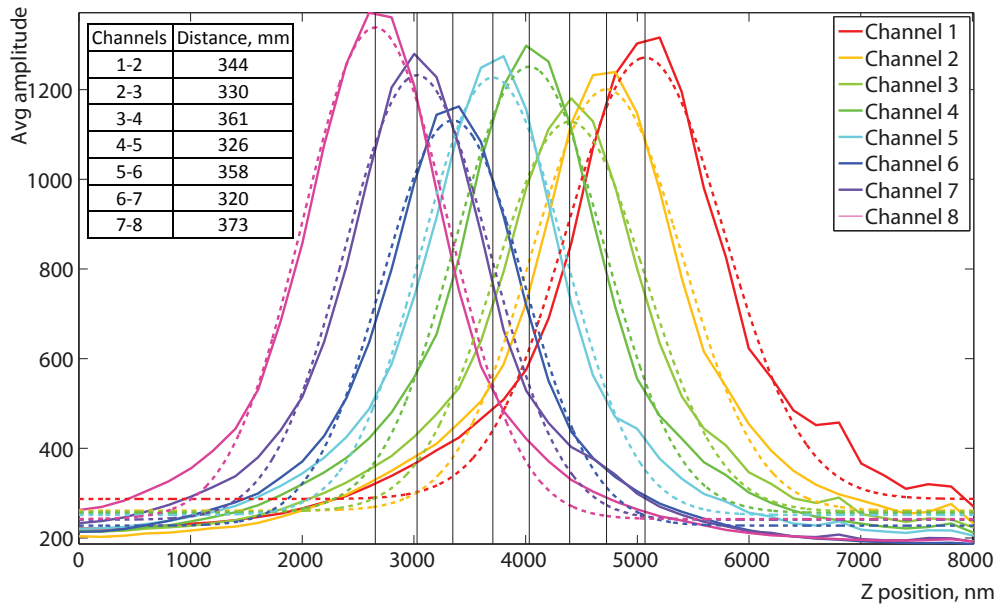


Figure 3.16: Average brightness response per plane, fitted by Gaussian. The table shows the measured interplane distances.

Chapter 3. Multi-plane setup and its configurations

The average distance is 345nm, and the standard deviation is 20nm, which is in correspondence with a theoretical value of 334nm. The non-uniformities can come from non-ideal prism component thicknesses, and positioning errors of the scanning stage. The overall image depth in an aqueous environment then yields about 3.2 μm .

3.4.3 PSF characterization

The full width at half maximum (FWHM) of the PSF in lateral extent is determined as the FWHM of Airy function:

$$d_l = 0.51 \frac{\lambda}{NA} \quad (3.8)$$

The axial extent of the PSF is determined from the scalar model by Born and Wolf [64] as:

$$PSF_z(z) = I_0 \text{sinc}^2\left(\frac{NA^2 z}{2\lambda n}\right) \quad (3.9)$$

where n is the refractive index of the medium, 1.33 for aqueous solution, and 1.2 is the numerical aperture NA . The calculations yield 240nm and 283nm in the lateral dimension, and 916 and 1080 in the axial dimension.

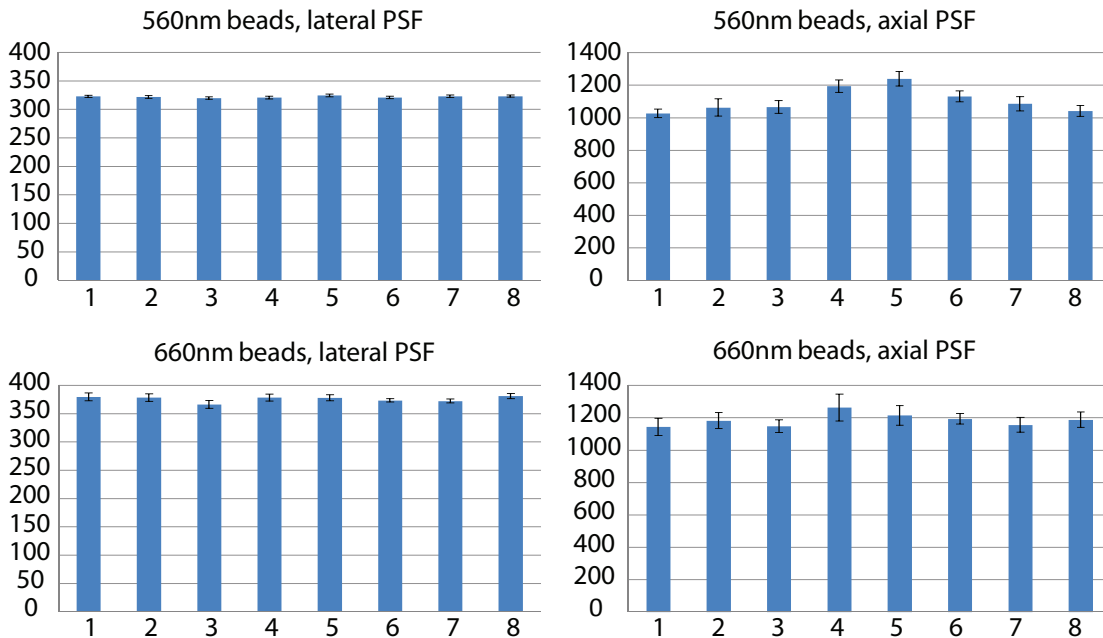


Figure 3.17: FWHMs in axial and lateral dimensions measured with orange and deep red fluorescent beads

The PSF characterization was done with orange (emission maximum at 560nm) and deep

3.4. Experimental characterization:

red (emission maximum at 660nm) fluorescent beads (Thermo Fisher Scientific) dried and mounted on 170 μm thick coverslip, so that there was several tens of sparse beads per field of view. The scan was done in the z direction using 200nm steps. To characterize the PSF in all 3 spatial dimensions, 3 dimensional Gaussian fit was applied to each detected sparse bead, averaged over all beads per channel, and FWHMs were extracted. The results are summarized in figure 3.17.

The extracted FWHM average values for orange and red beads accordingly are 322nm and 376nm in the lateral dimension, and 1106 and 1187 in the axial dimension. The difference between the theoretical and experimentally measured PSFs most likely occurs due to the finite size of the beads used.

3.4.4 Brightness response

An average brightness response per channel was extracted using the scan data with orange and deep red fluorescent beads and Gaussian fitting, as described in section 3.4.2. The relative amplitudes of Gaussians correspond to the channel brightness response, while the vertical offset corresponds to the ADC bias with an out of focus background. The extracted relative amplitudes were subsequently used as a weighting factor for each channel in order to equalize the channel brightness responses.

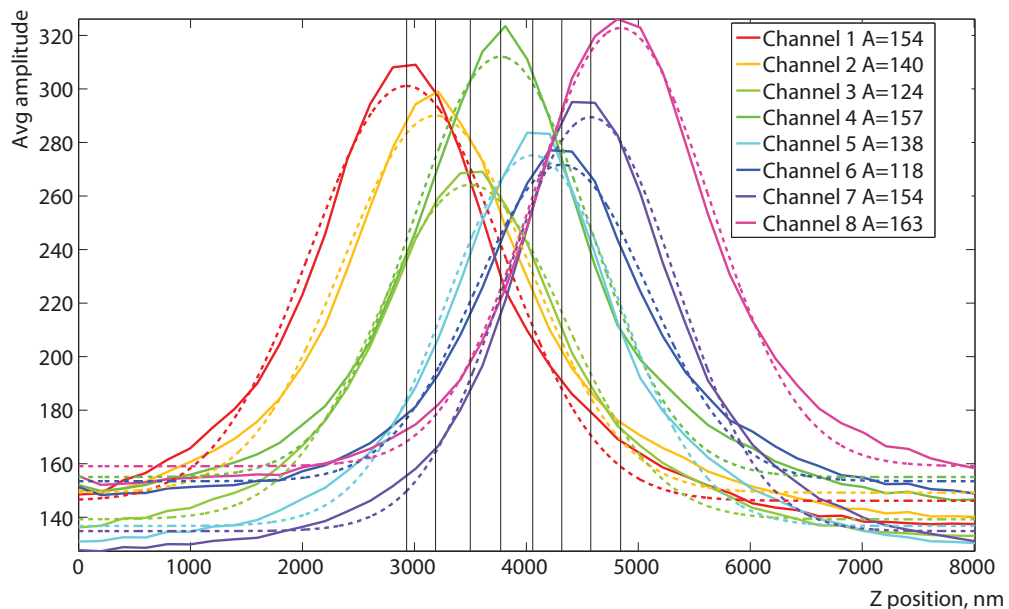


Figure 3.18: Average brightness response measured with deep red fluorescent beads

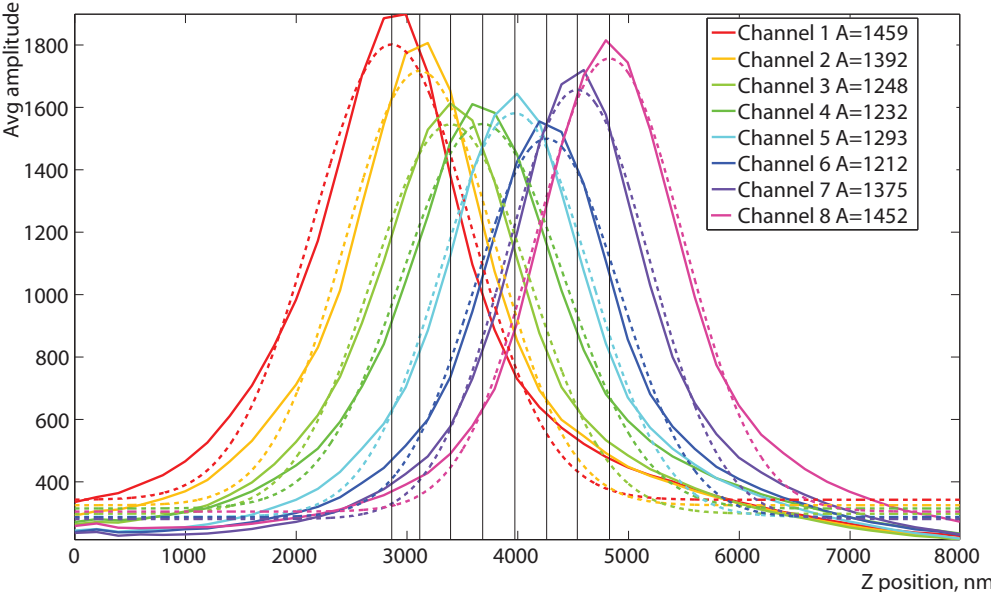


Figure 3.19: Average brightness response measured with orange fluorescent beads

4 SOFI imaging

Optimal imaging conditions are not solely determined by the quality of the imaging system but are also dependent on the quality of the sample. Section 4.1 describes the different fluorescence staining methods used in this thesis. Section 4.2 focuses on the optimization of the blinking conditions for SOFI via excitation adjustment. In sections 4.3, 4.4, and 4.5 we discuss the imaging of fixed cells, live bacteria, and live cells accordingly.

4.1 Sample preparation

4.1.1 Immunofluorescence

Immunofluorescence is a method for qualitative and quantitative staining of cell membranes, subcellular structures, bacteria and tissue samples. Biological samples can then be analyzed for the presence and amount of antigens with the help of a fluorescence microscope if antibodies are conjugated with the fluorescent markers [65]. The initial sample preparation (cell fixation) is crucial for conserving the cell morphology and maintaining antigenicity of the targeted epitopes.

Depending on cell type and antibodies used, the unspecific binding tends to increase background. In this case a blocking buffer is required. If blocking is necessary, we used a bovine serum albumin (BSA) solution. When staining intracellular structures, cell membrane permeabilisation is required to allow antibodies to reach the interior of the cell. The Triton X-100 or Tween-20 reagents were used to perform this permeabilisation.

Direct and indirect antibody labeling strategies are possible. When using the direct staining method, the sample is incubated with a solution of fluorophore labeled primary antibodies. The formed antigen-antibody complexes can be detected via the fluorescent signal (figure 4.1).

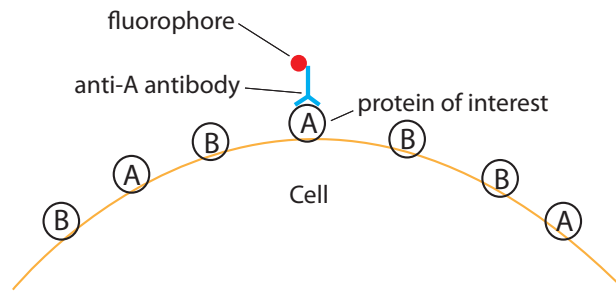


Figure 4.1: Direct antibody staining

In the widely applied indirect staining method, the sample is first exposed to unlabeled primary antibodies against the antigens of interest and then, in a second step, by species-specific secondary antibodies. The fluorescently labelled secondary antibodies should then be raised against the Immunoglobulin G (IgG) of the primary antibody species. Since several secondary antibodies can bind to one primary antibody, the fluorescence signal can be amplified.

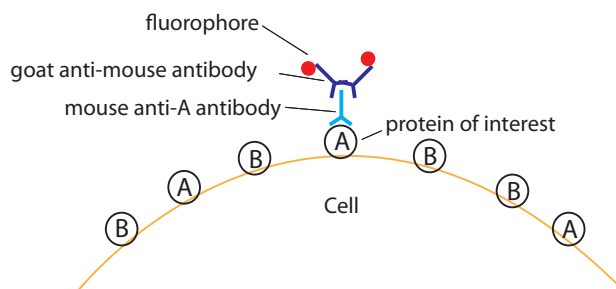


Figure 4.2: Indirect antibody staining

4.1.2 Transfection and expression of fluorescent proteins

Antibody staining is generally not compatible with live cell imaging as the typical antibodies cannot penetrate the living cell membrane. In contrast, fluorescent proteins are almost ideal biomarkers for living cell labeling [66].

Cell transfection is a well-developed method for targeting proteins of interest. Transfection stands for a variety of methods integrating a foreign DNA at least in part into a cell. We mainly used lipofection and electroporation, where lipofection uses liposomes, i.e., small vesicles that can merge with the cell membrane and deliver their cargo into the cell. A standard transfection reagent, Lipofectamine, contains lipid subunits that form liposomes while entrapping the DNA in an aqueous environment. Another possibility is Fugene, a lipid-based reagent. In contrast, electroporation enables the temporary permeability of a cellular membrane by submitting the cell to short and intense electric pulses, such that foreign DNA can diffuse into the cell.

The introduced DNA or plasmid serves as a cloning vector for amplifying and/or expressing a specific protein. Fluorescent proteins expression is used for fluorescence microscopy with a variety of photoswitchable fluorescent proteins (see also section 2.2.3).

4.1.3 Direct labeling with cell-permeant probes

Specific cell-permeant probes such as Mitotracker Orange provide a direct and simple way for cell staining. The sample is incubated with a dye solution, followed by several washing steps. Mitotracker probes diffuse through the plasma membrane and accumulate in living mitochondria [67].

4.1.4 Sample preparation protocols

The following table summarizes the samples and their preparation description used in this thesis:

Sample	Fluorophore	Cell type	Target structure	Labelling method
1	Dreiklang	Hela	Vimentin	Fugene
2	Dreiklang	Hela	Actin	Lipofectamine
3	Dreiklang	Hela	Keratin	Fugene
4	Mitotracker	Hela	Mitochondria	Direct
5	Alexa 647	Hela	Microtubuli	Secondary antibody
6	rsEGFP	E.Coli	MreB	Stable line
7	Dreiklang	M.smegmatis	FtsZ	Stable line
8	Alexa 647	Microglia	Membrane	Secondary antibody

Cell preparation

Hela cells were incubated at 37°C at 5% CO₂ in a Minimum Essential Medium (MEM) Eagle completed with Earle's salts, L-glutamine, sodium bicarbonate complemented with 10% fetal bovine serum, 1× penicillin-streptomycin, 1× GlutaMAX, 1× MEM Non-Essential Amino Acids Solution. The cells were plated in 35mm glass bottom FluoroDishes (World Precision Instruments Inc.).

Fugene transfection

Transfection was performed one day after the cells plating, when cells reach ≈80% confluency. 6µl of Fugene were incubated in 92 µl OptiMEM for 5 minutes. 2 µg of DNA were subsequently added to the solution, followed by 30 minute incubation at room temperature. For each dish, the cell medium was exchanged for the fresh one. The Fugene solution was then distributed in small droplets over the surface of the dish. The dishes were then put back into the incu-

Chapter 4. SOFI imaging

bator, and imaged the next day. We used DMEM_{gfp-2} (BioCat) antibleaching cell medium, complemented with 1% rutin solution during imaging. This medium reduces the background fluorescence and Dreiklang bleaching compared to the normal cell medium.

Mitotracker staining

Mitotracker staining was performed one day after plating the cells. Mitotracker was diluted to 400nM concentration in Hank's balanced salt solution (HBSS). After washing the cells with 37°C prewarmed 1× PBS, the cells were incubated with Mitotracker for 10 minutes at 37°C. The cells were then washed three times with 37°C prewarmed HBSS and imaged immediately afterwards. HBSS allows to reduce the background fluorescence compared to the normal cell medium.

Antibody staining

One day after plating, HeLa cells were washed with 37°C prewarmed PBS and then fixed by incubation with 37°C prewarmed 4% paraformaldehyde (PFA) solution. The cells were then washed three times with PBS. Meanwhile the blocking buffer, containing 3% bovine serum albumin (BSA) and 0.25% Triton-X 100 in PBS was prepared. We also prepared the washing buffer, containing 0.2% BSA and 0.05% Triton-x 100.

The cells were then incubated for 30 minutes in the blocking buffer. The primary antibody (DM1A, against microtubuli, raised in mouse) was diluted to 1/100 concentration in the blocking buffer. The cells were incubated with the primary antibody for 45 minutes, followed by three times washing in the washing buffer. The secondary antibody (Alexa 647 anti-mouse, Invitrogen) was diluted to 1/200 concentration in the blocking buffer. After 45 minutes incubation with the secondary antibodies, the cells were washed three times with the imaging buffer.

The medium was then replaced for 1× PBS for further imaging, or by 50:50 PBS Glycerol solution for the long-term storage.

Imaging buffer

The imaging buffer for the samples stained with Alexa dyes contained reducing and anti-oxidizing agents. We used 20mM Cysteamine (Sigma-Aldrich) solution as a reducing agent, and 0.5 mg/ml glucose oxidase combined with 40 µg/ml catalase as an oxygen scavenger. The solution was prepared using 50 mM Tris buffer at pH 9.0 containing 6% glucose and 10mM NaCl.

4.2 Optimizing imaging conditions

Using the appropriate fluorophore blinking conditions is crucial for SOFI imaging. In this section we describe the selection of the illumination intensities by the examples of rsEGFP and Dreiklang fluorescent protein labelling. In order to determine the optimal imaging conditions, we performed ensemble switching experiments with the 2D SOFI setup (figure 3.1).

rsEGFP has two absorption bands, around 490nm for fluorescence excitation and switching off and around 396nm for back-switching into the on-state [66]. In order to determine the switching kinetics, we used a laser illumination at 405 and 488nm wavelengths. The sample was exposed to a continuous illumination at 488nm wavelength and pulsed illumination at 405nm with intensities adjusted to 0.02 W/cm^2 and 0.05 W/cm^2 . The recorded images were thresholded to segment and analyze only regions containing rsEGFP (figure 4.3). The average fluorescence intensity was extracted and background corrected by subtracting the average response from non-thresholded area, as plotted in figure 4.4 on the top graph.

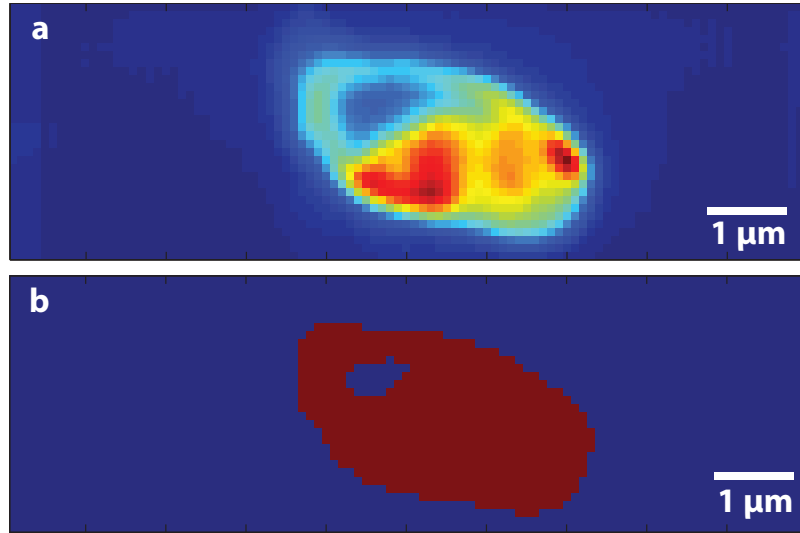


Figure 4.3: Thresholding the region containing fluorescent proteins.(a) Recorded image. (b) Red region shows the thresholding mask.

The average fluorescence intensity during continuous exposure to 488nm excitation is then proportional to the population of the off state, and the intensity during continuous exposure to 405 and 488nm excitation corresponds to the population of the on state. The rate equation is given as $\partial P/\partial t = \mathbf{Q} \cdot P(t)$, where \mathbf{Q} is the transition rate matrix. For the two-level system it is written down as follows:

$$\begin{bmatrix} \partial P_{on}/\partial t \\ \partial P_{off}/\partial t \end{bmatrix} = \begin{bmatrix} -k_{off} & k_{on} \\ k_{off} & -k_{on} \end{bmatrix} \cdot \begin{bmatrix} P_{on}(t) \\ P_{off}(t) \end{bmatrix} \quad (4.1)$$

Chapter 4. SOFI imaging

The state evolution is then obtained by Laplace transform, yielding $P_{on}(t) = P_{on}(t_0) + (P_{on}(\infty) - P_{on}(t_0)) \exp(-(k_{on} + k_{off})(t - t_0))$. To extract the switching rates $k_{on} = 1/\tau_{off,m}$ and $k_{off} = 1/\tau_{on,m}$, fluorescence on- and off-switching curves were averaged over several switching cycles and fitted to an exponential curve (figure 4.4, bottom graph).

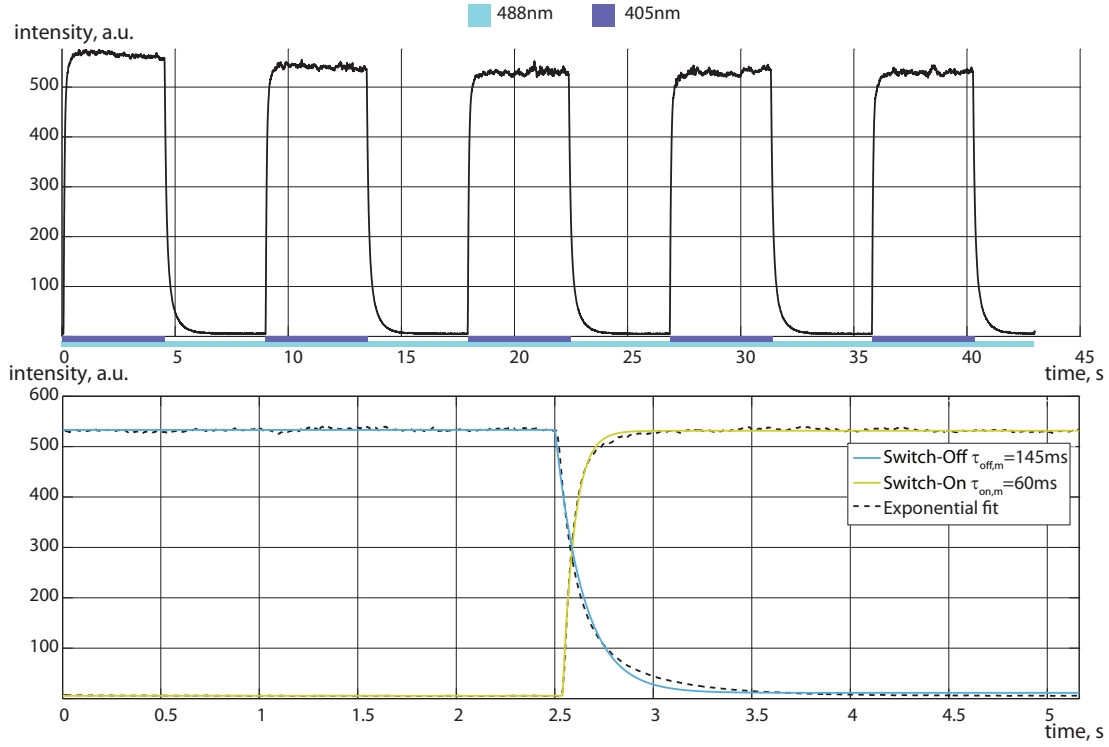


Figure 4.4: Average signal under exposure to continuous 488nm and pulsed 405nm illumination. Averaged switching curves are fitted by an exponential model function.

The measured switch-off rate corresponds to the molecular off switching and the measured switch-on rate corresponds to the sum of molecular on- and off-switching rates (since the on-switching 488nm illumination was continuous):

$$\frac{1}{\tau_{off,m}} = \frac{1}{\tau_{off}} \qquad \frac{1}{\tau_{on,m}} = \frac{1}{\tau_{off}} + \frac{1}{\tau_{on}} \quad (4.2)$$

The individual lifetimes are then extracted as follows:

$$\tau_{off} = \tau_{off,m} = 145 \text{ ms} \qquad \tau_{on} = \frac{\tau_{on,m} \tau_{off,m}}{\tau_{off,m} - \tau_{on,m}} = 102 \text{ ms} \quad (4.3)$$

As mentioned in section 2.2.3, Dreiklang possesses three absorption bands, a separate band for on-switching, off-switching and fluorescence excitation [52] at 365nm, 405nm, and 515nm accordingly.

4.2. Optimizing imaging conditions

Due to UV-light induced background, Dreiklang requires a more sophisticated approach for kinetics extraction [57]. We used transfected Hela cells expressing Dreiklang in vimentin structure for the ensemble switching experiments. We used a 365nm LED and 405nm laser corresponding to the on- and off-switching absorption maxima with intensities adjusted to 1.6 and 5.6 W/cm² accordingly. 532nm laser with an intensity of 0.7 W/cm² was used for fluorescence excitation above the absorption maximum (515nm) in order to completely avoid off-switching at the same time. In order to determine the on-ratios $\rho_{on} = \tau_{on}/(\tau_{on} + \tau_{off})$ for 365nm and 405nm illuminations, the sample was exposed to a repeated sequence of pulses of 532-405-532-365nm light. The recorded images were then background corrected and thresholded in order to segment regions containing Dreiklang. The signal plotted in the figure 4.5 shows the averaged fluorescence intensity.

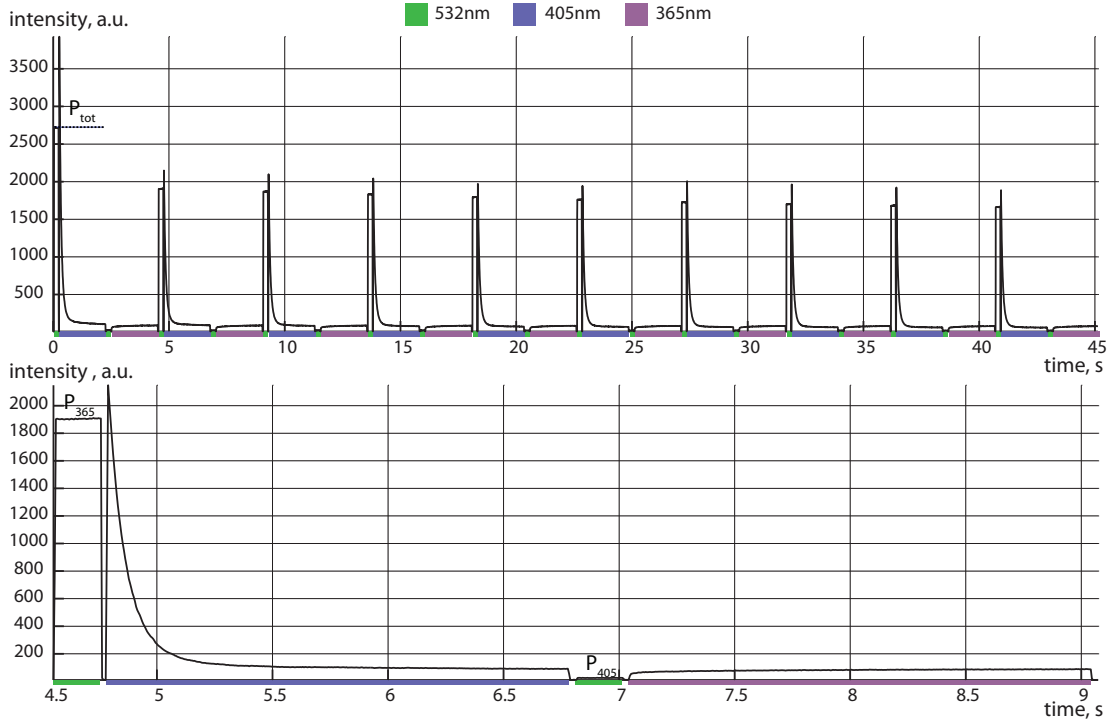


Figure 4.5: Averaged signal after exposure to 532-405-532-365nm illumination.

The signal recorded during the exposure to 532nm illumination then corresponds to the population P_{365} or P_{405} as set up by the preceding illumination pulse. The total population P_{tot} is extracted from the first exposure to 532nm illumination. The on-ratios then correspond to the according population ratios:

$$\frac{P_{365}}{P_{tot}} = \rho_{on,365} = \frac{\tau_{on,365}}{\tau_{on,365} + \tau_{off,365}}, \quad \frac{P_{405}}{P_{tot}} = \rho_{on,405} = \frac{\tau_{on,405}}{\tau_{on,405} + \tau_{off,405}} \quad (4.4)$$

In order to extract the absolute lifetimes, the sample was exposed to a continuous illumination

Chapter 4. SOFI imaging

by 405 and 532nm and pulsed 365nm light. The recorded images were treated identically to the first experiment. The switch-on and switch-off curves were then averaged and fitted by an exponential model function (figure 4.6).

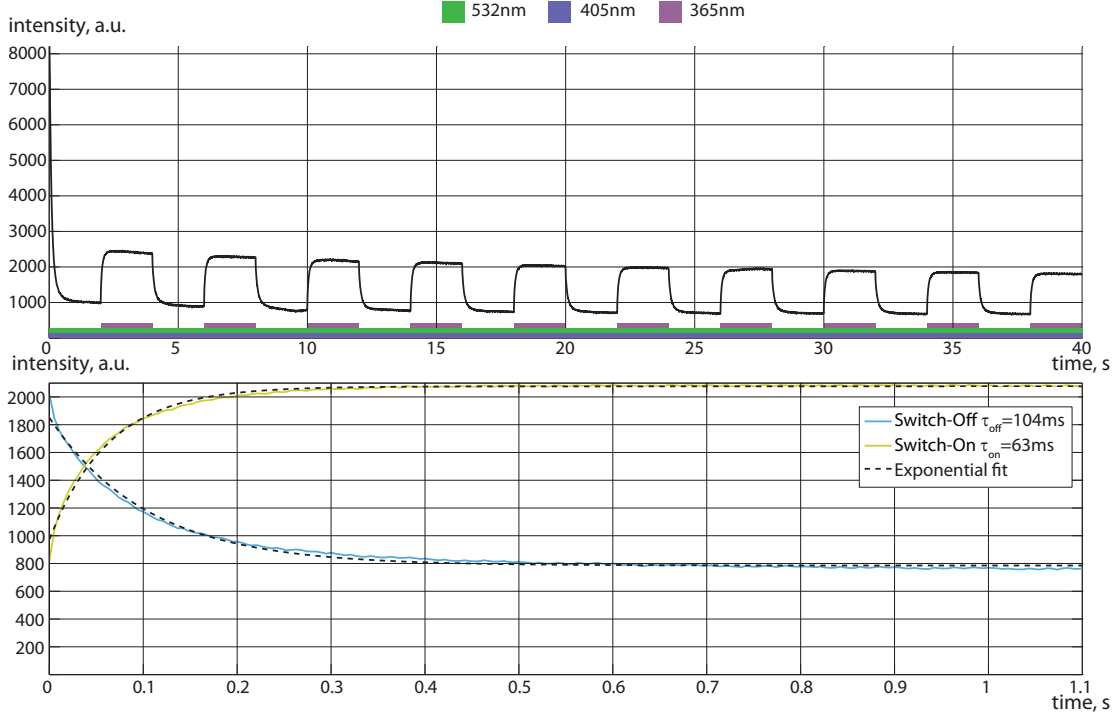


Figure 4.6: Averaged signal after exposure to constant 405 and 532nm, and pulsed 365nm illumination. Averaged switch-on and switch-off curves fitted by an exponential.

The switching rates are then determined as:

$$\frac{1}{\tau_{on}} = \frac{1}{\tau_{on,405}} \quad \frac{1}{\tau_{off}} = \frac{1}{\tau_{off,365} + \tau_{off,405}} \quad (4.5)$$

And the individual on- and off-times can be extracted as follows [57]:

$$\tau_{on,405} = \tau_{on} = 104 \text{ ms} \quad \tau_{off,365} = \frac{\tau_{on}\tau_{off}}{\tau_{on} - \tau_{off}} = 160 \text{ ms} \quad (4.6)$$

$$\tau_{off,405} = \tau_{on,405} (1/\rho_{on,405} - 1) = 10 \text{ s} \quad \tau_{on,365} = \tau_{off,365} \frac{\rho_{on,365}}{1 - \rho_{on,365}} = 383 \text{ ms}. \quad (4.7)$$

It follows that applying 405nm combined with 532nm illumination allows to switch Dreiklang at a low on-ratio of 1%, which was optimal for SOFI. The switching speed can be tuned by adjusting the intensity of 405nm source, with single frame exposure time being about the molecular on-time. Faster exposure times are favorable for avoiding motion artifacts during live cell imaging. However, molecules usually emit less photons per switching cycle at faster

switching rates. The 15 W/cm^2 intensity of 405nm illumination provided a good balance between these two parameters.

4.3 Fixed cell 3D fluorescence imaging

As a first 3D SOFI proof of principle we acquired 5000 images of antibody stained microtubuli in a fixed Hela cell. Under continuous excitation with 635nm laser and reactivation with 405 nm laser, Alexa 647 showed reversible photoswitching. Figure 4.7 shows the color-coded maximum intensity projections of the wide-field and second order SOFI images. For visualizing 3D data, we show maximum intensity projection of the stack, color-coded in depth with isolum strict colormap, compatible with red-green color perception deficiencies [68].

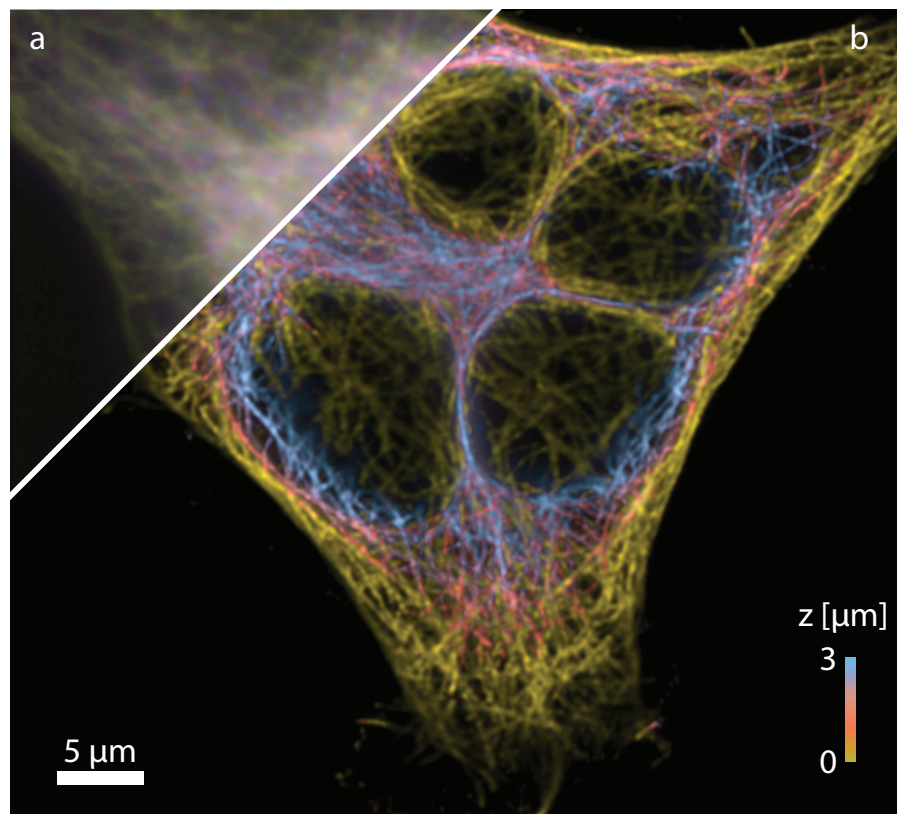


Figure 4.7: Alexa 647 stained microtubuli in a fixed Hela cell. (a) Wide field image. (b) Second order 3D SOFI reconstruction.

Microglial cells represent about 10% of brain cells and act as the primary immune defense of the nervous system [69]. Recent studies by Bolmont et al [70, 71] showed that microglia react to the formation of amyloid plaques, indicating their role in the progression of Alzheimer's disease. We used 3D SOFI approach to image the antibody stained microglial cell membrane (Alexa 647) surrounding the extracellular amyloid plaque in a thin slice of transgenic mouse

Chapter 4. SOFI imaging

(Alzheimer's disease) brain tissue.

Using the setup for simultaneous 3D acquisition, we acquired 5000 frames containing blinking fluorophores at 30ms exposure time. Images of microglial cell membranes were generated (figure 4.8) with the third order balanced SOFI algorithm described in section 2.4.6. Calculating 3D cross-cumulants, 22 sampling planes were obtained from the original eight image planes, allowing therefore a finer depth sampling.

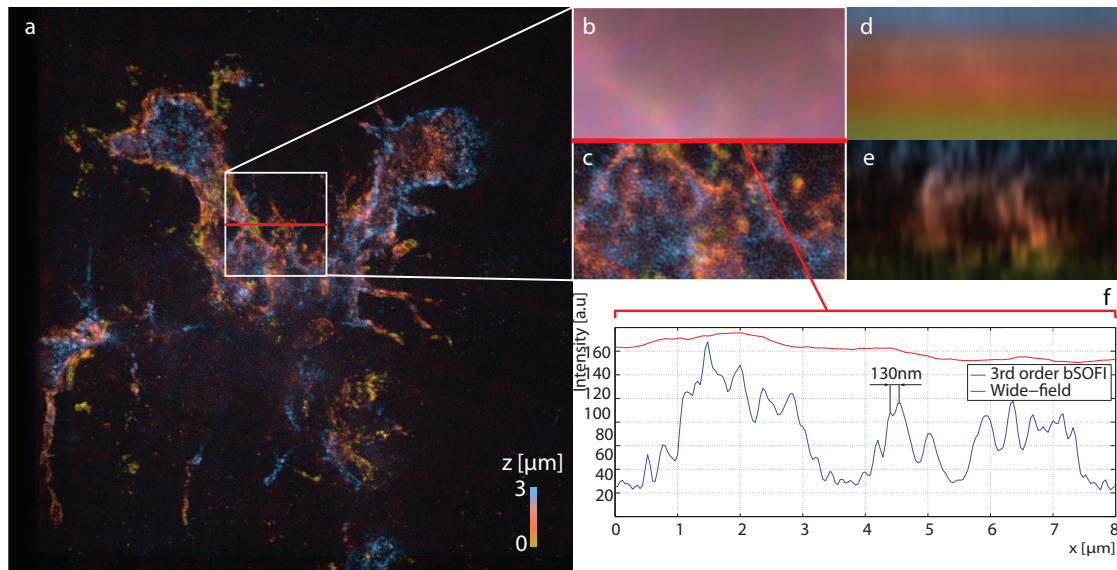


Figure 4.8: (a) Microglial cell membrane surrounding an amyloid plaque, third order SOFI. (b) Zoomed region, wide-field image (c) Zoomed region, third order SOFI. (d) X-Z projection of the cut indicated by red line, wide-field. (e) same projection, third order SOFI. (f) x-profile of the same cut, wide-field v.s. SOFI.

Structural details barely visible in the classical widefield image are resolved and the strong out-of-focus background is significantly reduced. Details as small as 130nm (lateral) are resolved, close to the expected three fold resolution improvement.

4.4 Live cell and bacteria 2D fluorescence imaging

FtsZ and MreB proteins are the major parts of the bacterial cytoskeleton [72]. FtsZ (Filamenting temperature-sensitive mutant Z) is a ring structure and a homologue to tubulin in eukaryotic cells. It plays an important role in the cell division of different bacterial species [73, 74]. MreB is a protein homologous to actin in eukaryotic cells. It was shown, that MreB controls the thickness of bacteria and plays an important role in bacterial membrane synthesis [75].

4.4. Live cell and bacteria 2D fluorescence imaging

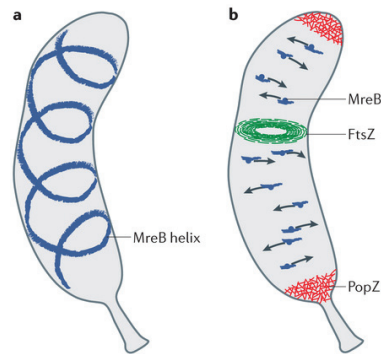


Figure 4.9: Model for MreB and FtsZ organization in *C. crescentus*. Adapted from Nature Reviews Microbiology 12, 9–22(2014), figure 2.

Mycobacterium Smegmatis (*M. Smegmatis*) serves as model organism since it shares the ring structure similar to *M. Tuberculosis* while being non-patogenic. In order to see the FtsZ ring in *M. Smegmatis*, we used a mutant stably expressing FtsZ-Dreiklang. Since the environment conditions in bacteria are different compared to the mammalian cells, we adapted the illumination intensity to optimize Dreiklang photoswitching.

Under 45 W/cm^2 532nm illumination intensity Dreiklang showed fast off-switching. We used 365nm LED to back-switch to the on-state. As the UV illumination caused strong autofluorescence, we kept its intensity at a low level of about 0.5 W/cm^2 . We used sequences of 2000 frames acquired with a 2D SOFI setup (figure 3.1) at 30ms exposure time in order to reconstruct third order super-resolved images (figure 4.10).

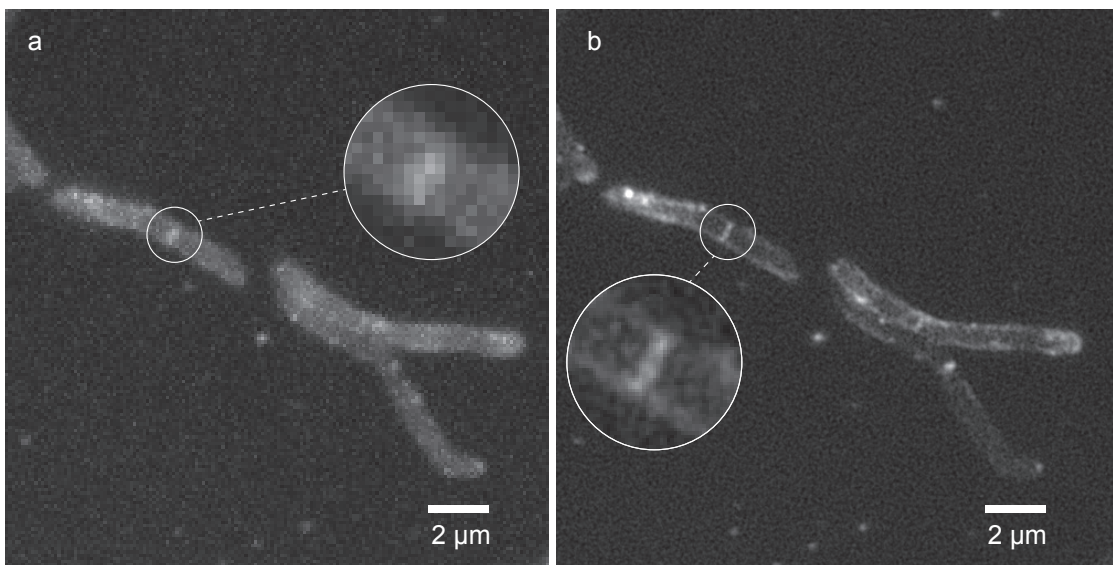


Figure 4.10: FtsZ structure in *M. Smegmatis*. (a) Wide field image. (b) SOFI third order.

Chapter 4. SOFI imaging

Compared to the wide-field image, SOFI allows to better distinguish the FtsZ ring and suppress the background from the bacterial membrane.

For observation of MreB structure, we used E. Coli stably expressing MreB-rsEGFP. We used a 488nm laser source at 2 W/cm^2 intensity and a 405nm laser at a low intensity of 0.05 W/cm^2 to induce the reversible photoswitching of rsEGFP. Second order SOFI allows to resolve details of MreB skeleton, which are not visible in a conventional image (figure 4.11).

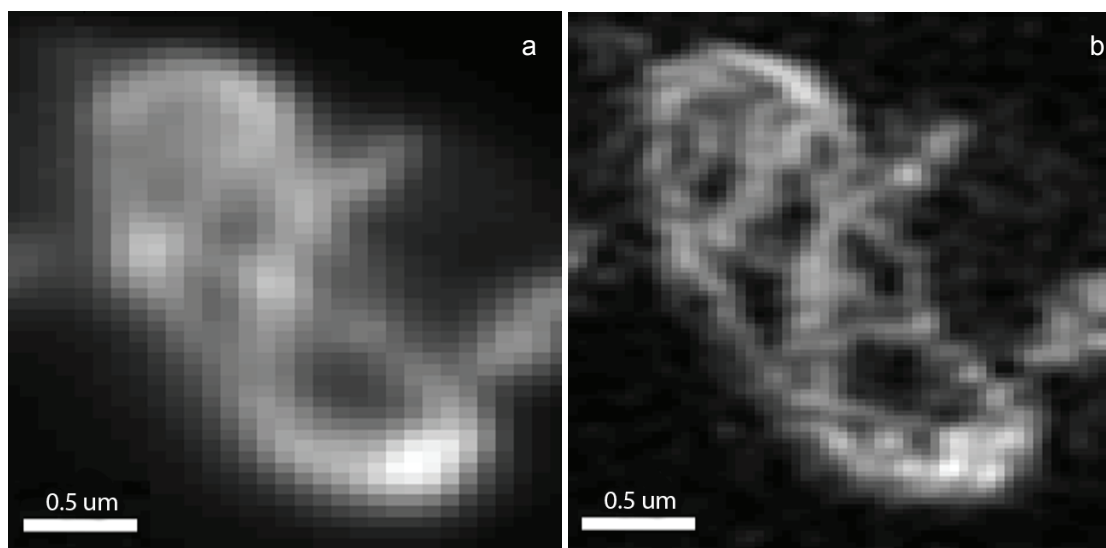


Figure 4.11: Images of MreB structure of E Coli. (a) Wide-field image. (b) 2nd order SOFI image.

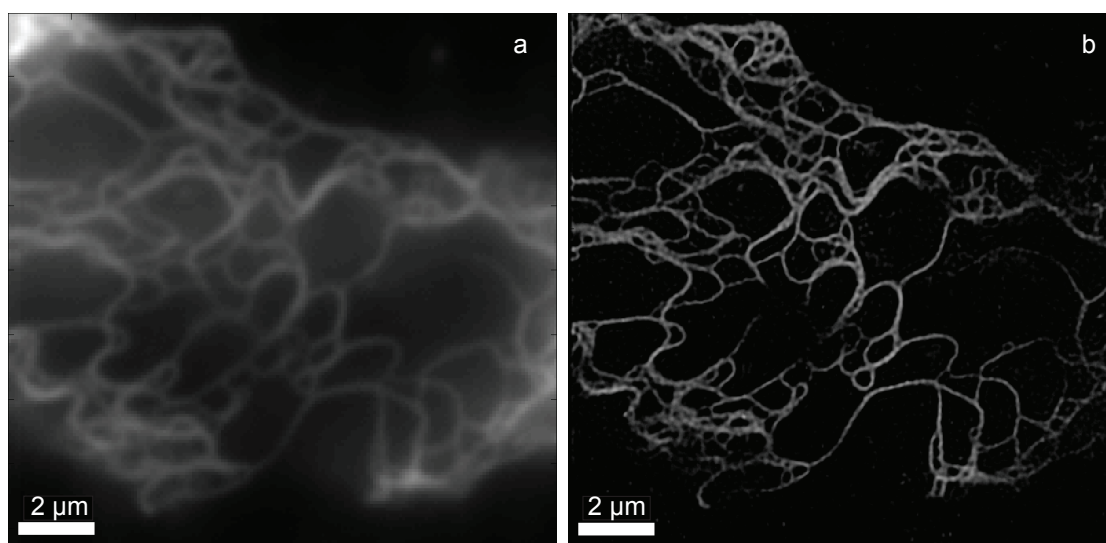


Figure 4.12: Images of Dreiklang expressing keratin structure in live HeLa cell. (a) Wide-field image. (b) 3rd order SOFI image.

4.4. Live cell and bacteria 2D fluorescence imaging

For the first experiment with live cells, we chose HeLa cells expressing Keratin-Dreiklang. We acquired 5000 images at 20 ms exposure time at 450 W/cm^2 and 15 W/cm^2 532nm and 405nm laser intensities accordingly. Figure 4.12 shows comparison of wide-field and SOFI reconstructed image. Third order SOFI analysis allows to suppress the background and distinguish between the close-situated keratin fibers.

4.5 Journal article preview/manuscript

Live cell three-dimensional time-lapse super-resolution imaging

Azat Sharipov^{1*}, Tomas Lukes¹, Patrick A. Sandoz², Amir Nahas¹, Marcel Leutenegger^{1,3}, Stefan Geissbuehler¹, Daniel Szlag¹, Gisou van der Goot², Theo Lasser¹

¹ École Polytechnique Fédérale de Lausanne, Laboratoire d'Optique Biomédicale, 1015 Lausanne, Switzerland

² École Polytechnique Fédérale de Lausanne, Global Health Institute, 1015 Lausanne, Switzerland.

³ Department of NanoBiophotonics, Max Planck Institute of Biophysical Chemistry, Am Fassberg 11, 37077 Göttingen, Germany.

* azat.sharipov@epfl.ch

Three-dimensional (3D) imaging in conventional wide-field super-resolution microscopy techniques is typically done by sequential imaging of several depth planes, which is suboptimal for imaging dynamic objects. We introduce a robust image-splitting prism designed as an add-on for conventional wide-field microscopes to acquire several depth planes of a sample volume simultaneously. The prism greatly simplifies the multi-plane acquisition and improves the opto-mechanical stability of the microscope. Applied for 3D super-resolution optical fluctuation imaging (SOFI), the depth sampling was increased and background and out-of-focus contributions were minimized. Using a Bregman iterative method for deconvolution and noise suppression, we obtained single 3D super-resolved images from short image sequences with as few as 100 frames, resulting in an acquisition time of two seconds per super-resolved 3D image. We show super-resolved 3D movies of living Hela cells expressing the fluorescent protein Dreiklang.

4.5.1 Introduction

Super-resolution fluorescence microscopy is a widely emerging field recognized by the Nobel Prize in chemistry in 2014. The acquisition of super-resolved images in three dimensions (3D) by means of light-sheet microscopy [23] or super-resolution optical reconstruction microscopy [76] have been demonstrated recently. However improvement in axial and lateral dimensions combined with the speed compatible with imaging the processes in live cells remains a challenge.

Single molecule localization microscopy (SMLM) achieved 3D imaging with several techniques, for instance by introducing astigmatism in the imaging path [77] or by interferometric detection [78, 79]. Although SMLM achieves high localization precision (20nm in lateral and 20–60nm in axial directions), the imaging depth is limited to about a wavelength or less and the acquisition usually lasts for minutes. Faster acquisition was demonstrated by trading off

spatial resolution.

Super-resolution optical fluctuation imaging (SOFI) [13] provides a unique approach to diffraction-unlimited imaging in 3D because SOFI accepts a wider range of photoswitching conditions than SMLM [37] by analyzing the spatio-temporal fluctuations of light from the sample to boost the image resolution. If the point spread function (PSF) spans several pixels, spatio-temporal cross-correlations of intensity fluctuations among neighboring pixels can be calculated in order to increase the image resolution in 3D. SOFI assumes that the fluorophores in the sample blink stochastically and independently.

Super-resolved 3D imaging with SOFI was first demonstrated by sequential acquisition of depth planes [62]. Recently, Geissbuehler et al. [57] proposed a multi-plane imaging concept that supports higher acquisition speed and reduces photobleaching. To image several depth planes simultaneously, 50:50 beam splitters were used together with a set of mirrors. This design allowed tuning the distances between the imaged depth planes but required frequent time-consuming alignment. Long term live cell imaging also demands improved mechanical stability. We address these issues by providing eight image planes with a dedicated single solid prism that we designed for 3D microscopy. The sensitivity of the system against environmental changes is greatly reduced. Focusing on fast acquisition while maintaining image quality, we further propose a novel deconvolution algorithm well suited for SOFI microscopy.

4.5.2 Experimental setup

Figure 4.13 outlines our multi-plane epi-fluorescence microscope. A high numerical aperture objective is selected so that the immersion liquid matches the refraction index of the sample to avoid spherical aberrations. The tube lens TL creates an intermediate image, where a rectangular window is used to limit the field of view. An additional telescope comprising lenses T_1 and T_2 is used to project the images at the camera sensors.

The images are separated in depth using a 2×4 image splitting prism, assembled of two plane parallel and a rhomboid prism with sides cut at 45 degrees. A coating for broadband 50:50 image splitting is used at the central cemented interface. The larger plane parallel, smaller plane parallel and rhomboid prisms have thicknesses of $h + 2\varepsilon$, h , and $h - 2\varepsilon$, where $\varepsilon = \sqrt{2}d$ sets up a lateral distance d between the neighboring images on the camera sensors. The optical path difference (OPD) in the image space corresponds to $\delta z = d/n$, where n is the refraction index of the prism glass. This distance corresponds to a displacement $\delta z/M_t^2$ in the object space, where M_t is the lateral magnification of the microscope.

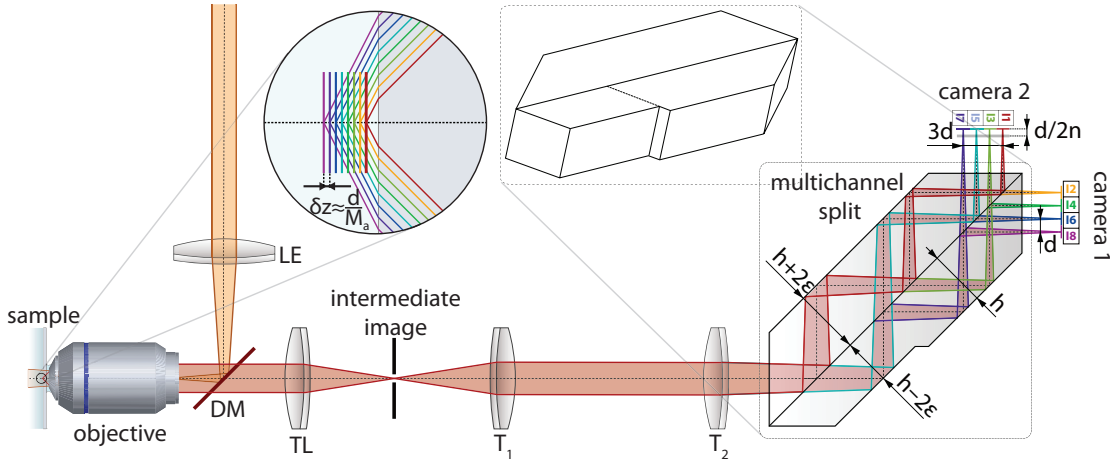


Figure 4.13: Detection path of the multi-plane epi-fluorescence microscope

We mounted the cameras at axial distances differing by $d/2n$ to set up an interleaved channel configuration and an OPD of $\delta z = d/2n$ between adjacent depth planes. The cameras could be placed at $4d/n$ distance to obtain a sequential channel configuration and double the OPD to $\delta z = d/n$.

The prism was designed for the use with a $13.3 \times 13.3\text{mm}^2$ CMOS sensor. Thus, it implements a lateral distance d of 3.3mm allowing to acquire an image field of 3.2mm width. The OPD is therefore $\delta z = d/n \approx 2.1\text{mm}$, which sets up an image defocus of about 1% of the focal length of lens L_2 ($f_2 = 200\text{mm}$). When stepping through the object planes, the marginal field points in the images shift by a few percent of the PSF diameter only, ideally allowing analysis of the images by a 1:1 correspondence of the pixels in the image frames of adjacent object planes.

We also incorporated a custom-built incubation system, allowing to control the temperature and CO_2 level. The motorized stage and objective lens were placed inside the incubated chamber to avoid the temperature drifts.

4.5.3 Image reconstruction

SOFI achieves super-resolution by calculating spatio-temporal cumulants on a sufficiently long image sequence [13, 12]. In its basic form, the application of n^{th} order SOFI analysis achieves up to $\sqrt{n} \times$ resolution improvement. The resolution improvement can be boosted to $n \times$ by an additional deconvolution step. So far a classic Lucy-Richardson deconvolution was applied within the balanced SOFI algorithm [56]. However, the Lucy-Richardson deconvolution shows limitations in dealing with noise and it applies a non-negativity constraint for the image data. In contrast to classical imaging, the cumulant analysis in SOFI cannot warrant and often does not yield positive values which may lead to image artifacts upon deconvolution.

Figure 4.14 outlines the image analysis for time-lapse SOFI. During step 1, the multi-plane

microscope simultaneously acquires eight depth planes at each time point. At step 2, each subsequence (100 - 1000 frames) is used for calculating the 3D raw cumulant output image. The subsequences were chosen sufficiently long to satisfy image quality criteria [37]. To minimize photobleaching artifacts, the whole sequence of acquired camera frames can be divided into shorter subsequences (100 - 500 frames).

Step 3 involves the deconvolution of each raw cumulant image. Aiming for super-resolved 3D time lapse live cell imaging, we adapted the split Bregman iterative method [80] for deconvolution and incorporated it into the balanced SOFI algorithm. The Bregman iterative method has several advantages such as fast convergence rate, flexibility of parameters and prominent stability. It has been proven efficient for image restoration and deconvolution tasks [81]. The new SOFI post-processing based on the Bregman iterative method can handle the peculiarities of cumulant images, reduces the noise contribution and in consequence increases the signal to noise ratio (SNR). However, in the presence of noise, this inversion can become unstable and a regularization is necessary. The total variation (TV) based regularization introduced by Rudin et. al. [82] was then used for the final image reconstruction. For a more detailed description of the algorithm, please refer to the PhD thesis of Tomas Lukes [83].

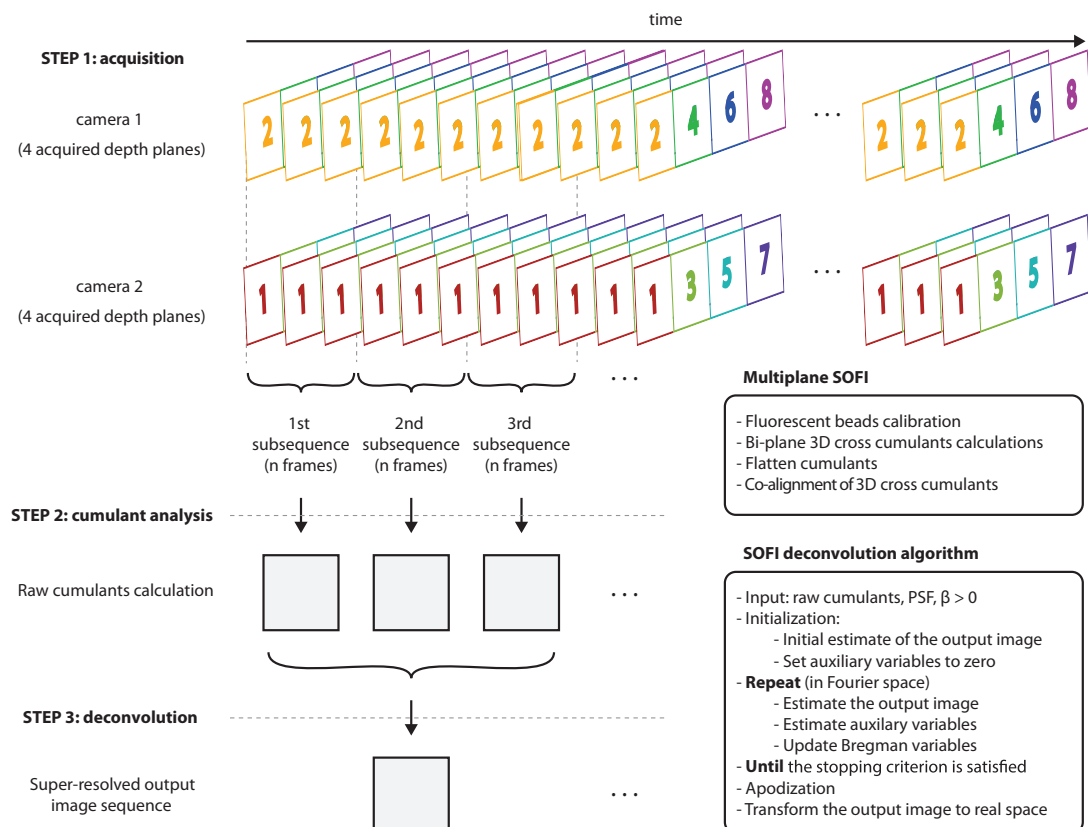


Figure 4.14: SOFI processing flowchart. The sequence of images is acquired synchronously by 2 cameras. The images are then divided into subsequences to limit artifacts due to photobleaching and sample motion.

4.5.4 Live cell imaging

To demonstrate the imaging capabilities of our approach, we acquired several measurements with live and fixed HeLa cells. The acquired raw image data was processed using the aforementioned 3D SOFI algorithm.

We imaged HeLa cells cultured in a Petri dish and further transfected with Lipofectamine-2000 reagent. The transfected cells expressed the reversibly photo-switchable fluorescent protein Dreiklang [52] in the vimentin (figure 4.17) and actin (figure 4.15) structures. Overexpression of actin and tubulin subunits are known to alter the cytoskeleton dynamics and the cell fate, in particular cell division [84]. In order to overcome this issue, Dreiklang was coupled to the actin binding peptide LifeAct [85].

Dreiklang's reversible on-off switching of fluorescence can be controlled by illumination at 365nm and 405nm wavelengths and is separated from the excitation maximum at 515nm wavelength. We illuminated Dreiklang by 532nm light to excite its fluorescence and applied 405nm light at low intensity to switch it on and off at a low on-ratio of about 1%. The lateral magnification was adjusted to $M_t = 58.3\times$ to set up a depth plane separation of around 450nm in an aqueous environment.

Figure 4.15 shows the first frame of 3D video sequence of living HeLa cells expressing Actin-Dreiklang. Due to the the lower Dreiklang expression level, we used 500 frames to generate a single super-resolved frame.

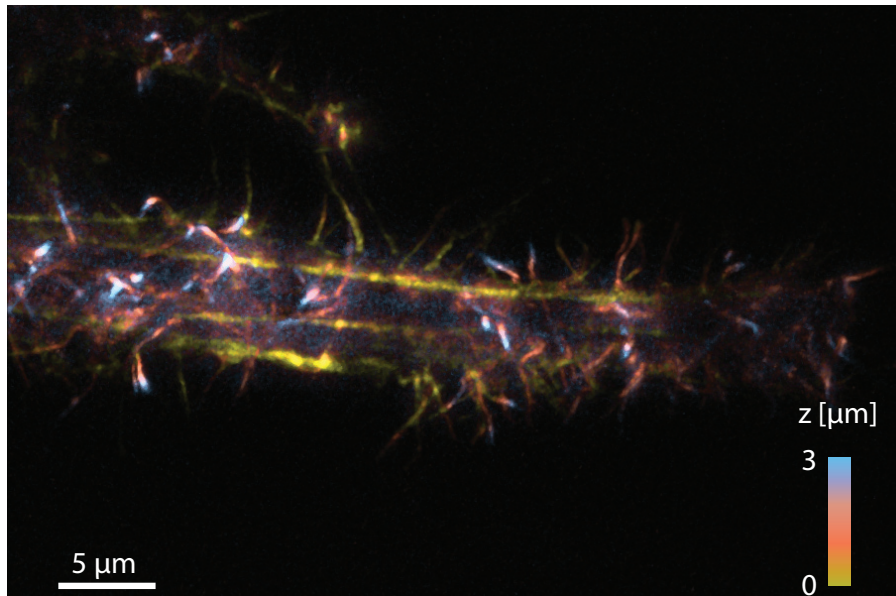


Figure 4.15: First frame of a super-resolved 3D video sequence of living HeLa cells expressing Actin-Dreiklang. Shown is the maximum intensity projection of a second order 3D SOFI image.

Two-dimensional super-resolved images have been demonstrated using Mitotracker with STORM [34] and SIM [86]. Here we demonstrate 3D SOFI time-lapse imaging of mitochondria in a living HeLa cell using Mitotracker Orange labeling. The staining of HeLa cells was performed in Leibovitz solution at 40 nM concentration. The cells were later washed three times with Leibovitz medium and then imaged immediately (figure 4.16). We used 400 frames acquired at 15ms frame exposure time for the SOFI reconstruction, limiting the overall exposure time to 6 seconds.

Figure 4.17 shows one frame of a super-resolved 3D video sequence of living HeLa cells expressing Vimentin-Dreiklang. For this experiment, we used a setup described in figure 3.2 with a number of planes reduced to four. Here we used only 100 frames for the 3D image reconstruction. Second order SOFI analysis allows (b) to improve resolution and reduced the background compared to the wide field image (a). Bregman deconvolution (c) also allows to suppress noise compared to the conventional Lucy-Richardson deconvolution.

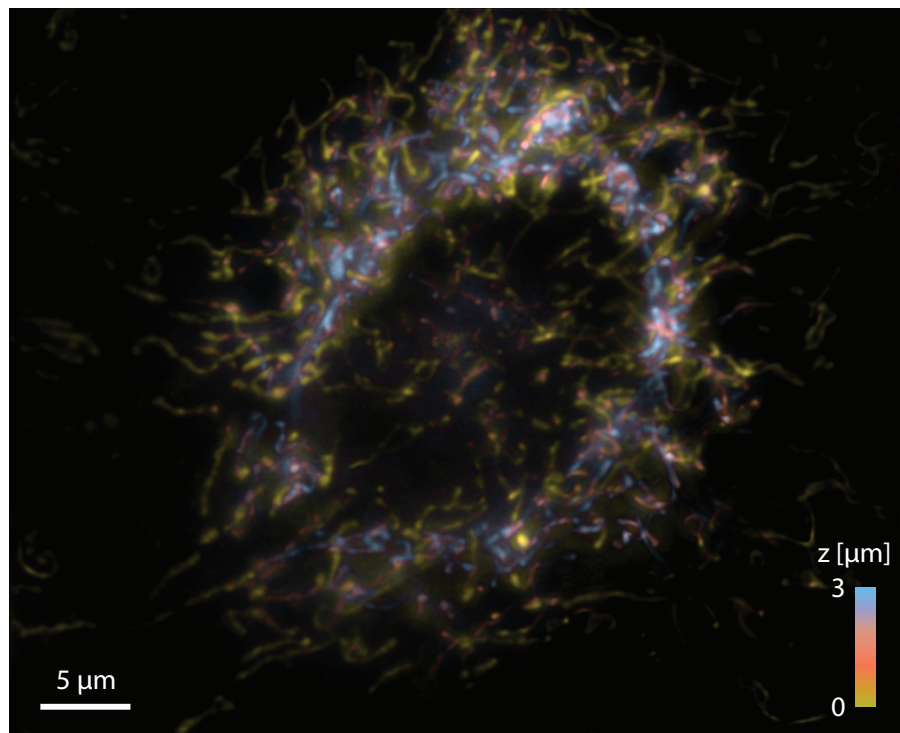


Figure 4.16: 3D SOFI 2nd order reconstruction of mitochondria structure in a live HeLa cell.

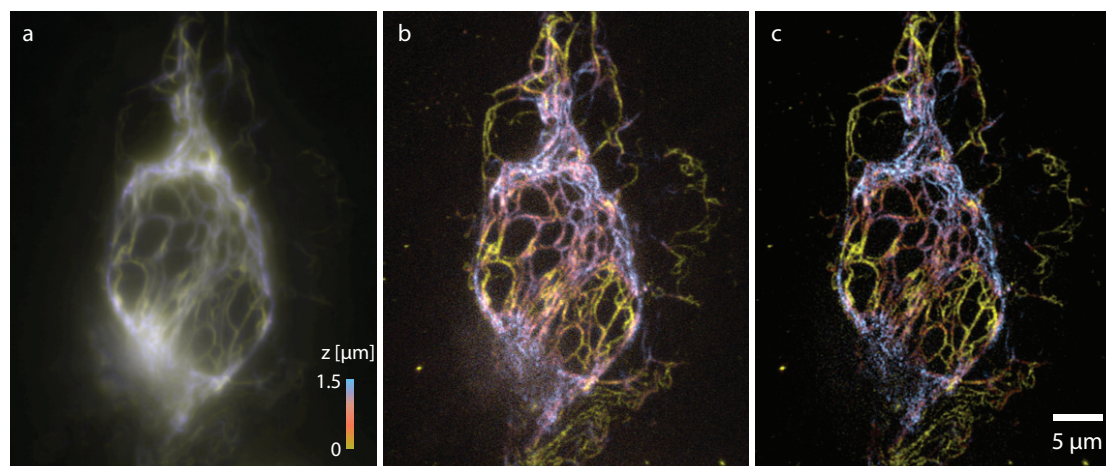


Figure 4.17: First frame of a super-resolved 3D video sequence of living HeLa cells expressing Vimentin-Dreiklang. Maximum intensity projections of the 3D (a) widefield image, (b) second order SOFI image, (c) improved balanced SOFI image. The depth information is color-coded. Only 100 images were used for the SOFI reconstructions. The image acquisition for one super-resolved 3D image took two seconds.

4.5.5 Discussion

We introduced a new 3D microscope designed to acquire several depth planes simultaneously. The setup allows some flexibility in tuning inter-plane distances by modifying the lateral magnification and by choosing an appropriate channel configuration. We characterized the microscope's optical performance and achieved diffraction-limited imaging. The microscope's capabilities enable the use of 3D SOFI reconstructions for long-term experiments. We developed and applied a novel deconvolution algorithm for linearizing the resolution improvement with the cumulant order in SOFI. Due to our new algorithm, fewer input images are required for the SOFI reconstruction. We demonstrated the performance of this algorithm and the 3D microscope by recording super-resolved time-lapse movies of actin and mitochondria network reconfigurations in living HeLa cells that were incubated in the sample chamber during the entire time-lapse acquisition.

4.5.6 Methods

Microscope setup

The cell imaging experiments were performed on a custom-built microscope comprising an incubator with temperature and CO_2 control. We used an Olympus UPLSAPO 60XW water-immersion objective with a numerical aperture of 1.2 and $60\times$ magnification. The following continuous-wave (cw) lasers were used for fluorescence switching and excitation: a 120 mW 405 nm laser (iBeam smart, Toptica), a 200 mW 488 nm laser (iBeam smart, Toptica), and

an 800 mW 532 nm DPSS laser (MLL-FN-532, Roithner Lasertechnik). All laser beams were combined with a set of dichroic mirrors and focused in the back focal plane of the objective to create an approximately homogeneous epi-illumination in the imaged field of view. The image-splitting prism was custom-manufactured at Schott Suisse Sa facility.

Cell preparation

Hela cells were incubated at 37°C at 5% CO₂ in a Minimum Essential Medium (MEM) Eagle completed with Earle's salts, L-glutamine, sodium bicarbonate complemented with 10% fetal bovine serum, 1× penicillin-streptomycin, 1× GlutaMAX, 1× MEM Non-Essential Amino Acids Solution. The cells were plated in 35mm glass bottom FluoroDishes (World Precision Instruments Inc.).

Dreiklang-LifeAct construction and cell transfection

Dreiklang-LifeAct was constructed as follows: The Dreiklang sequence (Aberrior) was amplified by PCR and inserted in a pCDNA3 using PmeI and AgeI restriction sites. The LifeAct sequence was synthesized (Microsynth) according to [85], annealed and inserted in front of Dreiklang using KpnI and BstBI restriction sites. The transfection was done with Fugene (Promega) or Lipofectamine-2000 (Invitrogen) for 24 hours before imaging.

Funding Information

This work was supported by Swiss National Science Foundation (SNSF) under grant 200020_159945/1. T.L. acknowledges a SCIEX scholarship (project code 13.183).

5 Conclusions and outlook

During my thesis, I adapted super-resolution optical fluctuation imaging (SOFI) for the use with the new multi-plane epi-fluorescence microscope for 3D live-cell super-resolution imaging. The microscope performance was described and experimentally verified. 3D SOFI was demonstrated on the examples of fixed and living cells.

As established in chapter 2, the key advantage of SOFI compared to the localization techniques is its high tolerance of fluorophore blinking conditions and low SNR. We have shown further intrinsic properties of SOFI, such as finer pixel grid generation and background reduction. The cross-cumulants concept allows to extend the existing algorithm for swift 3D imaging. The principle of 'virtual' plane generation was explained as well as the concomitant resolution improvement in all three spatial dimensions.

Thanks to our new image-splitting prism, made as a single optical element, we achieved robust in-depth plane separation and could simplify the alignment procedure decisively as compared to the previous multi-plane epi-fluorescence microscope. We tuned the depth sampling by changing the microscope's magnification and showed by ray-tracing and experiments that the new multi-plane microscope achieved diffraction-limited performance. The microscope was fully characterized experimentally and the calibration results were used for the SOFI analysis of multi-plane image sequences.

Aiming at live cell imaging, we investigated the switching properties of fluorescent proteins. Dreiklang proved to be a versatile fluorescent protein, allowing to tune the blinking properties due to three distinct absorption wavelengths for fluorescence excitation and switching on and off. We have taken 3D super-resolved images of a Microglial cell in a brain slice, showing almost three-fold resolution improvement and significant background reduction. 2D images of live bacteria and cells demonstrated the compatibility of SOFI with different types of live cell imaging. Moreover, we demonstrated the capability of 3D time-lapse SOFI by recording SOFI movies of vimentin, actin and mitochondria in live HeLa cells.

Transport of intensity equation (TIE) is a versatile phase reconstruction method, based on the

Chapter 5. Conclusions and outlook

variation of intensity along the optical axis [87, 88]. The TIE can be derived from the paraxial wave equation:

$$(\nabla_{\perp}^2 + 2ik \frac{\partial}{\partial z})U_A(\vec{x}, z) = 0, \quad (5.1)$$

where k is the wave number, \vec{x} and z are lateral and axial coordinates accordingly, ∇_{\perp}^2 is the transverse Laplacian operator, and U_A is the complex amplitude of U . TIE then links the phase of the field to its intensity axial derivative under the assumption of uniform illumination $I_0(\vec{x}) = J_0$:

$$-\frac{k}{J_0} \frac{\partial}{\partial z} I(\vec{x}, z)|_{z=0} = \nabla_{\perp}^2 \phi_0(\vec{x}), \quad (5.2)$$

Where I is the image intensity, and ϕ is the phase. The intensity axial derivative can be approximated as the difference between the defocused planes [89], assuming that the defocus distance is small. Typically, several depth planes are acquired by doing a z -scan, as indicated in figure 5.1.

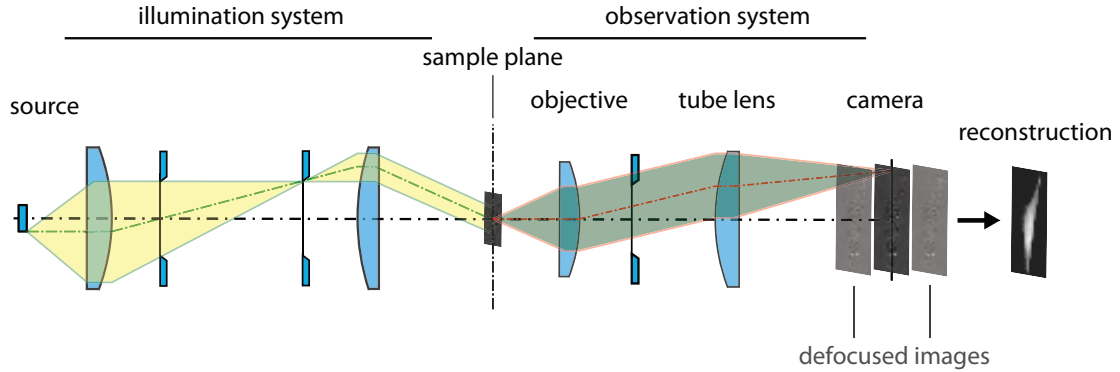


Figure 5.1: Standard acquisition scheme for TIE. A transparent object is illuminated in transmission mode. The image of an object and is projected on a camera. Moving the camera along the optical axis allows to acquire the defocused object images.

In order to take advantage of TIE phase reconstruction, we added a Koehler trans-illumination to the multi-plane microscope. This allows to acquire several defocused images of an object simultaneously. By applying the TIE phase reconstruction algorithm, the phase of the transmitted light can be recovered quantitatively [88]. In a proof-of-principle experiment, we acquired an 8-plane image of fixed non-stained Hela cells and used planes 1, 4 and 7 for the reconstruction of the phase image (figure 5.2).

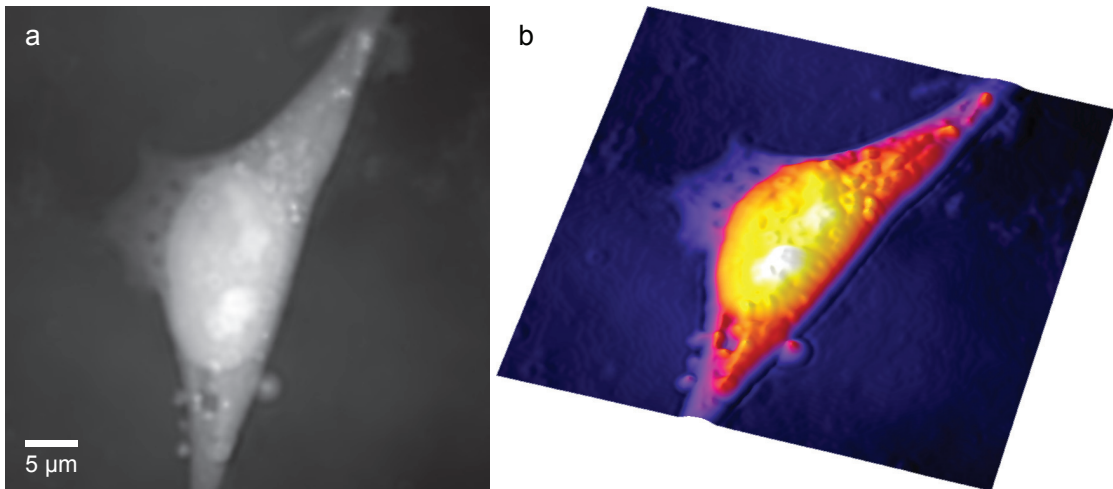


Figure 5.2: (a) TIE reconstructed image of the fixed HeLa cell. (b) 3D surface plot of the same image, Morganstemnig colormap.

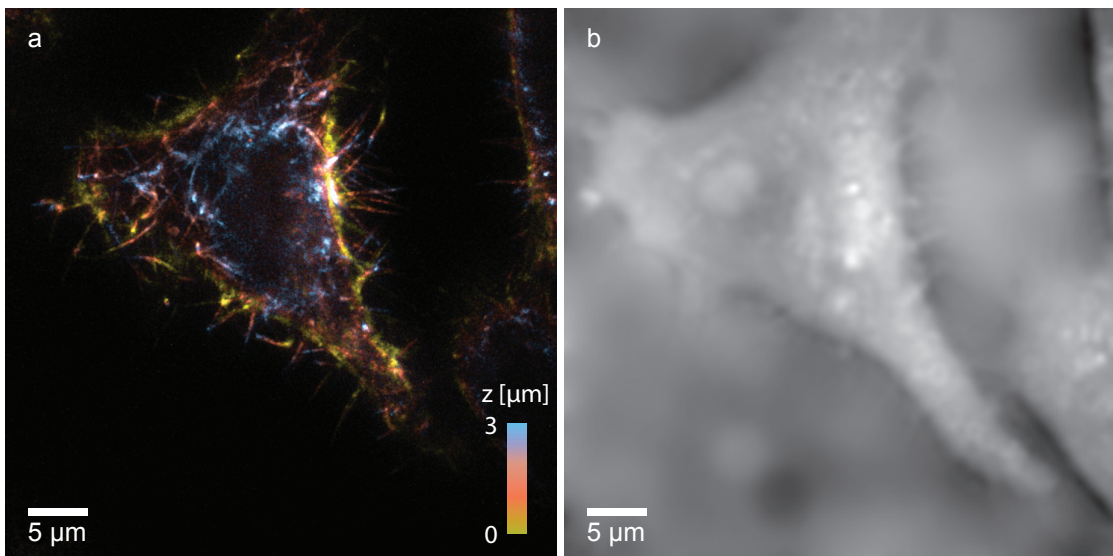


Figure 5.3: (a) First frame of a super-resolved 3D video sequence of live HeLa cells expressing Dreiklang Lifeact. (b) TIE reconstructed image. 600 frames were used for SOFI reconstruction, and one single frame for the TIE reconstruction, taken directly after the fluorescence frame. 5 super-resolved and 5 phase images were acquired.

In order to demonstrate the potential of 3D multi-plane microscope, we performed a time-lapse experiment on HeLa cells, expressing actin-Dreiklang. The first SOFI and TIE images are shown in the figure 5.3.

Since the speed of TIE imaging is in principle limited only by camera exposure time, the frame rate can reach 300 Hz when using Hamamatsu ORCA Flash-4.0 camera. The complementarity

Chapter 5. Conclusions and outlook

of SOFI and TIE can therefore provide both high spatial resolution for a structure of interest and temporal resolution for the phase image. One of potential applications can be the tracking of signal transfer between neurons. So far we have demonstrated the 2D application of TIE. However, it holds a potential for the 3D phase reconstruction [90].

Odermatt et. al. have demonstrated the complementarity of Atomic force microscopy (AFM) and single molecule localization microscopy (SMLM) when imaging living cells [91, 74]. While AFM provides high-resolution topological images of cell surfaces, SMLM gives a better insight of the internal cell structures. SOFI's tolerance of a wide range of blinking conditions can further contribute to the markers choice and subsequent long-term imaging when using the combination of AFM and super-resolution fluorescence techniques.

In summary, my thesis introduced a super-resolution technique capable of imaging the fluorescent samples in 3D. The technique bears a potential for life science applications and for combinations with label-free techniques.

Image gallery

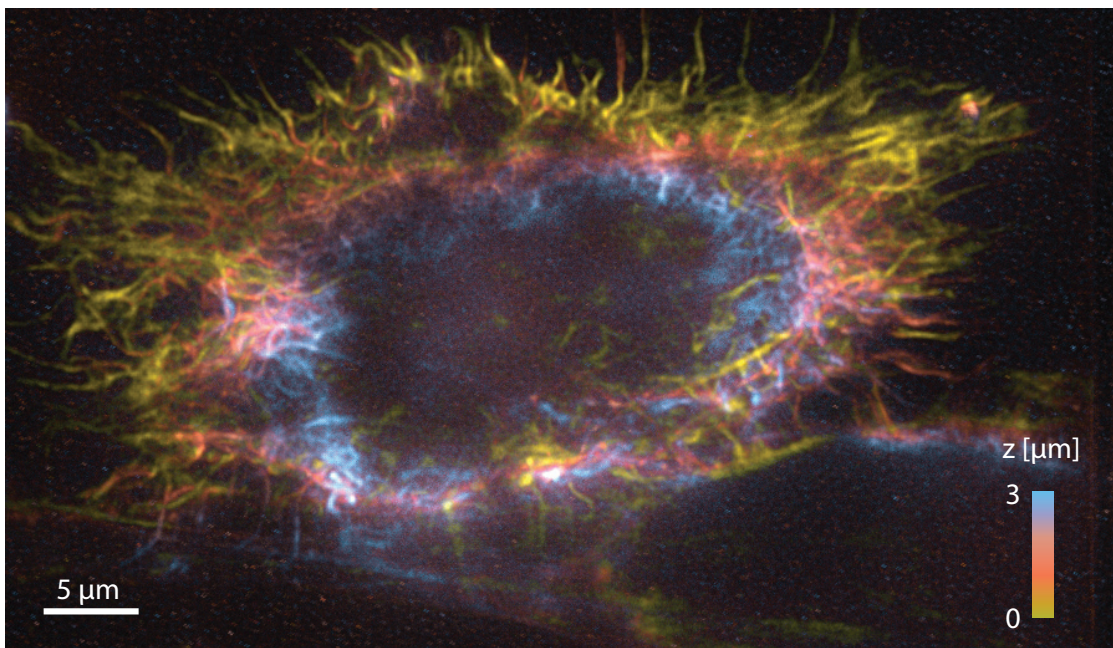


Figure 5.4: Actin structure expressing Dreiklang in a live HeLa cell. Second order SOFI reconstruction. Cooperation with Patrick Sandoz and Prof. F. Gisou van der Goot.

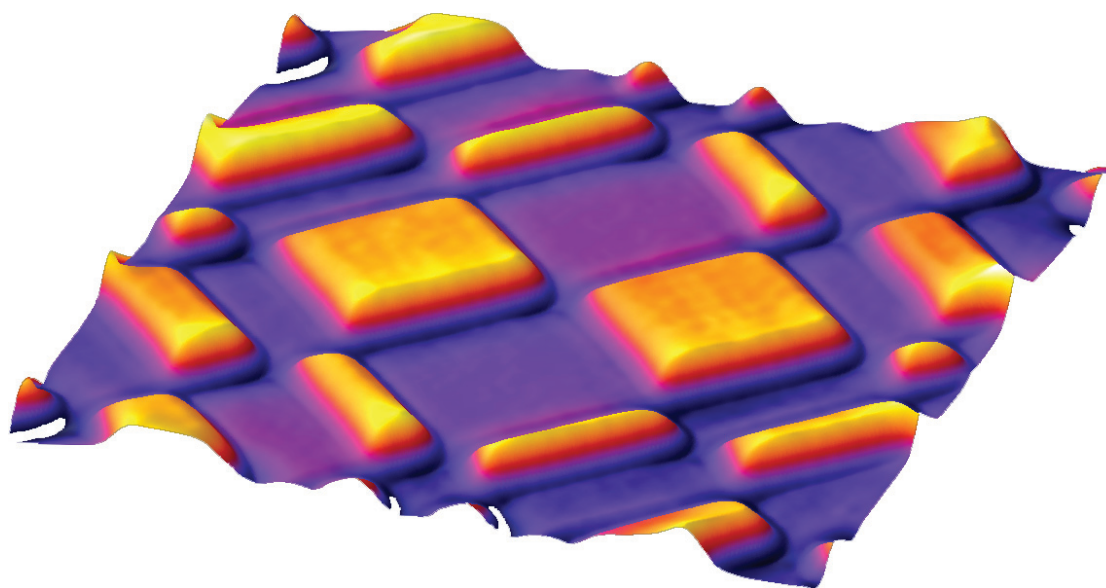


Figure 5.5: Surface plot of the TIE reconstruction of test sample, containing stepped checkerboard structure. Isolum colormap [68].

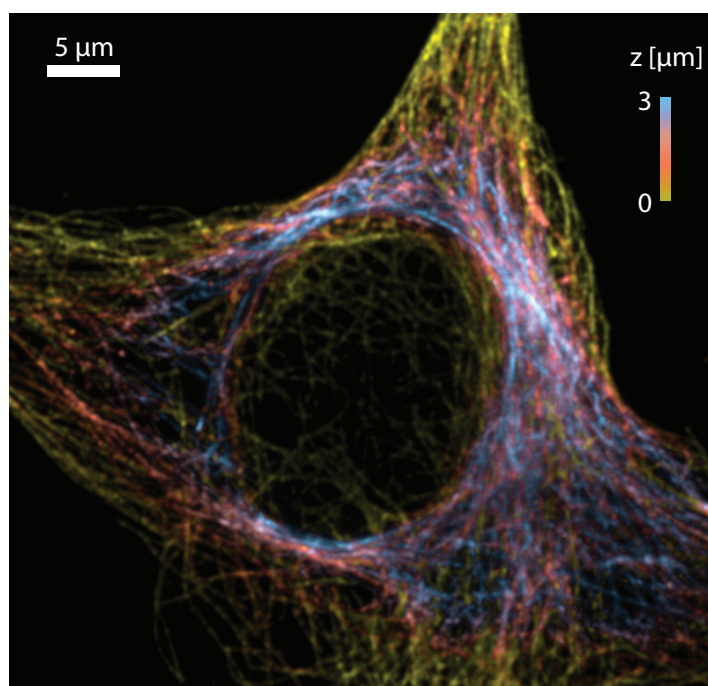


Figure 5.6: Tubulin structure in a fixed HeLa cell. Antibody staining with Alexa 647. Second order SOFI reconstruction.

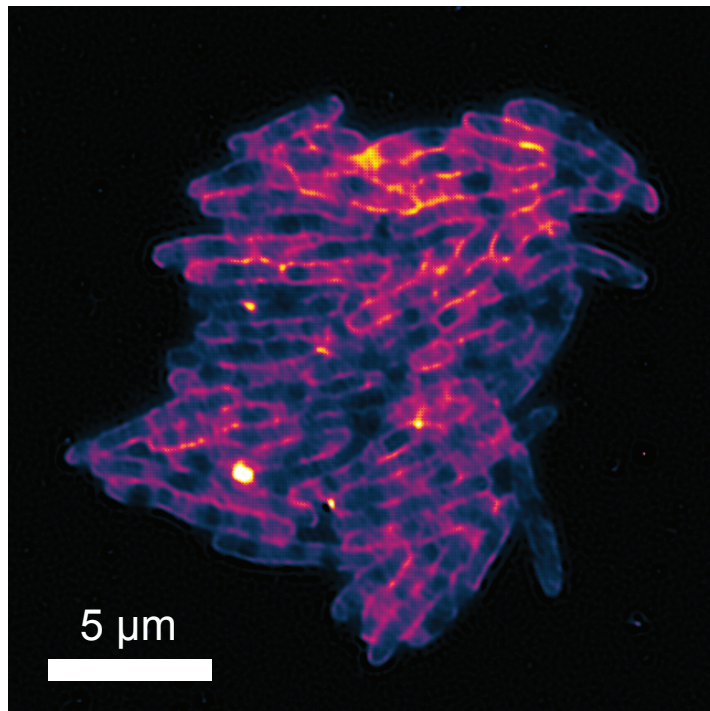


Figure 5.7: Third order SOFI image of bacteria *M. Smegmatis*, expressing Dreiklang in cell membrane. Morgenstemnig colormap [68]. Cooperation with Raphael Sommer and Prof. Stewart Cole.

A Image splitting prism characterization and setup alignment

A.1 ABCD calculation conventions

ABCD matrix analysis or ray transfer matrix analysis provides a simple way to describe a paraxial optical system. The technique is based on tracing rays in a meridional plane between transverse input and output planes. A ray is defined by a 2×1 vector, defining its distance from and optical angle with the optical axis. Each optical element can then be described by a 2×2 matrix whose product with a ray vector yields the corresponding output ray parameters. A combination of optical elements can then be described by consecutive matrix products. Here we define the fundamental matrices used for the calculations.

The refraction by a thin lens with focal length f is described by

$$\begin{bmatrix} 1 & 0 \\ -1/f & 1 \end{bmatrix}. \quad (\text{A.1})$$

The propagation over the distance d in a medium of refractive index n is described by

$$\begin{bmatrix} 1 & d/n \\ 0 & 1 \end{bmatrix}. \quad (\text{A.2})$$

A.2 Jones Matrix description of the beam splitter

In the first (strong) approximation the entrance and exits as well as all reflections occur at a perfect right angle inside the prism. We can easily calculate the difference phase shift between s and p polarization using the Jones matrix formalism.

The matrix $\mathbb{B}\mathbb{S}_r$ and $\mathbb{B}\mathbb{S}_t$ respectively of a reflection and a transmission by a perfect 50/50

Appendix A. Image splitting prism characterization and setup alignment

beam splitter can be written as:

$$\mathbb{B}S_r = \frac{1}{\sqrt{2}} \begin{bmatrix} -1 & 0 \\ 0 & 1 \end{bmatrix} \quad \mathbb{B}S_t = \frac{1}{\sqrt{2}} \begin{bmatrix} 1 & 0 \\ 0 & 1 \end{bmatrix} \quad (\text{A.3})$$

A.2.1 Jones Matrix total internal reflection

The phase shifts in total internal reflection (θ_p, θ_s) p and s polarized light are given for an incidence angle of θ by:

$$\tan\left(\frac{\theta_p}{2}\right) = \frac{n\sqrt{n^2 \sin^2(\theta) - 1}}{\cos(\theta)} \quad \tan\left(\frac{\theta_s}{2}\right) = \frac{\sqrt{n^2 \sin^2(\theta) - 1}}{n \cos(\theta)} \quad (\text{A.4})$$

And so for $\theta = \pi/4$ and $n = 1.5$:

$$\theta_p = 0.644 \quad \theta_s = 0.322 \quad (\text{A.5})$$

Because only the phase shift between both polarizations is important, the corresponding Jones Matrix can be written as:

$$\text{TR} = \begin{bmatrix} e^{0.644i} & 0 \\ 0 & e^{0.322i} \end{bmatrix} \equiv \begin{bmatrix} 1 & 0 \\ 0 & e^{0.322i} \end{bmatrix} \quad (\text{A.6})$$

The polarization state for each image can then be written as:

$$M_{\text{Jones},1} = \text{TR} \cdot \text{TR} \cdot \mathbb{B}S_r \cdot \mathbb{B}S_r \cdot \mathbb{B}S_t = \begin{bmatrix} 1 & 0 \\ 0 & e^{0.644i} \end{bmatrix} \quad (\text{A.7})$$

$$M_{\text{Jones},2} = \text{TR} \cdot \text{TR} \cdot \mathbb{B}S_r \cdot \mathbb{B}S_r \cdot \mathbb{B}S_t = \begin{bmatrix} 1 & 0 \\ 0 & e^{0.644i} \end{bmatrix} \quad (\text{A.8})$$

$$M_{\text{Jones},3} = \text{TR} \cdot \text{TR} \cdot \mathbb{B}S_t \cdot \mathbb{B}S_t \cdot \mathbb{B}S_t = \begin{bmatrix} 1 & 0 \\ 0 & e^{0.644i} \end{bmatrix} \quad (\text{A.9})$$

$$M_{\text{Jones},4} = \text{TR} \cdot \text{TR} \cdot \mathbb{B}S_r \cdot \mathbb{B}S_r \cdot \mathbb{B}S_t = \begin{bmatrix} 1 & 0 \\ 0 & e^{0.644i} \end{bmatrix} \quad (\text{A.10})$$

$$M_{\text{Jones},5} = \text{TR} \cdot \text{TR} \cdot \mathbb{B}S_t \cdot \mathbb{B}S_t \cdot \mathbb{B}S_r = \begin{bmatrix} -1 & 0 \\ 0 & e^{0.644i} \end{bmatrix} \quad (\text{A.11})$$

$$M_{\text{Jones},6} = \text{TR} \cdot \text{TR} \cdot \mathbb{B}S_t \cdot \mathbb{B}S_t \cdot \mathbb{B}S_r = \begin{bmatrix} -1 & 0 \\ 0 & e^{0.644i} \end{bmatrix} \quad (\text{A.12})$$

$$M_{\text{Jones},7} = \text{TR} \cdot \text{TR} \cdot \mathbb{B}S_t \cdot \mathbb{B}S_t \cdot \mathbb{B}S_r = \begin{bmatrix} -1 & 0 \\ 0 & e^{0.644i} \end{bmatrix} \quad (\text{A.13})$$

$$M_{\text{Jones},8} = \text{TR} \cdot \text{TR} \cdot \mathbb{B}S_r \cdot \mathbb{B}S_r \cdot \mathbb{B}S_r = \begin{bmatrix} -1 & 0 \\ 0 & e^{0.644i} \end{bmatrix} \quad (\text{A.14})$$

A.2.2 Summary

As the total internal reflection induces a phase shift between both polarizations but all images two total internal reflections, we have the same phase shift for each image per camera.

A.3 3D epi-fluorescence microscope alignment

This protocol outlines the alignment procedure followed for achieving diffraction-limited performance of the 3D SOFI microscope. Figure A.1 outlines the used configuration.

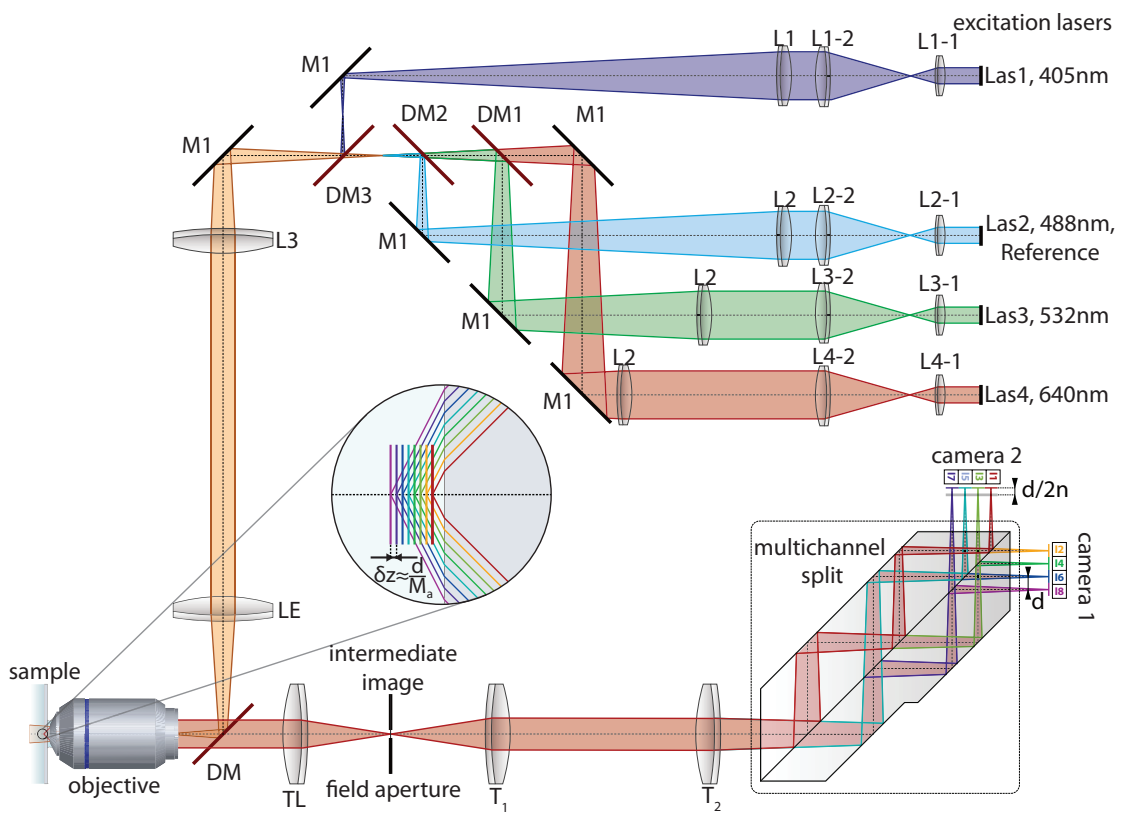


Figure A.1: Multi-plane epi-fluorescence microscope outline.

The excitation laser beams are focused at the back aperture of the objective to create a widefield epi-illumination. Changing the initial beam extension allows to adjust the illumination area and the maximum illumination intensity for each of the laser lines.

STEP 1: The alignment procedure starts with the alignment of one of the excitation laser beams that will serve as reference beam. We used the 488nm Toptica iBeam laser beam as reference as it has a well-defined Gaussian profile and is in a visible range of the spectrum. Adjust the beam expander to get a collimated output:

Appendix A. Image splitting prism characterization and setup alignment

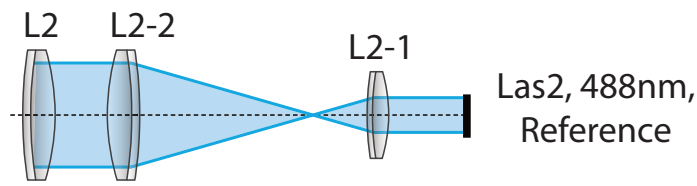


Figure A.2: Setting the laser beam expander

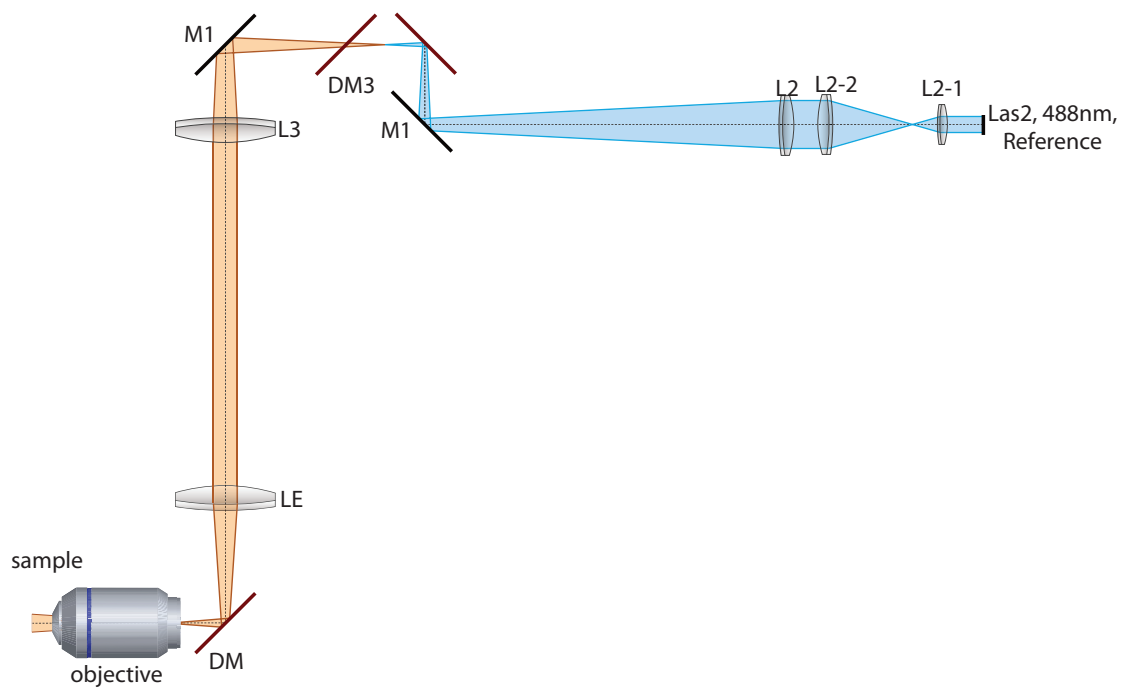


Figure A.3: Setting the laser beam expander

STEP 2: The laser beam should come at the center of the back aperture of the objective and orthogonally to it. The centering of the beam can be checked by placing a circular aperture between lenses L3 and LE.

A.3. 3D epi-fluorescence microscope alignment

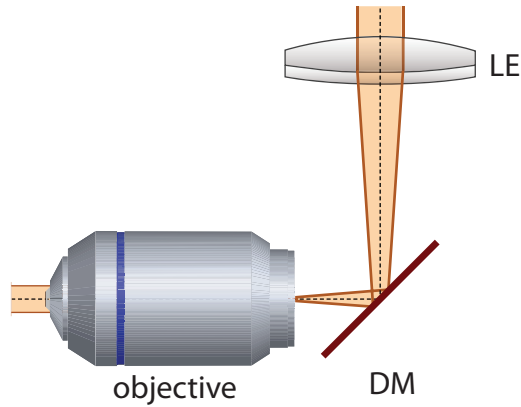


Figure A.4: Placing the objective

STEP 3: As a next step, a mirror coated coverslip should be introduced in the focal plane of the objective (if using an immersion objective, immersion liquid should also be applied). Lens LE should be then removed to create a collimated input into the objective. The correct position of the mirror corresponds to the collimated output of the objective (here and further on the collimation of the beam is checked by a shear plate).

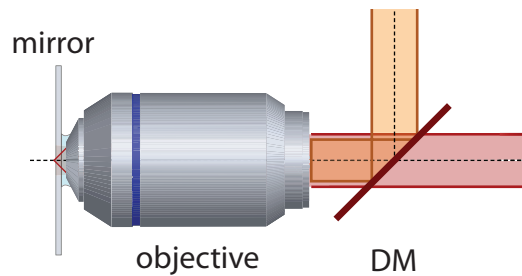


Figure A.5: Adjusting the mirror position

STEP 4: Next step is a positioning of the tube lens (TL). To do that, one should put back the lens LE and position the tube lens so that the output of the tube lens is collimated. As a result, the tube lens is focused at the back aperture of the objective, which ensures telecentricity of the system in the intermediate image plane.

Appendix A. Image splitting prism characterization and setup alignment

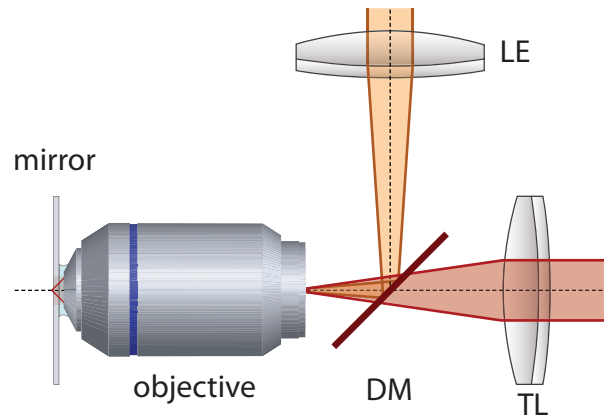


Figure A.6: Adjusting the tube lens position

STEP 5: The lenses T_1 and T_2 are positioned in a similar way as the tube lens by removing and placing back the lens LE and accordingly collimating the output. Thereby, the image side telecentricity of the system is ensured as well.

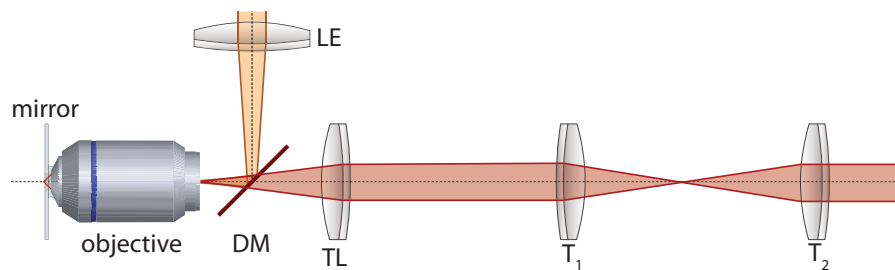


Figure A.7: Adjusting the telescope lenses

STEP 6: The next step is positioning the prism orthogonally to the optical axis. Place a mirror in the estimated position between the prism and camera 1. Place also an aperture with a small opening (1mm) after the lens T_2 . Position the mirror orthogonally to the beam by matching the reflection from it with the aperture opening.

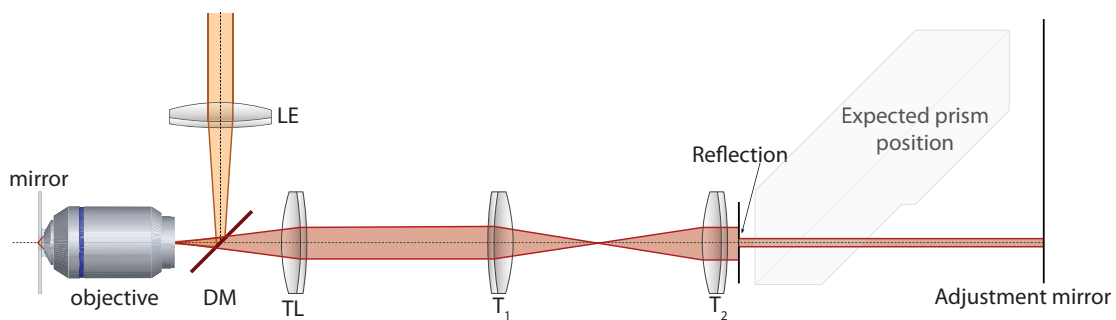


Figure A.8: Placing the adjustment mirror

A.3. 3D epi-fluorescence microscope alignment

Put the prism into position between T_2 and the mirror. There will be 4 minor beam reflections visible on the aperture, and the major one (beams converging from 4 paths). Orthogonality is ensured by matching the major reflection with the aperture opening by correcting the inclination of the prism. Remove the adjustment mirror afterwards.

STEP 7: The cameras are positioned and fixed orthogonally to the edges of the breadboard. The lateral position is checked by aligning the beams at the center of the camera sensor.

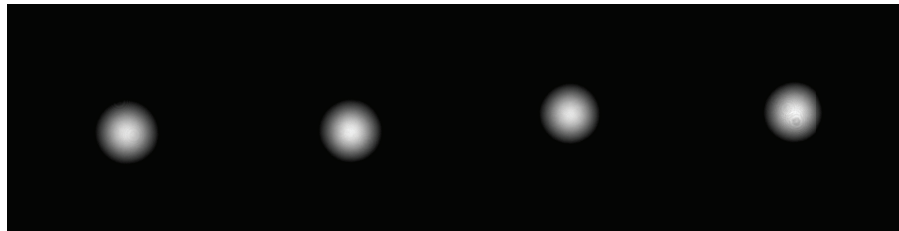


Figure A.9: Centering the beams on the camera sensor

The axial position is checked by removing the objective and imaging a far-distance object on the camera. The sharpest images should correspond to the 2 middle planes of each camera. The field aperture should be placed in the intermediate image plane accordingly with the sharpest visible edges corresponding to the 2 middle planes of each camera. The size of the aperture should be adjusted to correspond to approximately 512×512 pixels area on the camera image and avoid overlapping between the channels.

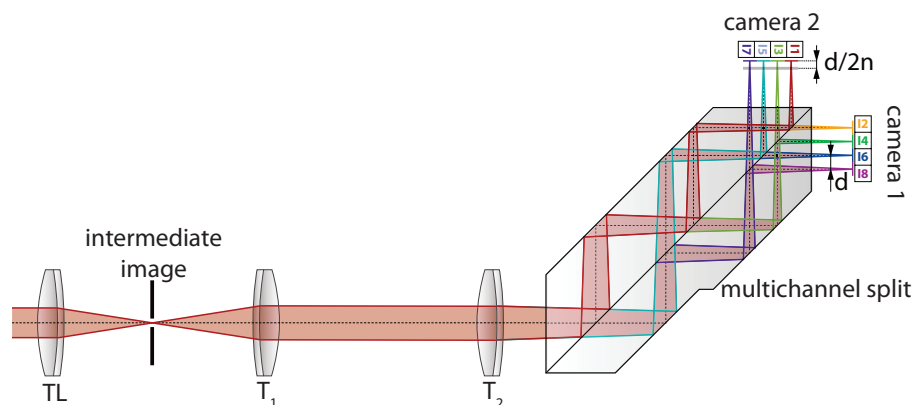


Figure A.10: Field aperture position

Appendix A. Image splitting prism characterization and setup alignment



Figure A.11: Image of a far-distance object

STEP 8: The final calibration and axial distance adjustment is done by imaging a sample with fluorescent beads. The beads should be sparsely distributed (non-overlapping within PSF) on a coverslip surface. A scan in depth is done with small (200nm) steps and an image at each axial sample position is acquired. From these images, the depth planes can be extracted. For instance, the images acquired from 2 cameras show the response from orange fluorescent beads.



Figure A.12: Image of fluorescent beads

Acknowledgments

This thesis has been a four year long adventure, which would not be possible without the support of my colleagues, friends, and family.

I would like to thank Prof. Theo Lasser for providing an opportunity to do PhD studies in his group. His availability for scientific discussions and support have been exceptional. The enthusiasm and numerous ideas often arising during discussions has kept my motivation during these years.

I am also very grateful to my co-supervisor Marcel Leutenegger. The support he provided was always extremely useful whether he was here in Lausanne or giving remote advices from Goettingen. It has been numerous amount of times when his advices helped me to get through a challenging problem.

Furthermore, I would like to thank Prof. Yves Bellouard, Prof. Dirk-Peter Herten, Prof. Georg Fantner, and Dr. Luigi Bonacina for kindly accepting to be part of my thesis committee.

I am especially grateful to Stefan Geissbühler for his guidance during the beginning of my PhD. Working together, whether it were discussions or long-term experiments, has always been a great pleasure. Last but not least, I really enjoyed our weekly ten kilometer run.

I would also like to thank Patrick Sandoz for his help with sample preparations and especially for Dreiklang-Lifeact construction. Furthermore, I would like to thank our collaborators, Prof. Stefan Jakobs, Prof. Jörg Enderlein, and Anja Huss for providing Dreiklang-Vimentin and Dreiklang-Keratin plasmids, as well as rsEGFP-MreB E.Colis. I greatly acknowledge Aurélien Godinat for his help in antibody staining tasks. I also thank Mélanie Hannebelle and Joelle Ven for providing M.Smegmatis FtsZ-Dreiklang, and Tristan Bolmont for providing the stained Microglial cells.

For the SOFI calculation part, a particular thanks goes to Tomas Lukes. His support and investigations, in particular in Bregman deconvolution, contributed greatly to the overall applicability of SOFI. I am also very grateful to Kristin Grussmayer for her help in multi-plane SOFI applications. I greatly acknowledge Emrah Bostan and Adrien Descloux for their contributions in TIE calculations.

Appendix A. Image splitting prism characterization and setup alignment

Many thanks goes to my colleagues and friends at LOB: Antonio Lopez, Miguel Sison, Séverine Coquoz, David Nguyen, Paul Marchand, Stéphane Broillet, Corinne Berclaz, Arno Bouwens, Arielle Planchette, Amir Nahas, Taoufiq Harach, Jérôme Extermann, Jochem Deen, Daniel Szlag, Vincent Shamaei, Fabienne Ubezio, and Noelia Simone for their help during these years. I have really enjoyed all the time we spent together in and outside of LOB.

I am very grateful to all my friends, in particular Alexey Lyasota, Johannes Schampel, and Ruslan Khairullin for sharing unforgettable experience outside the lab. Whatever activity we shared together, I always had more energy when coming back to the lab.

My greatest gratitude goes to my parents, Ruslan and Rimma, who have been encouraging me to go further throughout all these years. All this only became possible due to your endless support.

Lausanne, 12 December 2016

Bibliography

- [1] Stefan W. Hell. Far-Field Optical Nanoscopy. *Science*, 316(5828), 2007.
- [2] Bates Mark Bo Huang and Zhuang Xiaowei. Super resolution fluorescence microscopy. *Annu Rev Biochem.*, 78:993–1016, 2010.
- [3] Wim Vandenberg, Marcel Leutenegger, Theo Lasser, Johan Hofkens, and Peter Dedecker. Diffraction-unlimited imaging: from pretty pictures to hard numbers. *Cell and Tissue Research*, 360(1):151–178, apr 2015.
- [4] Stefan W. Hell and Jan Wichmann. Breaking the diffraction resolution limit by stimulated emission: stimulated-emission-depletion fluorescence microscopy. *Optics Letters*, 19(11):780, jun 1994.
- [5] Thomas A Klar and Stefan W Hell. Subdiffraction resolution in far-field fluorescence microscopy. *OPTICS LETTERS*, 24(14), 1999.
- [6] Stefan W Hell, Katrin I Willig, Marcus Dyba, Stefan Jakobs, Lars Kastrup, and Volker Westphal. Nanoscale Resolution with Focused Light : STED and Other RESOLFT Microscopy Concepts. *Science*, pages 571–579, 2006.
- [7] Roman Schmidt, Christian A Wurm, Stefan Jakobs, Johann Engelhardt, Alexander Egner, and Stefan W Hell. Spherical nanosized focal spot unravels the interior of cells. *Nature Methods*, 5(6):539–544, jun 2008.
- [8] Rainer Heintzmann and Mats G. L. Gustafsson. Subdiffraction resolution in continuous samples. *Nature Photonics*, 3(7):362–364, jul 2009.
- [9] Eric Betzig, George H Patterson, Rachid Sougrat, O Wolf Lindwasser, Scott Olenych, Juan S Bonifacino, Michael W Davidson, Jennifer Lippincott-Schwartz, and Harald F Hess. Imaging intracellular fluorescent proteins at nanometer resolution. *Science (New York, N.Y.)*, 313(5793):1642–5, sep 2006.
- [10] Michael J Rust, Mark Bates, and Xiaowei Zhuang. Sub-diffraction-limit imaging by stochastic optical reconstruction microscopy (STORM). *Nature methods*, 3(10):793–5, oct 2006.

Bibliography

- [11] Samuel T Hess, Thanu P K Girirajan, and Michael D Mason. Ultra-high resolution imaging by fluorescence photoactivation localization microscopy. *Biophysical journal*, 91(11):4258–72, dec 2006.
- [12] Thomas Dertinger, Ryan Colyer, Robert Vogel, Jörg Enderlein, and Shimon Weiss. Achieving increased resolution and more pixels with Superresolution Optical Fluctuation Imaging (SOFI). *Optics express*, 18(18):18875–85, aug 2010.
- [13] T Dertinger and R Colyer. Fast, background-free, 3D super-resolution optical fluctuation imaging (SOFI). *Proceedings of the . . .*, pages 22287–22292, 2009.
- [14] Marcus Dyba and Stefan W. Hell. Focal Spots of Size $\lambda / 23$ Open Up Far-Field Florescence Microscopy at 33 nm Axial Resolution. *Physical Review Letters*, 88(16):163901, apr 2002.
- [15] Roman Schmidt, Christian A Wurm, Stefan Jakobs, Johann Engelhardt, Alexander Egner, and Stefan W Hell. Spherical nanosized focal spot unravels the interior of cells. *Nature methods*, 5(6):539–44, jun 2008.
- [16] Marcel Lauterbach. *Fast STED Microscopy*. PhD thesis, Max Planck Institute for Biophysical Chemistry, 2009.
- [17] M. G. L. Gustafsson. Surpassing the lateral resolution limit by a factor of two using structured illumination microscopy. SHORT COMMUNICATION. *Journal of Microscopy*, 198(2):82–87, may 2000.
- [18] Mats G L Gustafsson. Nonlinear structured-illumination microscopy: wide-field fluorescence imaging with theoretically unlimited resolution. *Proceedings of the National Academy of Sciences of the United States of America*, 102(37):13081–6, sep 2005.
- [19] E Mudry, K Belkebir, J Girard, J Savatier, E Le Moal, C Nicoletti, M Allain, and A Sentenac. Structured illumination microscopy using unknown speckle patterns. *Nature Photonics*, 6(April):312–315, 2012.
- [20] Junhong Min, Jaeduck Jang, Dongmin Keum, Seung-Wook Ryu, Chulhee Choi, Ki-Hun Jeong, and Jong Chul Ye. Fluorescent microscopy beyond diffraction limits using speckle illumination and joint support recovery. *Scientific Reports*, 3:1–6, jun 2013.
- [21] A. H. VOIE, D. H. BURNS, and F. A. SPELMAN. Orthogonal-plane fluorescence optical sectioning: Three-dimensional imaging of macroscopic biological specimens. *Journal of Microscopy*, 170(3):229–236, jun 1993.
- [22] Sean Megason, Shankar Srinivas, Mary Dickinson, Anna-Katerina Hadjantonakis, Michael Weber, and Jan Huisken. Light sheet microscopy for real-time developmental biology. *Current Opinion in Genetics & Development*, 21(5):566–572, 2011.
- [23] B.-C. Chen, W. R. Legant, K. Wang, L. Shao, D. E. Milkie, M. W. Davidson, C. Janetopoulos, X. S. Wu, J. A. Hammer, Z. Liu, B. P. English, Y. Mimori-Kiyosue, D. P. Romero, A. T. Ritter,

- J. Lippincott-Schwartz, L. Fritz-Laylin, R. D. Mullins, D. M. Mitchell, J. N. Bembenek, A.-C. Reymann, R. Bohme, S. W. Grill, J. T. Wang, G. Seydoux, U. S. Tulu, D. P. Kiehart, and E. Betzig. Lattice light-sheet microscopy: Imaging molecules to embryos at high spatiotemporal resolution. *Science*, 346(6208):1257998–1257998, oct 2014.
- [24] Remi Galland, Gianluca Grenci, Ajay Aravind, Virgile Viasnoff, Vincent Studer, and Jean-Baptiste Sibarita. 3D high- and super-resolution imaging using single-objective SPIM. *Nature methods*, 12(7):641–644, may 2015.
- [25] Michael J Rust, Mark Bates, and Xiaowei Zhuang. imaging by stochastic optical reconstruction microscopy (STORM). *Nature methods*, 3(10):793–795, 2006.
- [26] Mike Heilemann, Sebastian van de Linde, Mark Schuttpelz, Robert Kasper, Britta Seefeldt, Anindita Mukherjee, Philip Tinnefeld, and Markus Sauer. Subdiffraction-Resolution Fluorescence Imaging with Conventional Fluorescent Probes. *Angewandte Chemie International Edition*, 47(33):6172–6176, aug 2008.
- [27] S Van De Linde, · R Kasper, · M Heilemann, and · M Sauer. Photoswitching microscopy with standard fluorophores. *Appl Phys B*, 93:725–731, 2008.
- [28] George H. Patterson and Jennifer Lippincott-Schwartz. A Photoactivatable GFP for Selective Photolabeling of Proteins and Cells. *Science*, 297(5588), 2002.
- [29] Fedor V Subach, George H Patterson, Suliana Manley, Jennifer M Gillette, Jennifer Lippincott-Schwartz, and Vladislav V Verkhusha. Photoactivatable mCherry for high-resolution two-color fluorescence microscopy. *Nature Methods*, 6(2):153–159, feb 2009.
- [30] Mark Bates, Timothy R. Blosser, and Xiaowei Zhuang. Short-Range Spectroscopic Ruler Based on a Single-Molecule Optical Switch. *Physical Review Letters*, 94(10):108101, mar 2005.
- [31] M. Heilemann, P. Dedecker, J. Hofkens, and M. Sauer. Photoswitches: Key molecules for subdiffraction-resolution fluorescence imaging and molecular quantification. *Laser & Photonics Review*, 3(1-2):180–202, feb 2009.
- [32] Daniel Sage, Hagai Kirshner, Thomas Pengo, Nico Stuurman, Junhong Min, Suliana Manley, and Michael Unser. Quantitative evaluation of software packages for single-molecule localization microscopy. *Nature Methods*, 12(8):717–724, jun 2015.
- [33] Seamus J Holden, Stephan Uphoff, and Achillefs N Kapanidis. DAOSTORM: an algorithm for high- density super-resolution microscopy. *Nature Methods*, 8(4):279–280, apr 2011.
- [34] Sang-Hee Shim, Chenglong Xia, Guisheng Zhong, Hazen P Babcock, Joshua C Vaughan, Bo Huang, Xun Wang, Cheng Xu, Guo-Qiang Bi, and Xiaowei Zhuang. Super-resolution fluorescence imaging of organelles in live cells with photoswitchable membrane probes. *Proceedings of the National Academy of Sciences of the United States of America*, 109(35):13978–83, aug 2012.

Bibliography

- [35] Bo Huang, Wenqin Wang, Mark Bates, and Xiaowei Zhuang. Three-Dimensional Super-Resolution Imaging by Stochastic Optical Reconstruction Microscopy. *Science*, 319(5864), 2008.
- [36] Sri Rama Prasanna Pavani, Michael A Thompson, Julie S Biteen, Samuel J Lord, Na Liu, Robert J Twieg, Rafael Piestun, and W E Moerner. Three-dimensional, single-molecule fluorescence imaging beyond the diffraction limit by using a double-helix point spread function. *Proceedings of the National Academy of Sciences of the United States of America*, 106(9):2995–9, mar 2009.
- [37] Stefan Geissbuehler, Claudio Dellagiacomma, and Theo Lasser. Comparison between SOFI and STORM. *Biomedical optics express*, 2(3):408–20, jan 2011.
- [38] Stefan Geissbuehler. *Structural and Functional Stochastic Super-Resolution Microscopy (Thesis 5826)*. PhD thesis, EPFL, 2013.
- [39] August Koehler. New Method of Illumination for Photomicrographical Purposes. *Journal of the Royal Microscopical Society*, 14:261–262, 1894.
- [40] Mustafa Mir, Basanta Bhaduri, Ru Wang, Ruoyu Zhu, and Gabriel Popescu. Quantitative Phase Imaging. *Progress in Optics*, 57:133–217, 2012.
- [41] Bernard Valeur and Mario N. Berberan-Santos. A Brief History of Fluorescence and Phosphorescence before the Emergence of Quantum Theory. *Journal of Chemical Education*, 88(6):731–738, jun 2011.
- [42] Osamu Shimomura, Frank H. Johnson, and Yo Saiga. Extraction, Purification and Properties of Aequorin, a Bioluminescent Protein from the Luminous Hydromedusan, Aequorea. *Journal of Cellular and Comparative Physiology*, 59(3):223–239, jun 1962.
- [43] E. Abbe. Beiträge zur Theorie des Mikroskops und der mikroskopischen Wahrnehmung. *Archiv für Mikroskopische Anatomie*, 9(1):413–418, dec 1873.
- [44] Yoshie Harada, Katsuhiko Sakurada, Toshiaki Aoki, David D. Thomas, and Toshio Yanagida. Mechanochemical coupling in actomyosin energy transduction studied by in vitro movement assay. *Journal of Molecular Biology*, 216(1):49–68, nov 1990.
- [45] Sebastian van de Linde and Markus Sauer. How to switch a fluorophore: from undesired blinking to controlled photoswitching. *Chem. Soc. Rev.*, 43(4):1076–1087, 2014.
- [46] Sören Doose, Hannes Neuweiler, and Markus Sauer. Fluorescence Quenching by Photoinduced Electron Transfer: A Reporter for Conformational Dynamics of Macromolecules. *ChemPhysChem*, 10(9-10):1389–1398, jul 2009.
- [47] Graham T Dempsey, Joshua C Vaughan, Kok Hao Chen, Mark Bates, and Xiaowei Zhuang. Evaluation of fluorophores for optimal performance in localization-based super-resolution imaging. *Nature methods*, 8(12):1027–36, dec 2011.

-
- [48] Taekjip Ha and Philip Tinnefeld. Photophysics of fluorescent probes for single-molecule biophysics and super-resolution imaging. *Annual review of physical chemistry*, 63:595–617, 2012.
- [49] Samuel T. Hess, Thanu P.K. Girirajan, and Michael D. Mason. Ultra-High Resolution Imaging by Fluorescence Photoactivation Localization Microscopy. *Biophysical Journal*, 91(11):4258–4272, 2006.
- [50] G. Ulrich Nienhaus and Jörg Wiedenmann. Structure, Dynamics and Optical Properties of Fluorescent Proteins: Perspectives for Marker Development. *ChemPhysChem*, 10(9-10):1369–1379, jul 2009.
- [51] Xin X Zhou and Michael Z Lin. Photoswitchable fluorescent proteins: ten years of colorful chemistry and exciting applications. *Current opinion in chemical biology*, 17(4):682–90, aug 2013.
- [52] Tanja Brakemann, Andre C Stiel, Gert Weber, Martin Andresen, Ilaria Testa, Tim Grotjohann, Marcel Leutenegger, Uwe Plessmann, Henning Urlaub, Christian Eggeling, Markus C Wahl, Stefan W Hell, and Stefan Jakobs. A reversibly photoswitchable GFP-like protein with fluorescence excitation decoupled from switching. *Nature biotechnology*, 29(10):942–7, oct 2011.
- [53] Alexey Sharonov and Robin M Hochstrasser. Wide-field subdiffraction imaging by accumulated binding of diffusing probes. *Proceedings of the National Academy of Sciences of the United States of America*, 103(50):18911–6, dec 2006.
- [54] Jonas Fölling, Mariano Bossi, Hannes Bock, Rebecca Medda, Christian A Wurm, Birka Hein, Stefan Jakobs, Christian Eggeling, and Stefan W Hell. Fluorescence nanoscopy by ground-state depletion and single-molecule return. *Nature methods*, 5(11):943–5, nov 2008.
- [55] E. J. AMBROSE. A Surface Contact Microscope for the study of Cell Movements. *Nature*, 178(4543):1194–1194, nov 1956.
- [56] Stefan Geissbuehler, Noelia L Bocchio, Claudio Dellagiacoma, Corinne Berclaz, Marcel Leutenegger, and Theo Lasser. Mapping molecular statistics with balanced super-resolution optical fluctuation imaging (bSOFI). *Optical Nanoscopy*, 1(1):4, 2012.
- [57] Stefan Geissbuehler, Azat Sharipov, Aurélien Godinat, Noelia L. Bocchio, Patrick A. Sandoz, Anja Huss, Nickels A. Jensen, Stefan Jakobs, Jörg Enderlein, F. Gisou van der Goot, Elena A. Dubikovskaya, Theo Lasser, and Marcel Leutenegger. Live-cell multiplane three-dimensional super-resolution optical fluctuation imaging. *Nature Communications*, 5:5830, dec 2014.
- [58] Claudio Dellagiacoma. *Single Molecule Sensing*. PhD thesis, EPFL, 2011.

Bibliography

- [59] E. C. Titchmarsh. The Zeros of Certain Integral Functions. *Proceedings of the London Mathematical Society*, s2-25(1):283–302, jan 1926.
- [60] L. Lucy. An iterative technique for the rectification of observed distributions. *The Astronomical Journal*, 79:745, jun 1974.
- [61] William Hadley Richardson. Bayesian-Based Iterative Method of Image Restoration*. *Journal of the Optical Society of America*, 62(1):55, jan 1972.
- [62] Thomas Dertinger, Jianmin Xu, Omeed Naini, Robert Vogel, and Shimon Weiss. SOFI-based 3D superresolution sectioning with a widefield microscope. *Optical Nanoscopy*, 1(1):2, 2012.
- [63] Virendra N. Mahajan and SPIE (Society). *Aberration theory made simple*. SPIE Press, 2011.
- [64] E. Wolf M. Born. *Principles of optics: Electromagnetic theory of propagation, interference and diffraction of light*. Pergamon Press, 1959.
- [65] Albert H. Coons, Hugh J. Creech, Norman R. Jones, and Ernst Berliner. The Demonstration of Pneumococcal Antigen in Tissues by the Use of Fluorescent Antibody. *The Journal of Immunology*, 45(3):159–170, 1942.
- [66] Tim Grotjohann, Ilaria Testa, Marcel Leutenegger, Hannes Bock, Nicolai T. Urban, Flavie Lavoie-Cardinal, Katrin I. Willig, Christian Eggeling, Stefan Jakobs, and Stefan W. Hell. Diffraction-unlimited all-optical imaging and writing with a photochromic GFP. *Nature*, 478(7368):204–208, sep 2011.
- [67] Brad Chazotte. Labeling mitochondria with MitoTracker dyes. *Cold Spring Harbor protocols*, 2011(8):990–2, aug 2011.
- [68] Matthias Geissbuehler and Theo Lasser. How to display data by color schemes compatible with red-green color perception deficiencies. *Optics Express*, 21(8):9862, apr 2013.
- [69] Florent Ginhoux, Shawn Lim, Guillaume Hoeffel, Donovan Low, and Tara Huber. Origin and differentiation of microglia. *Frontiers in Cellular Neuroscience*, 7:45, 2013.
- [70] Tristan Bolmont, Florent Haiss, Daniel Eicke, Rebecca Radde, Chester a Mathis, William E Klunk, Shinichi Kohsaka, Mathias Jucker, and Michael E Calhoun. Dynamics of the microglial/amyloid interaction indicate a role in plaque maintenance. *The Journal of neuroscience : the official journal of the Society for Neuroscience*, 28(16):4283–92, apr 2008.
- [71] Stefan a Grathwohl, Roland E Kälin, Tristan Bolmont, Stefan Prokop, Georg Winkelmann, Stephan a Kaeser, Jörg Odenthal, Rebecca Radde, Therese Eldh, Sam Gandy, Adriano Aguzzi, Matthias Staufenbiel, Paul M Mathews, Hartwig Wolburg, Frank L Heppner, and Mathias Jucker. Formation and maintenance of Alzheimer's disease beta-amyloid plaques in the absence of microglia. *Nature neuroscience*, 12(11):1361–3, nov 2009.

-
- [72] Andreas Gahlmann and W. E. Moerner. Exploring bacterial cell biology with single-molecule tracking and super-resolution imaging. *Nature Reviews Microbiology*, 12(1):9–22, dec 2013.
- [73] Erfei Bi and Joe Lutkenhaus. FtsZ ring structure associated with division in *Escherichia coli*. *Nature*, 354(6349):161–164, nov 1991.
- [74] Pascal Damian Odermatt. *Mechanical and Functional Study of Cell Physiology at the Nanoscale PAR*. PhD thesis, EPFL, 2016.
- [75] Henrik Strahl and Frank Bürmann. The actin homologue MreB organizes the bacterial cell membrane. *Nature Communications*, 5:589–618, mar 2014.
- [76] Bassam Hajj, Jan Wisniewski, Mohamed El Beheiry, Jiji Chen, Andrey Revyakin, Carl Wu, and Maxime Dahan. Whole-cell, multicolor superresolution imaging using volumetric multifocus microscopy. *Proceedings of the National Academy of Sciences of the United States of America*, 111(49):17480–17485, nov 2014.
- [77] Bo Huang, Wenqin Wang, Mark Bates, and Xiaowei Zhuang. Three-dimensional super-resolution imaging by stochastic optical reconstruction microscopy. *Science (New York, N.Y.)*, 319(5864):810–3, feb 2008.
- [78] Gleb Shtengel, James A Galbraith, Catherine G Galbraith, Jennifer Lippincott-Schwartz, Jennifer M Gillette, Suliana Manley, Rachid Sougrat, Clare M Waterman, Pakorn Kanchanawong, Michael W Davidson, Richard D Fetter, and Harald F Hess. Interferometric fluorescent super-resolution microscopy resolves 3D cellular ultrastructure. *Proceedings of the National Academy of Sciences of the United States of America*, 106(9):3125–30, mar 2009.
- [79] Daniel Aquino, Andreas Schönle, Claudia Geisler, Claas v Middendorff, Christian A Wurm, Yosuke Okamura, Thorsten Lang, Stefan W Hell, and Alexander Egner. Two-color nanoscopy of three-dimensional volumes by 4Pi detection of stochastically switched fluorophores. *Nature Methods*, 8(4):353–359, apr 2011.
- [80] Tom Goldstein and Stanley Osher. The Split Bregman Method for L1-Regularized Problems. *SIAM Journal on Imaging Sciences*, 2(2):323–343, jan 2009.
- [81] F. Sroubek and P. Milanfar. Robust Multichannel Blind Deconvolution via Fast Alternating Minimization. *IEEE Transactions on Image Processing*, 21(4):1687–1700, apr 2012.
- [82] Leonid I. Rudin, Stanley Osher, and Emad Fatemi. Nonlinear total variation based noise removal algorithms. *Physica D: Nonlinear Phenomena*, 60(1):259–268, 1992.
- [83] Tomas Lukes. *Super-resolution microscopy live cell imaging and image analysis*. PhD thesis, Czech technical university in Prague.

Bibliography

- [84] Aleksandra Simiczyjew, Antonina Joanna Mazur, Agnieszka Popow-Woźniak, Maria Malicka-Błaszkiwicz, and Dorota Nowak. Effect of overexpression of β - and γ -actin isoforms on actin cytoskeleton organization and migration of human colon cancer cells. *Histochemistry and cell biology*, 142(3):307–22, sep 2014.
- [85] Julia Riedl, Alvaro H Crevenna, Kai Kessenbrock, Jerry Haochen Yu, Dorothee Neukirchen, Michal Bista, Frank Bradke, Dieter Jenne, Tad A Holak, Zena Werb, Michael Sixt, and Roland Wedlich-Soldner. Lifeact: a versatile marker to visualize F-actin. *Nature methods*, 5(7):605–7, jul 2008.
- [86] Andrew G York, Panagiotis Chandris, Damian Dalle Nogare, Jeffrey Head, Peter Wawrzusin, Robert S Fischer, Ajay Chitnis, and Hari Shroff. Instant super-resolution imaging in live cells and embryos via analog image processing. *Nature methods*, 10(11):1122–6, nov 2013.
- [87] Michael Reed Teague. Deterministic phase retrieval: a Green's function solution. *Journal of the Optical Society of America*, 73(11):1434, nov 1983.
- [88] Emrah Bostan, Emmanuel Froustey, Masih Nilchian, Daniel Sage, and Michael Unser. Variational Phase Imaging Using the Transport-of-Intensity Equation. *IEEE transactions on image processing: a publication of the IEEE Signal Processing Society*, PP(99):1, dec 2015.
- [89] Emrah Bostan. *Sparsity-Based Data Reconstruction Models for Biomedical Imaging*. PhD thesis, EPFL, 2016.
- [90] Taewoo Kim, Renjie Zhou, Mustafa Mir, S. Derin Babacan, P. Scott Carney, Lynford L. Goddard, and Gabriel Popescu. White-light diffraction tomography of unlabelled live cells. *Nature Photonics*, 8(3):256–263, jan 2014.
- [91] Pascal D. Odermatt, Arun Shivanandan, Hendrik Deschout, Radek Jankele, Adrian P. Niev-ergelt, Lely Feletti, Michael W. Davidson, Aleksandra Radenovic, and Georg E. Fantner. High-Resolution Correlative Microscopy: Bridging the Gap between Single Molecule Localization Microscopy and Atomic Force Microscopy. *Nano Letters*, 15(8):4896–4904, 2015.

CURRICULUM VITAE: Azat R. Sharipov

Affiliation and official address

École polytechnique Fédérale de Lausanne (EPFL), Laboratoire d'Optique Biomedicale, BM 5.142, Station 17, CH-1015, Lausanne, Switzerland,
e-mail: AzatRSharipov@gmail.com,
skype: azatrsharipov



Personal details

Date/place of birth; citizenship

November 17, 1989, Ufa (Russia); Russian

Marital status:

Single

Professional experience

January 2013-present

École polytechnique fédérale de Lausanne (EPFL), Laboratoire d'Optique Biomedicale, research assistant

Multidisciplinary responsibilities, including design, assembly and maintenance of microscopy-oriented optical systems, image processing, and biological sample preparations (immunohistochemistry, cell culture maintenance, various transfection types).

September 2012 – January 2013

Danip ltd., technological analyst

Comprehensive analysis of technological investment projects, including product, technology, team, equipment, infrastructure and plan of project coordination.

September 2009 – June 2012

P.N. Lebedev Physical Institute, RAS, research assistant

Hands-on use of femtosecond laser for nanostructuring solid surfaces and nanoparticles generation. Photonic crystal doping. Surface characterisation by optical and electron microscopy. Spectroscopy of photonic crystals.

2005-2006

Free-Winds ltd., technician

Design and assembly of drones for aerial photography.

Education

January 2013 – present

École polytechnique fédérale de Lausanne (EPFL), Faculty of Microengineering, Doctoral program in photonics

2006-2012

Moscow Institute of Physics and Technology (MIPT), Department of General and Applied Physics, Division of Optics and Quantum Radiophysics, Master of Science in Applied Mathematics and Physics. Diploma of additional education "Translator in the field of professional communication"

2010

2005-2006

Gymnasium 93, Ufa, accomplished with Gold medal (secondary school diploma, GPA: 5.0, A=5)

Computer skills

Matlab, C, Zemax, Maple, Office, Latex, Illustrator, ImageJ, Kompas-3D
Familiar with MS Windows and Mac OS

Languages

Russian (First language)
English (Full professional proficiency)
French (Limited working proficiency)
German (Basics)

Publications, presentations

Publications in refereed journals

4

Presentations at scientific meetings

3

Hobbies

Aeromodelling, Mountain bike, Skiing

Peer-reviewed publications

Azat Sharipov, Tomas Lukes, Patrick A. Sandoz, Amir Nahas, Marcel Leutenegger, Stefan Geissbuehler, Daniel Szlag, Gisou van der Goot, Theo Lasser. Live cell three-dimensional time-lapse super-resolution imaging, publication in preparation.

Hendrik Deschout, Tomas Lukes, Azat Sharipov, Daniel Szlag, Lely Feletti, Wim Vandenberg, Peter Dedecker, Marcel Leutenegger, Johan Hofkens, Theo Lasser, and Aleksandra Radenovic. Complementarity of PALM and SOFI for super-resolution live cell imaging of focal adhesions. Nature Communications, 7:13693, dec 2016.

Arik Girsault, Tomas Lukes, Azat Sharipov, Stefan Geissbuehler, Marcel Leutenegger, Wim Vandenberg, Peter Dedecker, Johan Hofkens, Theo Lasser. SOFI Simulation Tool: A Software Package for Simulating and Testing Super-Resolution Optical Fluctuation Imaging. PLoS ONE 11(9): e0161602. 2016.

Stefan Geissbuehler, Azat Sharipov, Aurélien Godinat, Noelia L. Bocchio, Patrick A. Sandoz, Anja Huss, Nickels A. Jensen, Stefan Jakobs, Jörg Enderlein, F. Gisou van der Goot, Elena A. Dubikovskaya, Theo Lasser, and Marcel Leutenegger. Live-cell multiplane three-dimensional super-resolution optical fluctuation imaging. Nature Communications, 5:5830, dec 2014.

E. V. Golosov, A. A. Ionin, Yu. R. Kolobov, S. I. Kudryashov, A. E. Ligachev, S. V. Makarov, Yu. N. Novoselov, L. V. Seleznev, D. V. Sinitsyn, and A. R. Sharipov. Near-threshold femtosecond laser fabrication of one-dimensional subwavelength nanogratings on a graphite surface, Phys. Rev. B 83, 115426, 2011.

Conference presentations

Azat Sharipov, Tomas Lukes, Patrick Sandoz, Marcel Leutenegger, Stefan Geissbuehler, Amir Nahas, Daniel Szlag, Theo Lasser, Live-Cell 3 dimensional time-lapse super-resolution imaging, «SMLMS», Lausanne, 2016.

Azat Sharipov, Stefan Geissbuehler, Marcel Leutenegger, Theo Lasser, Live-cell multiplane three-dimensional super-resolution optical fluctuation imaging, oral talk at «Focus on microscopy», Goettingen, 2015.

A.R. Sharipov, V.S. Gorelik, A.A. Ionin, S.I. Kudryashov, S.V. Makarov, L.V. Seleznev, D.V. Sinitsyn, R.A. Chanieva, Fabrication of new optical nanocomposites based on artificial opals, poster presentation at «Optics-2011», St.-Petersburg, 2011.

